# ESTIMACIÓN DE FLUJOS DE AGUA ENTRE SUELO, VEGETACIÓN Y ATMÓSFERA MEDIANTE TELEDETECCIÓN

## WATER FLUXES ESTIMATION BETWEEN SOIL, VEGETATION AND ATMOSPHERE USING REMOTE SENSING

---


Tesis Doctoral presentada por:

**GORKA MENDIGUREN GONZÁLEZ**

Bajo la dirección de:

**Dra. María Pilar Martín Isabel**

**Dr. David Riaño Arribas**

**Dr. Héctor Nieto Solana**


---


Programa de Doctorado en Tecnologías de la Información Geográfica.

DEPARTAMENTO DE GEOLOGÍA, GEOGRAFÍA Y MEDIO AMBIENTE

*Alcalá de Henares, Septiembre de 2014*

*'I confess that I have been blind as a mole,*

*but it is better to learn wisdom late*

*than never to learn it at all.'*

**Sherlock Holmes**

**-The Man with the Twisted Up**

# AGRADECIMIENTOS

*Me gustaría aprovechar estas líneas, que serán seguramente las que más gente lea, o las únicas, para mostrar mi agradecimiento a algunas personas e instituciones que con su trabajo han hecho posible esta tesis doctoral.*

*En primer lugar quiero agradecer a mis directores Pilar Martin, David Riaño y Héctor Nieto sin los cuales no existiría esta memoria y mucho menos estos agradecimientos. Su entusiasmo, dedicación y paciencia han sido un apoyo esencial a lo largo de estos casi cinco años.*

*Igualmente, quiero expresar mi gratitud a la Dr. Inge Sandholt y el Dr. Rasmus Fensholt de la Universidad de Copenhague (Dinamarca) por aceptarme en sus grupos de investigación en mis estancias breves, y las no tan breves , y hacerme sentir como en casa. Creo que han sido unas experiencias muy enriquecedoras, tanto laboral como personalmente.*

*Debo agradecer al Ministerio de Economía y competitividad la financiación recibida por medio de una beca FPI-Predoctoral (BES-2009-026831), así como las ayudas para realizar estancias en otros centros de investigación (EEBB-2011-44463, EEBB-12-04542). Así mismo quiero agradecer también al servicio estatal público de empleo la ayuda económica prestada para la finalización de este trabajo.*

*También, quiero agradecer a todo personal del Centro de Ciencias Humanas y Sociales (CCHS-CSIC) por su labor prestada y mención especial a los integrantes del Laboratorio de Espectro-Radiometría y Teledetección Ambiental. A mis compañeros de oficina, Javi, Marta, Elia, Isra, Pilar, Lara… muchísimas gracias!!*

*No puedo finalizar estos agradecimientos sin hacer una mención especial al equipo BIOSPEC-FLUXPEC. Son muchos los buenos momentos que hemos compartido en el campo e imprescindible vuestra colaboración en la recogida de datos de campo que he usado en gran parte de la tesis. Os estoy enormemente agradecido.*

*Finalmente, aunque no menos importante, me gustaría mencionar a todas aquellas personas que me han ayudado y acompañado en el camino de estos casi cinco años de tesis doctoral: pareja, familia, amigos, compañeros de trabajo. Son muchas las personas a las que no quisiera olvidar en este apartado, y poco el espacio. Durante estos años he tratado de trasmitirles mi agradecimiento día a día con cada uno de mis actos, espero haberlo logrado con éxito.*

# CONTENTS

# RESUMEN

En la frontera entre la superficie terrestre y la atmósfera se producen numerosos procesos físicos relacionados con el ciclo hidrológico. Cuando se producen precipitaciones en forma de lluvia, y el agua alcanza la superficie terrestre, una parte llega al suelo y otra parte puede ser interceptada por la vegetación. La fracción que llega al suelo se infiltra en la zona no saturada donde se almacena, lo humedece, disuelve los elementos que son absorbidos posteriormente por la vegetación y modifica las propiedades físicas del suelo. Para que la vegetación pueda desarrollarse es necesario que la planta abra los estomas, absorba $CO_2$ y realice la fotosíntesis. Durante este proceso se produce una pérdida de agua a través de la hoja, que si es lo suficientemente grande puede llegar a hacer que la planta marchite si no es capaz de reponerla del suelo. El agua del suelo es devuelta a la atmósfera posteriormente mediante la evaporación y la transpiración de las plantas. La Evapotranspiración (ET) se puede definir como el proceso por el cual se transfiere el agua evaporada del suelo y la transpirada de la vegetación a la atmósfera. La ET es de gran relevancia por su efecto en el clima local y la meteorología así como en un gran número de procesos biofísicos. La ET es un proceso que depende de los flujos energéticos como la radiación neta (Rn), el flujo sensible (H) y el flujo de calor en el suelo (G).

Es posible medir *in situ* diferentes variables de la vegetación, el suelo y la atmósfera relacionadas con los flujos de agua en la superficie terrestre. Sin embargo estas mediciones son complejas debido a su elevada dinámica espacial y temporal. Como alternativa a estas medidas *in situ*, se puede utilizar medidas obtenidas remotamente por sensores instalados en satélites, esto es, teledetección. Actualmente, la teledetección ofrece una gran variedad de sensores con diferentes características espaciales y temporales lo que la convierte en una herramienta idónea para el seguimiento de estos procesos teniendo en cuenta que existen diferencias, en algunos casos importantes, entre lo observado *in situ* y lo calculado

mediante teledetección. Este hecho hace que se requieran rigurosas validaciones de estas estimaciones, así como de los protocolos de recogida de los datos *in situ*.

En este trabajo se han analizado diferentes variables relacionadas con los flujos de agua entre tierra y atmósfera. El estudio se ha centrado en variables referentes al estado hídrico de la vegetación y el suelo, la estimación de parámetros biofísicos de la vegetación y en el comportamiento de la Fracción Evaporativa (EF), definida como la relación entre la ET y la energía disponible del sistema (Rn –G). Todos los datos empleados en este trabajo fueron recogidos en un ecosistema de dehesa en la localidad de Las Majadas del Tiétar, en la provincia de Cáceres. En esta zona está operativa, desde 2003, una torre de medición de flujos de agua y carbono perteneciente a la red FLUXNET.

La primera parte del trabajo se ha centrado en la estimación de parámetros biofísicos y estructurales de la vegetación, concretamente los relacionados con el contenido de agua. Para ello se han empleado numerosos datos recogidos en campo a lo largo de dos años fenológicos completos y se relacionaron con las medidas espectrales a dos escalas diferentes, campo y sensor MODIS (500 m). El contenido de agua se calculó usando tres métricas diferentes calculadas a partir de la misma muestra, el Contenido de Humedad de la Vegetación (FMC), el Espesor Equivalente de Agua (EWT) y el Contenido de Agua del Dosel (CWC). Además se usaron dos estimaciones a partir de Modelos de Transferencia Radiativa (RTM) para la obtención del FMC y CWC que fueron comparados con las obtenidas a partir de los modelos empíricos creados a partir los índices espectrales. Otras variables relacionadas como el contenido de materia seca (Dm) y el índice de área foliar (LAI) fueron también evaluadas usando índices de vegetación.

Entre los resultados destacables de este estudio se encuentran en primer lugar los relacionados con el protocolo de recogida de datos en campo. En este estudio se obtuvieron evidencias de que las diferencias temporales a la hora de recoger datos en campo son más importantes que las diferencias espaciales en este ecosistema. Además se demostró la necesidad de mostrar consistencia en el protocolo de muestreo: tamaño de la muestra, hora de recogida de las muestras, etc.

y en la importancia de evitar, en lo posible la toma de decisiones, generalmente subjetivas, por parte de los operadores de campo. Otro resultado destacable ha sido demostrar la existencia de una alta variabilidad del Dm a lo largo del año. Esto indica que asumir, como sugieren algunos autores, un valor constante de Dm para la estimación del espesor equivalente de agua a partir del contenido de humedad de la vegetación no es una opción viable en este ecosistema. De los índices de vegetación que fueron comparados en el estudio, el que presentó menores correlaciones fue el Índice de Vegetación Resistente a la Atmósfera (VARI). Se observaron algunas diferencias en el comportamiento de los modelos empíricos obtenidos con MODIS y las producidas a partir de medidas espectrales de campo, obteniendo resultados algo mejores en el caso de MODIS. Este hecho posiblemente sea debido a que las adquisiciones de del sensor MODIS presentan diferentes ángulos de observación, lo que reduce la proporción de suelo captada por el sensor y por lo tanto capturando una mayor proporción del dosel. La comparación entre los modelos empíricos y las estimaciones a partir de modelos de transferencia radiativa demostró que en este caso los modelos empíricos aún mejoran las estimaciones de los modelos físicos desarrollados en zonas similares para estimar el contenido de humedad de la vegetación.

La segunda parte del trabajo se ha centrado en la estimación del contenido de humedad del suelo combinando datos ópticos y térmicos mediante el cálculo del Índice de Temperatura y Sequedad de la Vegetación (TVDI) cuya obtención se basa en la técnica del triángulo. Se han investigado diferentes factores que afectan a la definición del triángulo, y cómo estos afectan los valores del TVDI y a su relación final con el contenido de humedad del suelo. En este trabajo se introdujo una modificación al cálculo del TVDI en la que se sustituyó el Índice de Vegetación de Diferencia Normalizada (NDVI) por el Índice de Diferencia Infraroja Normalizada (NDII). Esta modificación se tradujo en una mejora en el comportamiento de los modelos empíricos para estimar el contenido de humedad del suelo.

Finalmente en la tesis se investiga el comportamiento de la EF en la zona de estudio y su estimación a partir de teledetección. El principal motivo del empleo de la EF es que ha sido ampliamente utilizada para estimar la evapotranspiración

diaria, asumiendo que la EF es constante a lo largo del día. A partir de las medidas recogidas por una torre de flujos se han evaluado las variaciones diarias y se han validado las estimaciones de EF calculadas a partir de imágenes Landsat. Se ha usado una nueva versión modificada de la técnica del triángulo en la que se ha introducido el índice de área foliar adaptado a la escala Landsat a partir del producto MODIS (de 1 km a 30 m) como sustituto del índice de vegetación. Además se muestra un innovador método basado en las estadísticas propias del triángulo para la selección de las fechas a incluir en el análisis estadístico. La validación de las estimaciones de EF se ha llevado a cabo de dos maneras diferentes: usando las contribuciones de todos los pixeles incluidos en la zona de influencia de la torre; y utilizando el valor del único pixel correspondiente a la localización de la torre, mostrando ambas aproximaciones escasas diferencias en cuanto a resultados. Además se han comparado las EF diarias y la correspondiente a la hora de la pasada de Landsat sobre la zona de estudio. En este caso se observaron mayores diferencias, lo cual indica que el supuesto de una EF constante a lo largo del día ha de ser tomada con ciertas precauciones si el objetivo final es el cálculo de la evapotranspiración diaria.

## ABSTRACT

In the boundary layer between vegetation and soil with the atmosphere different processes within the hydrologic cycle take place. When rainfall occurs, part of the water reaches the inland surface, part is infiltrated in the soil, and part is intercepted by vegetation. The fraction reaching the soil infiltrates in the unsaturated zone of the soil making it wet, dissolving the elements that will be absorbed by the plants, and changing the physical properties of the soil. Vegetation needs to open the stomata during the absorption of $CO_2$ during photosynthesis. In this process loss of water by vegetation trough the leaves is produced. If this is loss is large, the wilting point of the plant can be reached, and therefore there is a need of water uptake which is done by the roots. Water returns to the atmosphere trough evaporation and plant transpiration. Evapotranspiration (ET), which can be defined as the process that combines the evaporation from the soil and the transpiration from the plants transferring water vapor to the atmosphere, is one the most relevant processes as it has strong influence on local climate, weather and many other biophysical processes. Finally, ET is an energy driven process that relies on land-surface energy fluxes like net radiation ($R_n$), sensible heat flux (H) and ground heat flux (G).

It is possible to collect *in situ* different variables from vegetation, soil and atmosphere related to water fluxes in the boundary layer. However, these variables are difficult to measure due to its spatial and temporal variability. Remote sensing platforms on the other hand offer an alternative to *in situ* measurements. Nowadays, remote sensing offers a great variety of sensors with different spatial and temporal resolutions, which makes this tool very attractive to monitor these processes, although there is a need for accounting for the existing differences between remote sensing estimates and *in situ* measurements. This issue requires rigorous validations of remote sensing estimates as well as *in situ* sampling protocols.

In this thesis, different variables related to water fluxes between vegetation, soil and atmosphere have been analyzed. The study focused on vegetation and soil water content, biophysical parameters of vegetation and in the behavior of Evaporative Fraction (EF), is defined as the ratio between ET and available energy ($R_n$-G). All data used were collected in a *dehesa* ecosystem at Las Majadas del Tiétar, in the province of Cáceres in Spain. In the study site there is an eddy covariance flux tower inside the FLUXNET network that has been operation since 2003.

The first part of this work was focused on the estimation of biophysical and structural variables of the vegetation, being the study mainly oriented to estimate vegetation water content. A large data set collected over two full phenological years was used to relate different metrics of vegetation water content with spectral measurements at two different scales, using proximal sensing data and using MODIS surface reflectance data (500 m). Three different water content metrics simultaneously obtained from the same sample - Fuel Moisture Content (FMC), Equivalent Water Thickness (EWT) and Canopy Water Content (CWC) - were related to spectral vegetation indices (VI) calculated from MODIS and proximal sensing data. In addition estimates of FMC and CWC by inversion techniques of Radiative Transfer Model (RTM) were tested and compared against the empirical models. Dry Matter content (Dm) and Leaf Area Index (LAI) were also evaluated empirically with VI.

As result from this study, several findings were revealed. The first one is related to the field data collection: results showed that temporal changes in FMC, EWT and CWC are more critical than their spatial variation within the MODIS pixel. The field protocols should hence be adapted in order sample more frequently rather than conducting extensive spatial samplings. Field data analysis also highlighted the need of being consistent with the size of the sample collected, and avoiding as much as possible subjective operator interpretations when collecting the data. Another relevant result from this study is that due to the high seasonal Dm variability, a constant annual value would not be recommended to predict EWT from FMC. Furthermore, Vegetation Atmospheric Resistant Index (VARI) provided the worst results in all cases. The empirical estimators differed between sensors,

slightly better for MODIS than proximal sensing, probably due to differences in view angles, and as result the proportions of canopy observed by the sensor increases reducing the soil effect. These empirical methods still exceed RTM inversions developed for other sites to predict FMC and CWC.

The second part focused on estimation of soil moisture (SM) combining optical and thermal sensors and evaluating the Temperature Vegetation Dryness Index (TVDI) calculated using the triangle method. Some of the factors involved in the triangle parameterization were studied to better understand how they affect the TVDI values and the implications in the final model performance for estimating SM. A modification was introduced in the TVDI calculation and the Normalized Difference Vegetation Index (NDVI) was substituted by the Normalized Difference Infrared Index (NDII). This modification translated in a better performance of empirical methods to estimate SM using this technique.

Finally, this study investigates the behavior of EF on the site and the estimate using remote sensing. The reason why EF is investigated is that EF has been extensively used to retrieve daily ET, assuming that EF remains constant during daytime. Using the EF measured by the Eddy Covariance (EC), we have investigate how EF varies temporary and validated the EF calculated from Landsat using a modified triangle approach in which the VI was substituted by MODIS LAI downscaled to Landsat (from 1km to 30m). A novel method for selecting the highest quality days for the analysis based on the statistics of the triangle is also presented. The validation of EF estimates from remote sensing was carried out using either the pixel contribution based on the information of the EC footprint, or the single pixel located in the EC tower, showing both cases very similar results. Furthermore, daily EF and instantaneous EF at the time of the satellite overpass were also compared with the EF calculated from Landsat. Results of this comparison showed larger differences indicating that for this ecosystem the EF self-preservation assumption should be carefully taken into account if daily ET has to be obtained from EF.

## STRUCTURE OF THE PHD DISSERTATION

This work studies three different components of the hydrological cycle occurring in the boundary layer between vegetation-soil and atmosphere by using proximal and remote sensing data. These processes were divided into:

1. Vegetation biophysical variables
2. Soil moisture estimation
3. Evaporative fraction using Landsat

The document is divided into six chapters. The first chapter is dedicated to present the motivation to carry out this study and is followed by a specific literature review for each of the topics and ending with the objectives of this work. The second chapter describes the different methods used to collect and process the data used in the study. This is followed by three chapters in which the specific methods, results and discussion for each of the topics under investigation are presented: the estimation of biophysical variables related with vegetation water content (chapter 3), soil moisture (chapter 4) and the Evaporative Fraction (chapter 5). Finally, in chapter 6 the general conclusions of the thesis are summarized.

# 1 Introduction

While oceans represent the largest water reservoir (96.5% of Earth's total water) with an estimated volume of 1,338,000,000 km$^3$ , fresh water represents only 2.5% of Earth's total water (93,000 km$^3$) (**Figure 1**). The largest contributors of fresh water are the ice caps with accounting for about 70% of Earth's fresh water being Antarctica the largest reservoir. Ground water is the second largest reservoir of fresh water accounting for the 30%, however this water is only accessible to deep-rooted plant species (Dawson and Ehleringer 1991) and a small part of the human population with the infrastructures to reach it. The last pool of fresh water is the surface water that accounts for rivers, lakes, soil moisture (SM), and biological water, which represents only about 1% of the total fresh water.

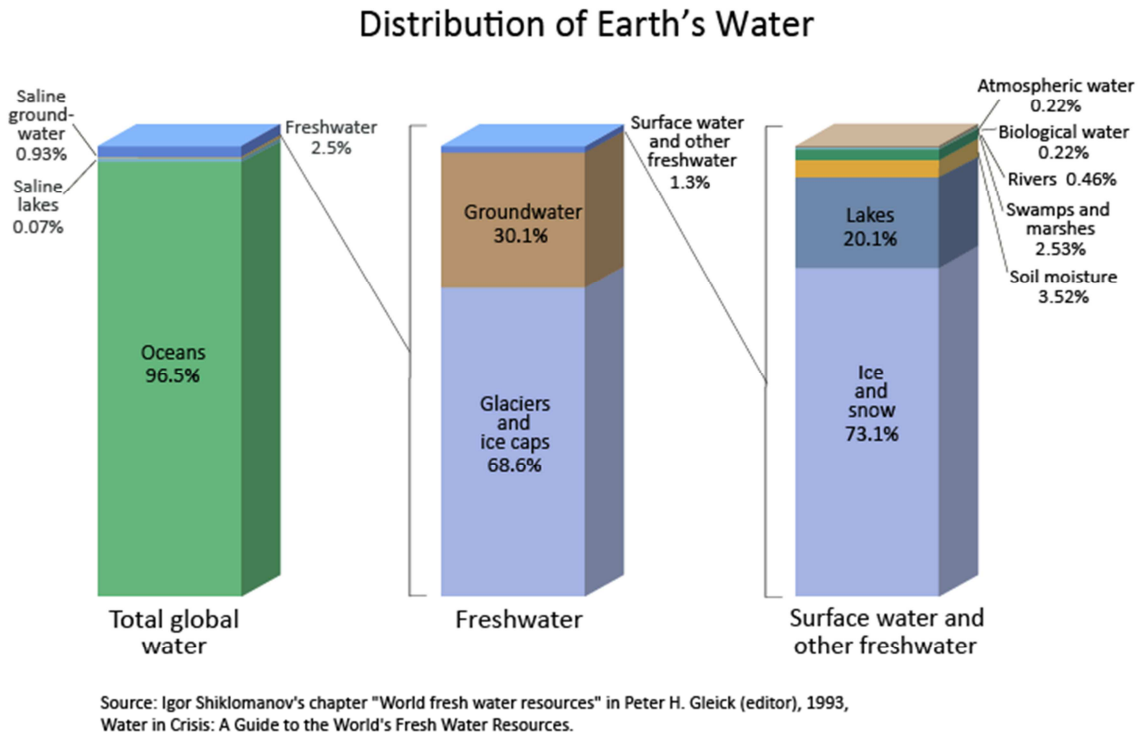


**Figure 1.** Distribution of Earth's Water (Source: http://ga.water.usgs.gov/edu/watercyclesummary.html).

Distribution of water on Earth is a dynamic process that is mostly controlled by the Sun. The Hydrologic Cycle, also called Water Cycle, describes the movement of water on the Earth. Different components are involved in this cycle according to

**Figure 2**, and as all the processes are connected, there is not a starting one. However, we will use the oceans as a starting reference for the Water Cycle description. Water from the oceans is evaporated with the energy reaching the surface of the Earth from the Sun. It is estimated that around 413,000 $km^3yr^{-1}$ of water is evaporated from the oceans (Syed et al. 2010). This evaporated water condensates at the upper atmospheric layers creating the clouds. The largest amount of water returns to the oceans as rainfall, around 383,000 $km^3\ yr^{-1}$ and the rest contributes to inland rainfall. Part of the inland rainfall is uptaken by vegetation and part of it is stored in the soil root zone area. It is estimated that soil root area contains about 58,100 $km^3\ yr^{-1}$ of water. The rest of this rainfall recharges ground water, rivers, lakes, runoff and returns, at the end, to the oceans closing the cycle. The water retained by plants, and in soil root zone returns to the atmosphere through evapotranspiration (ET). Ryu et al. (2011) indicated that inland plant transpiration and surface evaporation returns to the atmosphere 63,000 ± 13,000 $km^3\ yr^{-1}$, being plant transpiration responsible of 60% of the global ET. These numbers highlight the importance of monitoring processes occurring in the boundary layer between surface and atmosphere and are the base to carry out this research.

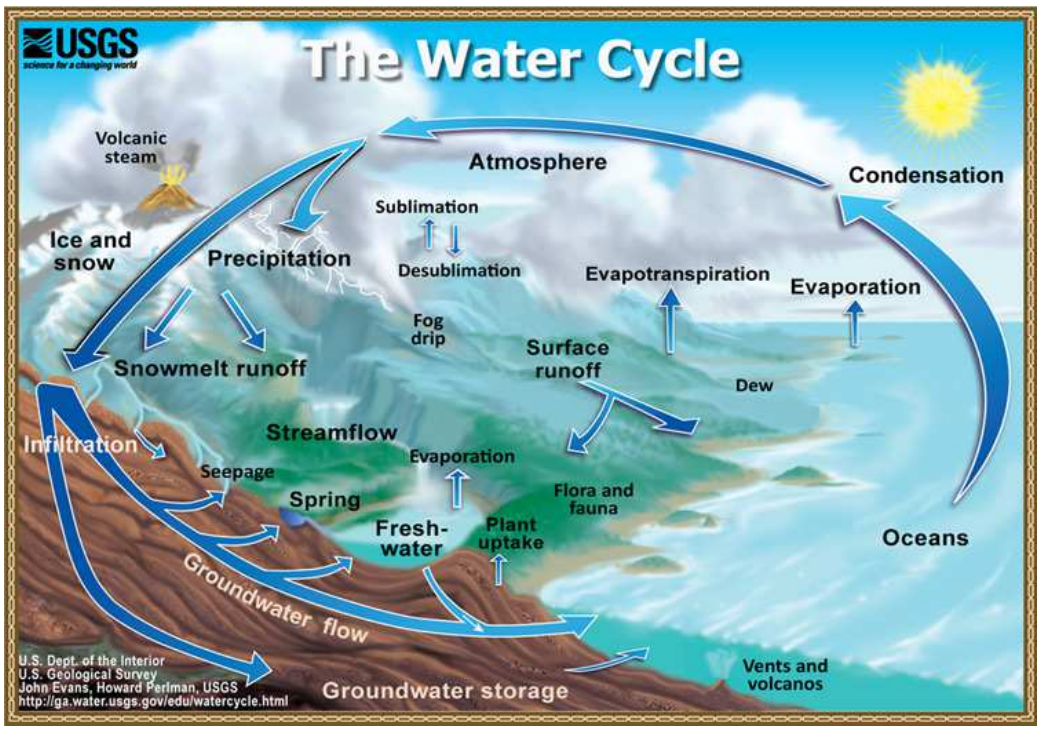


**Figure 2.** The Water Cycle diagram.
(Source: USGS, http://ga.water.usgs.gov/edu/watercycle.html).

The motivation to monitor the water fluxes between soil, vegetation and atmosphere using remote sensing is based on the relevance these processes have in the hydrological cycle. The aim to monitor SM is based on the fact that it affects different processes related to plant and soil properties. It is a controlling factor of plant growth as water transports the nutrient elements in the soil matrix and also limits the air content and gas exchange of the soil, and as a consequence, the respiration processes in the root zone (Campbell and Norman 1998). SM is critically involved in the energy and water balance of the land surface as soil water is taken by plant roots for photosynthesis and evaporated through transpiration (Monteith 1981). Monitoring vegetation water content, as well as other vegetation biophysical variables is motivated because water in leaves is a limiting factor for different physiological processes of vegetation and its deficit causes malfunctioning of different cellular processes. Water is involved in the thermal regulation of plant trough transpiration and also becomes crucial in the uptake of $CO_2$ for photosynthesis (Chaves et al. 2003). It is also fundamental to maintain turgor

pressure, which controls different functional parts of plants like cell enlargement or gas exchange (Taiz and Zeiger 2010). In addition, monitoring vegetation water content is fundamental for irrigation management to prevent vegetation water stress and in fire risk management (Chuvieco et al. 2004; Riaño et al. 2005; Verbesselt et al. 2007; Yebra et al. 2008b; Yebra et al. 2013). Monitoring other vegetation biophysical variables becomes also important when Radiative Transfer Models (RTM) or hydrological models are going to be used. These physical based models need to be parameterized or calibrated. In the case of RTMs, some of the most common variables are EWT, Dm (Jacquemoud and Baret 1990), or LAI (Verhoef 1985; Verhoef et al. 2007) among others as the number of variables depend whether the modeling is at canopy or leaf level, and the type of RTM. In the case of hydrological models, one of the most relevant vegetation parameters is the LAI (Stisen et al. 2008a) since it plays a crucial role in energy flux partition between soil and canopy as well as in rainfall interception. Therefore monitoring these vegetation variables is important not just to understand the ecosystem but for use as input parameters in different models. The fluxes from the surface to the atmosphere are relevant in agriculture, local climate and also affect the $CO_2$ assimilation by the plants. Daily ET can be estimated using the existing relationship with EF if assumed constant during the day, however, if this assumption is not completely true can lead to large errors in the final estimate, hence this fact needs to be validated to obtain accurate daily ET retrievals.

All these processes vary rapidly on time and space and, even if they can be measured *in situ,* the collection of the measurements is very time consuming, expensive and usually impossible to gather all the variability. Remote sensing is the most suitable tool to monitor these processes at an adequate spatial and temporal sampling. Space platforms observe the Earth surface and provide information with different spectral, temporal and spatial resolutions. Boundary layer processes like vegetation water content, SM and ET are very dynamic and can rapidly change in time; therefore monitoring them requires a high revisit frequency. With the current technology, this high temporal resolution is only achieved using platforms that

provide data at coarser spatial resolution which makes the validation with *in situ* data more difficult (Li et al. 2008; McCabe and Wood 2006). It is therefore necessary investigating the processes at different spatial and temporal scales in order to improve our understanding of the relationships between the variables measured *in situ* and those calculated using remote sensing data (Anderson et al. 2007) so more reliable estimations can be achieved.

## 1.1 Vegetation Water Content.

Measuring the content of vegetation is not a trivial task and indeed many metrics have been proposed in the literature. These metrics have been used and defined differently for a wide range of applications such as fire risk/spread modeling or plant productivity. There are different metrics to quantify vegetation water content. Fuel Moisture Content (FMC) (Desbois et al. 1997), for instance, is defined as the mass of water per unit mass of vegetation and, has been extensively used to estimate the fire risk occurrence and fire propagation (García et al. 2008; Yebra et al. 2008b). Equivalent Water Thickness (EWT) or Leaf Water Content (LWC), defined as the mass of water per leaf area, measures the thickness of the water layer with the same leaf area (Danson et al. 1992). Several studies showed that EWT can be retrieved from spectral information at leaf level as it is directly related to the water absorption depth of leaves (Ceccato et al. 2001; Datt 1999). FMC and EWT are related each other since EWT can be expressed as the product of FMC and the dry matter (Dm), the later one defined as the ratio of leaf dry weight and leaf area (Bowyer and Danson 2004; Chuvieco et al. 2003). Finally, another metric is the Canopy Water Content (CWC), the mass of water in the canopy per ground area (Cheng et al. 2008; Trombetti et al. 2008). Therefore, CWC represent the product of EWT and Leaf Area Index (LAI), offering not just information at leaf level but at canopy level.

Field sampling of FMC, EWT or CWC relies usually on gravitational methods but these methods are quite limited for estimates at regional to global spatial scales,

since it requires interpolation to bridge the gaps in both time and space. Monitoring vegetation water content with remote sensing benefits agriculture, to control crop production and prevent stress in plants (Peñuelas et al. 1992; Sepulcre-Cantó et al. 2006) and forestry, to assess fire danger associated with vegetation water conditions (Chuvieco et al. 2003; Chuvieco et al. 2004; Chuvieco et al. 2009; García et al. 2008; Yebra et al. 2008b).

In order to estimate plant water content with remote sensing, vegetation spectral reflectance has been primarily related to specific water absorption bands in the Short Wave Infrared region (SWIR, 1300-2500 nm) (Ceccato et al. 2001; Zarco-Tejada et al. 2003). Other studies related vegetation water content to spectral indices that do not include SWIR data. These indices monitor the vegetation water content by indirectly relating it to another biophysical parameter that is used as a proxy of water stress. This is the case of the Normalized Difference Vegetation Index (NDVI) (Rouse et al. 1973), with bands in the Visible (VIS) and Near Infrared (NIR) spectral region, which has shown a close relationship between vegetation biomass and chlorophyll content with the water content in grasslands (Chuvieco et al. 2003; Chuvieco et al. 2004; García et al. 2008; Yebra et al. 2008b). Least squares regression models have served to empirically relate observed measurements of water content to spectral indices. These models have their weakest point of being site dependent, requiring long datasets for calibration (Chuvieco et al. 2009) and showing different results when the models are extrapolated to other sites using different data sets, making difficult their applicability (Riaño et al. 2005; Yebra et al. 2008a). RTMs on the other hand simulate vegetation spectra based upon physical laws and are a sound alternative to empirical modeling. They can be applied to different locations to estimate different vegetation parameters, as long as the RTM is a realistic representation of the vegetation canopy. For example, Trombetti et al. (2008) predicted CWC for the continental US using PROSAILH (Baret et al. 1992) simulations. This model was calibrated with CWC from the Airborne Visible/Infrared Imaging Spectrometer (AVIRIS) hyperspectral water absorption bands. AVIRIS is capable of retrieving CWC as it can simultaneously estimate water

vapor and liquid water based on principles of spectroscopy (ACORN, ImSpec LLC, Analytical Imaging and Geophysics LLC, Boulder, CO), when using a RTM approach based on MODTRAN model. AVIRIS CWC estimates have been already validated in different studies (Gamon et al. 1993; Green et al. 1993; Sims and Gamon 2003). Trombetti et al. (2008) first created 600 PROSPECT-SAILH (Jacquemoud and Baret 1990; Jacquemoud et al. 1995) synthetic MODIS simulations based on a field data base. Later, based on these simulations 60 MODIS band combination were used to train the Artificial Neural Network (ANN) and AVIRIS CWC to calculate the calibration equation for each vegetation type. Another example is Jurdao et al. (2013) who inverted the RTM GEOSAIL (Huemmrich 2001) to estimate in their case FMC, which was then validated with extensive field sampling in Spain.

The objective of this part of the study is to investigate the relationship of three vegetation metrics (FMC, EWT, CWC), Dm and LAI and spectral information. To our knowledge there is not any study that analyzes three vegetation water content metrics simultaneously. This makes the comparison between them difficult, as the data sets usually are not comparable. Due to the different physical meanings of each metric, the spectral relationships should not be the same, and therefore this needs to be done using the same data set. This evaluation will show which metric can be retrieved more accurately using spectral information and the best regions of the electromagnetic spectrum for each metric. The next objective will assess the differences observed between field scale and satellite. Many studies have established empirical relationships between data collected *in situ* and spectral information from different sources. Within the area covered by a low spatial resolution pixel, there is the chance that the measured variables could vary in space due to different SM conditions, illumination and other climatic factors. It is therefore important to assess these variations and evaluate field protocols improving and modifying them in the weakest points, either increasing or reducing the sampling spatially or temporary. Validation of RTM estimates is a task that has to be carried out over different environments and ecosystems in order to ensure their applicability. In this study we propose to evaluate and compare the estimates

of two physical models, one that estimates FMC (Jurdao et al. 2013) and a second one that estimates CWC (Trombetti et al. 2008) against the estimates using empirical models.

## 1.2 Soil Moisture.

Given that SM at the root-zone is affected by rainfall, evapotranspiration processes and soil properties, one of the main difficulties of monitoring SM is to characterize its spatial and temporal variability. Indirect, accurate and continuous SM measurements can be obtained using a certain range of ground instruments and methods, such as the Time Domain Reflectometry (TDR). However, these ground measurements are very limited and hence they do not represent the spatial variability of SM. Earth Observation (EO) satellite platforms can be a powerful tool to overcome the limitations of ground sensors and spatialize this variable, since SM affects the emission and absorption of electromagnetic radiation in different regions of the spectrum:

- Microwave (MW) backscattered or emitted energy from/by the ground surface allows relating the dielectric constant with SM (Schmugge 1978);
- when the soil is wet the energy balance of the surface is controlled by soil evaporation and vegetation transpiration and, hence, lower surface temperatures are expected in wet soils than in dryer soils during daytime hours (Schmugge 1978). This effect can be captured in the Thermal Infra-Red (TIR) region of the electromagnetic spectrum. Additionally, if multiple observations of the land surface are taken at different times throughout the day they can be related to the soil thermal inertia (Wang et al. 2006b) and consequently to SM (Minacapilli et al. 2009); and
- in the optical domain (350-2500 nm), an increase of SM produces an overall decrease in albedo (Bach and Mauser 1994). Water-specific absorption features in the Short-Wave Infrared Region (SWIR), ranging from 1000 to 2500 nm, are sensitive to vegetation water content (Ceccato et al. 2001).

Each of these spectral regions has its own advantages and disadvantages for mapping SM (Kerr 2007; Moran et al. 2004). MW sensors are insensitive to atmospheric disturbances, but they usually require larger pixel size (10: 1 orders of magnitude) to be compared with sensors in the optical or thermal infrared domain, due to the lower emitted energy in the microwave (MW) region. This is the case of the most recent missions dedicated to monitor SM, the Soil Moisture and Ocean Salinity (SMOS) (50 km) or the future Soil Moisture Active Passive (SMAP) with 40 km resolution in its MW radiometer.

Regarding optical and TIR sensors, they allow a higher spatial and/or temporal resolution than MW sensors but they are greatly affected by the atmosphere. Different methods have been proposed in the literature to combine thermal information with visible and near infrared data in order to estimate the root-zone SM. This is the case of the Temperature-Vegetation Dryness Index (TVDI) (Sandholt et al. 2002), also known as the triangle method (**Figure 3**), since it delimitates empirically the triangle formed when plotting many different cases of the Surface Temperature (Ts) versus a Vegetation Index (VI) (Carlson et al. 1995; Carlson et al. 1990; Moran et al. 1994; Sandholt et al. 2002; Sun et al. 2012). This method was first used by Price (1990) based on the different thermal properties of soil and vegetation: for equal weather forcing conditions soil and vegetation temperatures differ and this fact explains why the Ts/VI scatter plot within a spatial window shows a typical triangular shape (Sandholt et al. 2002). Moisture availability (very wet to very dry range) and fractional vegetation cover will also affect the shape of the Ts/VI space (Carlson et al. 1995). The upper boundary is called “dry edge” and represents dry soils and stressed vegetation where ET does not occur and hence surface temperature is maximum. The “wet edge” establishes the lower boundary that corresponds with wet soils and unstressed vegetation where ET occurs near its potential rate and thus surface temperature is minimum and close to the air temperature. Between the two edges, all intermediate conditions occur, and SM can consequently be represented in the Ts/VI triangle space (**Figure 3**).

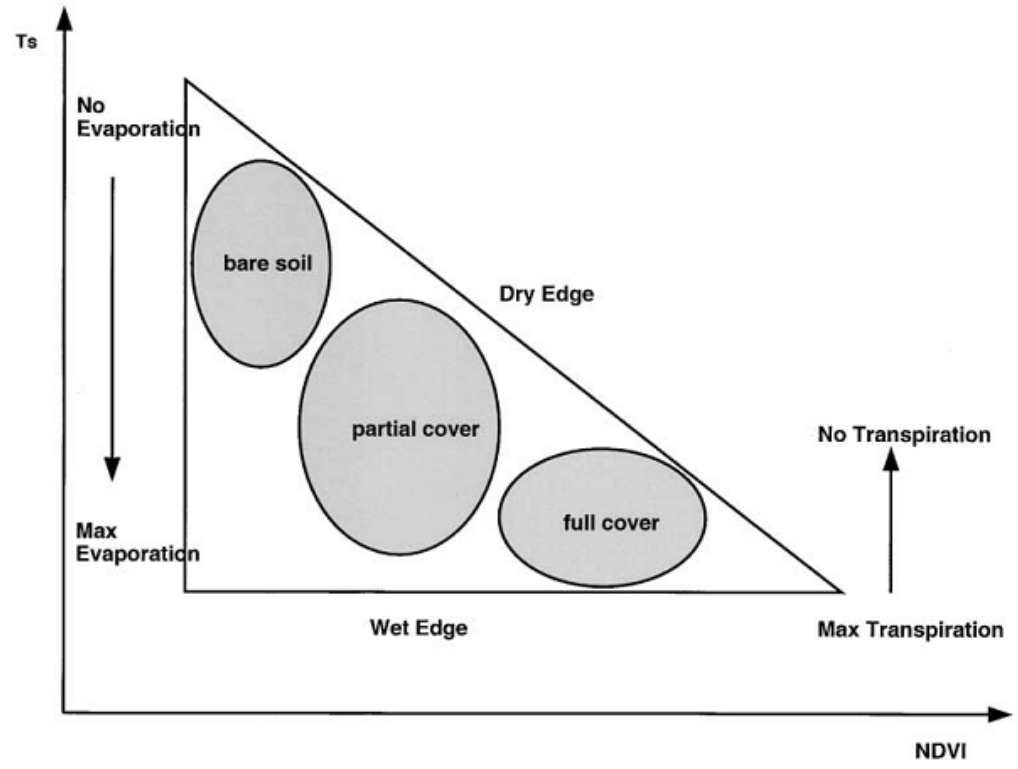


**Figure 3.** Ts/VI space diagram. Taken from (Sandholt et al. 2002).

One of the key issues in this method is the definition of the edges of the triangle. While some studies used ancillary meteorological data to invert an ET model, for instance using the Penman-Monteith ET equation (Moran et al. 1994), others used the information contained in the Ts/VI space to empirically retrieve the edges (Sandholt et al. 2002; Tang et al. 2010). In any case, several assumptions and prerequisites need to be taken into account when applying the triangle method: 1) uniform atmospheric forcing together with the presence of all moisture and vegetation cover conditions are needed within the spatial domain applied (Stisen et al. 2007); 2) the dimensions of this spatial domain have to be large enough to collect a sufficient amount of Ts/VI cases to the adequately define the triangle shape; and 3) factors such as land cover type and topography should also be taken into account to ensure the applicability of the method (Hassan et al. 2007).

Different land cover types inside the spatial domain of the Ts/VI space may modify the edges of the triangle. Smith and Choudhury (1991) showed the effects of

combining crops and forest in the definition of the triangle. Vegetated surfaces, in particular forests, have a higher roughness than non-vegetated ones. This affects the way the heat is dissipated from the surface at equal wind conditions, being less effective in rough surfaces compared to areas with bare soil or low vegetation. In addition, including areas with significant differences in altitude can affect to the condition of atmospheric homogeneity within the Ts/VI space, with air temperature changes caused by the adiabatic lapse rate. On the other hand, areas with high slopes or different exposures, besides of their higher difficulty in the retrieval of Ts with satellite remote sensing, also lead to changes in solar irradiance, possibly breaking the assumption of uniform meteorological conditions. Therefore, the size of the spatial window where the Ts/VI space is represented needs to be selected according to the abovementioned requisites. A very small window will ensure homogeneity in the atmospheric conditions, but there are chances of not finding all the SM and land cover conditions in the area. A larger window can solve this problem but topography and different land cover types may affect the applicability of the method, in particular over heterogeneous areas.

One of the decisions that need to be taken when using the triangle technique to determine the TVDI is the method election to calculate the edges. To the best of our knowledge, there are no studies in the literature in which the evaluation of different methods for bounding the wet and dry edges has been done; furthermore the question is whether this election has a further implication in the final model performance of the TVDI. Therefore in this study we propose to evaluate two different methods to calculate the edges of the triangle, and assess if this election has any consequence in the model performance of TVDI. Furthermore, the SWIR region of the spectrum has been proven to be the most sensitive region of the electromagnetic spectrum to moisture. Based on this, we propose a substitution of the NDVI by NDII. The hypothesis to carry out this modification is based in the fact that while NDVI can distinguish between areas with soil, partial cover and vegetated, the use of NDII offers more information on the moist status as the index will not just be sensitive to vegetation but also to the moisture conditions of

vegetation and soil. Additionally several studies have shown that SWIR index are higher correlated to LAI than NDVI therefore the edge delimitation and consequently the triangle technique can be improved.

### 1.3 Evapotranspiration and Evaporative Fraction (EF).

ET is one of the most important components on the water cycle (Jasechko et al. 2013). ET, also named latent heat flux (LE) when it is expressed in energy units, can be measured *in situ* using different techniques; such as Eddy Covariance, Bowen Ratio-energy Balance or using lysimeters. However these measurements are again, local and difficult to extrapolate at regional or global scales.

In the last decades, remote sensing has allowed regional/global estimation of ET using different models and sensors. A review of those methods can be found in Li et al. (2009). Since remote sensing methods cannot directly estimate ET, in most cases spectral data are used as proxies related to ET or to derive inputs mainly related to the estimation of the sensible heat flux for land surface models. These methods can be divided in three large groups. The first one includes empirical methods that do not need ancillary data such as the Simplified Equation method (Jackson et al. 1977; Seguin and Itier 1983) and the triangle method Jiang and Islam (2001); (Stisen et al. 2008b). The second group corresponds to the semi empirical methods. Some of them require the identification of anchor pixels with maximum ET and ET= 0, as well as other meteorological ancillary data to be operative. In this group we include the Surface Energy Balance Index (SEBI) (Menenti and Choudhury 1993), the SEBI simplified version S-SEBI (Roerink et al. 2000), the Surface Energy Balance Algorithm (SEBAL) (Bastiaanssen et al. 1998) and the Mapping Evapotranspiration with Internalized Calibration (METRIC) model (Allen et al. 2007). The third group corresponds to the physical methods such as the family of Two Source Energy Balance (TSEB) models (Kustas and Norman 2000): the Atmosphere-Land Exchange Inversion (ALEXI) (Anderson et al. 1997), the linked version with a canopy RTM Two Source Energy Balance Dual Angle Radiative

Transfer (TSEB-2ART), (Guzinski et al. 2014; Nieto et al. 2013) or the Dual Time Difference (DTD) (Guzinski et al. 2013).

Most of these methods make use of remotely sensed Land Surface Temperature (Ts) and hence the ET retrieved is an instantaneous estimate during the satellite overpass. In order to have ET estimates at daily scale the estimation of daily Evaporative Fraction (EF) offers some advantages. EF represents the proportion of available energy that is used for evapotranspiration.

$$EF = \frac{LE}{R_n - G} = \frac{LE}{LE + H} \qquad \textbf{(Equation 1)}$$

where $R_n$ is the net radiation, G is the soil heat flux, and H is the sensible heat flux.

Daily ET can then be obtained from EF assuming the self-preservation of EF along daytime (Brutsaert and Sugita 1992; Crago and Brutsaert 1996; Sugita and Brutsaert 1991). However, there is some controversy on whether EF can be assumed constant under sunny day conditions (Crago and Brutsaert 1996; Shuttleworth et al. 1989). A recent study (Peng et al. 2013) analyzed the relationship between *in situ* instantaneous EF and daily EF using a large dataset from the FLUXNET network (http://fluxnet.ornl.gov/). Results showed that there is a strong relationship between daily and instantaneous EF, but this relationship is weather, ecosystem and time of the day dependent.

Gentine et al. (2007) analyzed the EF diurnal behavior linking a SVAT model with micro-meteorological data in a typical Mediterranean semi-arid region. Variables affecting the diurnal EF evolution are presented for canopy EF ($EF_C$), soil EF ($EF_S$) and for the total EF in the study, showing that LAI and SM can strongly modify the EF values during daytime. The study also concluded that $EF_S$ component can be assumed constant during the day, which differs in the case of $EF_C$ as the latter shows strong variations during the day.

In some ecosystems, such as the semi-arid ones the most limiting factor that controls ET is the SM (Gentine et al. 2007; Stisen et al. 2008b) and consequently, in the case of EF, SM has also a great importance (Gentine et al. 2007 ). EF is less

affected by atmospheric forcing factors like incoming solar radiation or wind speed than ET is (Gentine et al. 2011). One of the simplest methods in estimating ET or EF from remote sensing is as well the triangle method since it only relies on remote sensing data and is easy to calculate with acceptable results obtained so far. The triangle method applied to EF estimation was originally proposed by Jiang and Islam (2001) and is based on the simplified expression of the Penman-Monteith's equation (Monteith 1965) developed by Priestley and Taylor (1972) for estimating potential ET. In that formulation the aerodynamic resistance in Pennman-Monteith's model is summarized in a single term, leading the equation as follows:

$$LE = \phi \left[ (R_n - G) \frac{\Delta}{\Delta + \gamma} \right] \qquad \textbf{(Equation 2)}$$

where $\Delta$ is the slope of the saturated vapour pressure curve (kPa $C^{-1}$), dependent of the air temperature, and $\gamma$ is the phsycometric constant (kPa $C^{-1}$). The term $\phi$ is a substitute of the Priestly-Taylor constant (α), which is usually agreed to be 1.26 under equilibrium conditions over wet surfaces (Eichinger et al. 1996). By combining **Equation 1** and **Equation 2**, EF can be expressed as:

$$EF = \phi \left[ \frac{\Delta}{\Delta + \gamma} \right] \qquad \textbf{(Equation 3)}$$

where the $\phi$ parameter of the equation can be empirically obtained using the triangle technique (de Tomás et al. ; Jiang and Islam 2001; Stisen et al. 2008b; Tang et al. 2010) by considering a value of 1.26 when ET is maximum (wet edge) and a value of 0 when ET is minimum (dry edge) (Jiang and Islam 2001), with all the intermediate values between both edges. However, It is not well understood the existing relationship between $\phi$ parameter in the Ts-VI triangle space. Some authors (Stisen et al. 2008b) proposed for instance a double interpolation using a second order polynomial equation to define the $\phi$ isolines (**Figure 4**), assuming that the estimated dry edge deviates from the theoretical dry edge (where ET is actually 0)

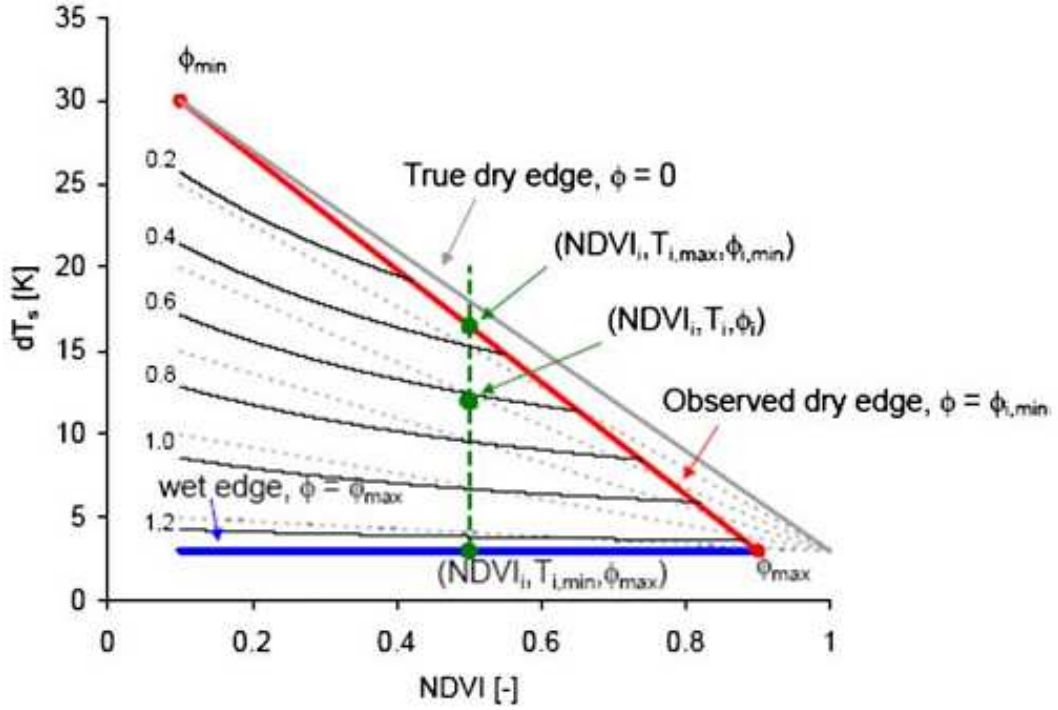


**Figure 4.** Scheme showing the triangle edges and the quadratic interpolation of $\phi$ compared to the linear method. Taken from Stisen et al. (2008b).

Finally, one of the challenges when using satellite remote sensing data to estimate ET/EF is model validation, as there is usually a scale mismatch between *in situ* measurements and the satellite data. Furthermore, since one of the most widely *in situ* ET/EF measurements currently used are based on EC data the validation becomes even more challenging as the footprint measured by the EC system is very variable due to changes in vegetation roughness and turbulence (Section 2.3). Therefore in this study we aim to validate the remote sensing estimates of EF using the footprint contributions calculated using the EC data. Although this validation has been carried out to validate ET models, this has never been done in the case of EF. Landsat was selected to carry out this comparison due to the pixel resolution of 30 m. The triangle method will be used to retrieve EF; however, in this case we propose using a LAI product from MODIS. The decision to use LAI rather than a VI is based on the strong relationship between LAI and EF described in Gentine et al. (2007). In addition LAI is a more physical variable of the vegetation which provides more control on the calculation of the edges of the triangle rather than a Vegetation

Index (de Tomás et al. 2014). We will downscale this product from its original resolution of 1 km to 30 m using a regression decision tree algorithm. The reason to use this product rather than the one measured in the field is that we consider that due to the sparse tree distributions at the study site, the proportion of canopy and grassland can be highly different within one pixel. We believe that using the proposed methodology the errors in the LAI calculation for each pixel will be smaller than using empirical models and consequently the calculation of the edges of the triangle will be more accurate too. Our hypothesis is that when using the footprint contributions the results should be more accurate than if just the value of a single pixel over the EC tower is used for the validation, therefore another question that we plan to answer in this study is how different are the results if instead of using the footprint contributions a single pixel corresponding to the EC is used. Daily EF and overpass EF coincident with Landsat will be calculated using the EC data and compared against Landsat EF.

# 2 Data acquisition

An overview of the data used in the thesis is presented in this section. The main objective of data acquisition is to calibrate and validate the models in the different studies of this thesis. This part is organized in different subsections:

1. Site description
2. Vegetation biophysical variables
3. Eddy covariance flux measurements
4. Soil moisture measurements
5. Remote and proximal sensing data

The acquisition was conducted for 2 years (2009/2010) in Las Majadas del Tiétar. In **Figure 5** it is presented a summary of the data sources used to carry out this research. They are divided in two sources, remote sensing data that are surrounded by a green box and *in situ* data that are surrounded by a blue box. Both sources merge in the middle of the figure, showing in which chapter of the thesis the different data have been used.

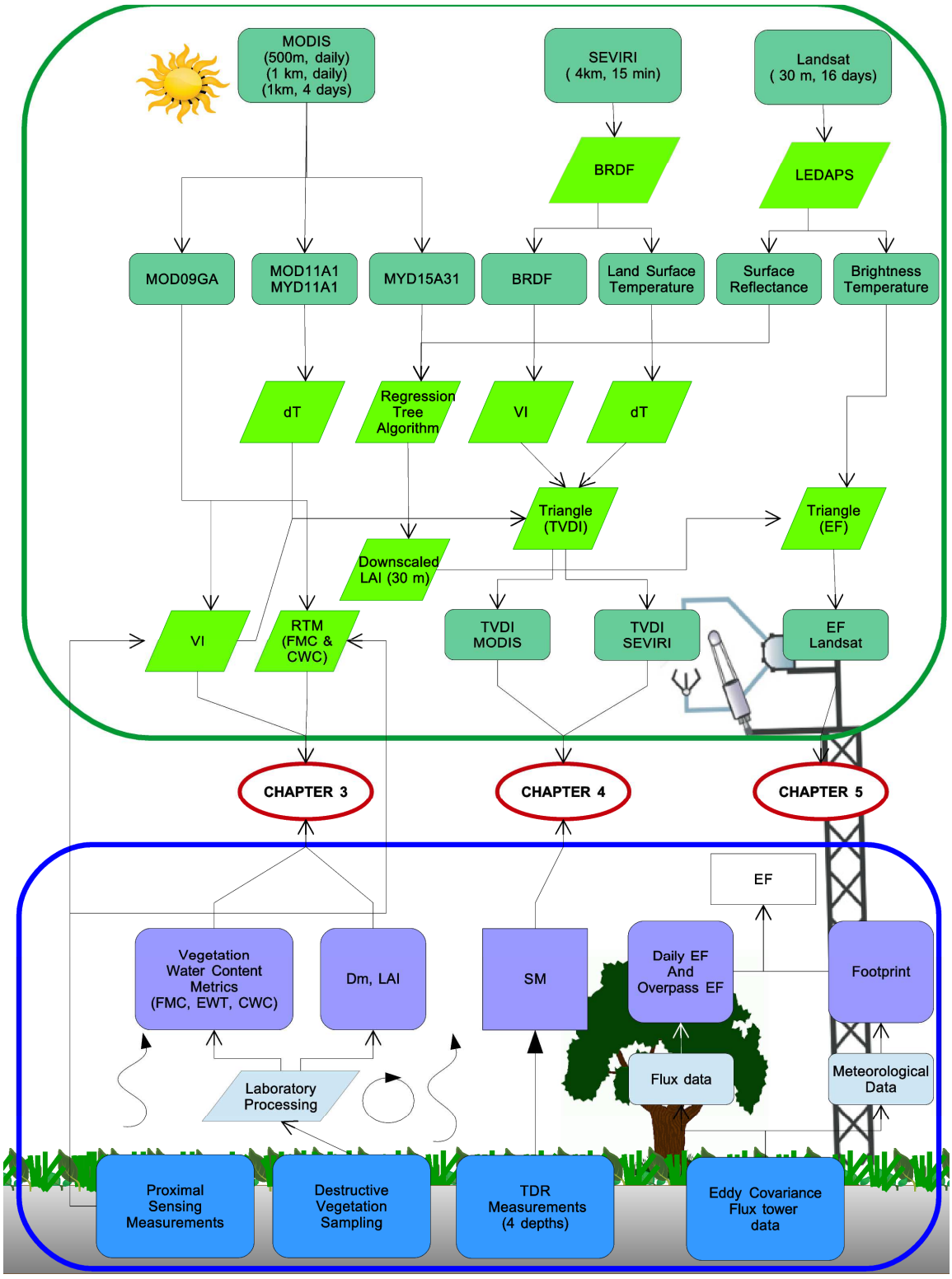


**Figure 5.** Scheme summarizing the data used during this research.

## 2.1 Site description

The study site is located at Las Majadas del Tiétar, Cáceres (Spain) FLUXNET site (http://fluxnet.ornl.gov/site/440) (**Figure 6**).

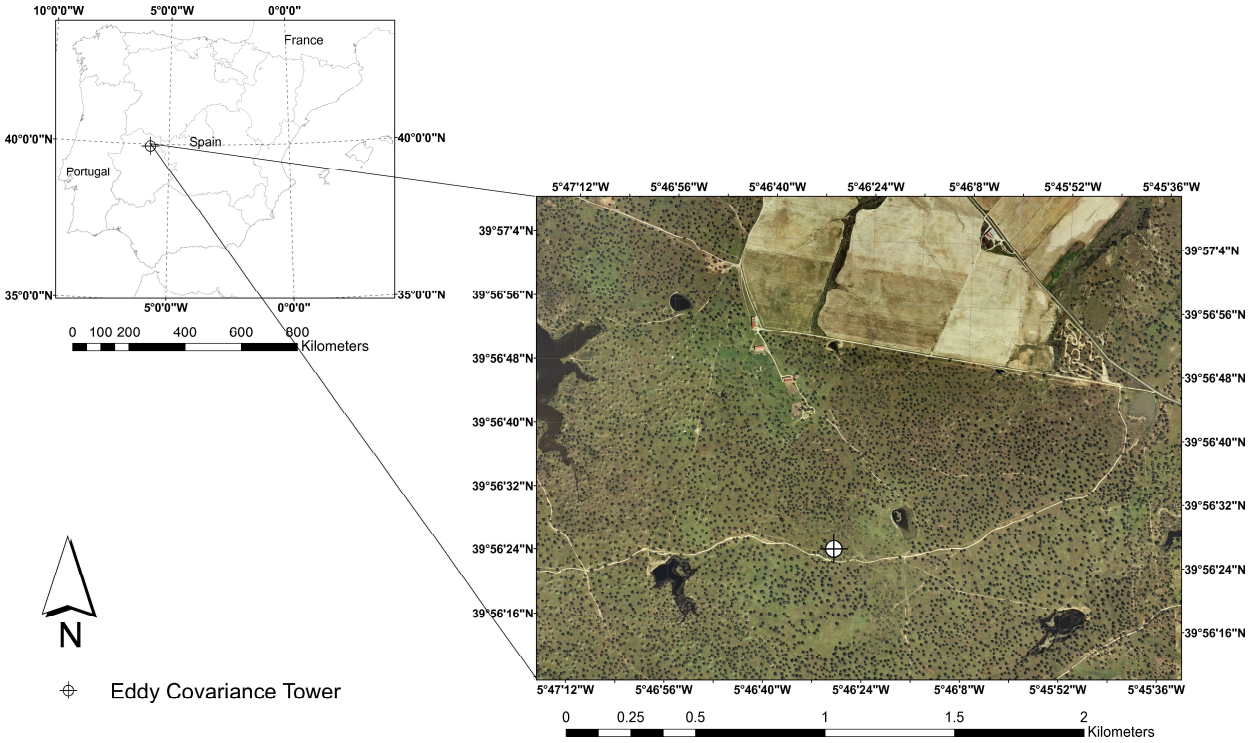


**Figure 6.** Las Majadas del Tiétar study site location.

The area is a Mediterranean wooded grassland ("dehesa"), an ecosystem that occupies about 4% (2.5 Mha) of the Iberian Peninsula (Castro 1997). Common tree species are different varieties of oaks, here mostly *Quercus ilex* subsp. *ballota* (L.), whose acorns and leaves are mainly used as forage for pigs and cows, respectively. The scattered oak trees have a 9 m mean height and 6 m mean crown diameter. Due to its deep and wide root system, this species is resistant to long drought periods (Camarero et al. 2012). Short grassland covers 86% of the area that is managed for cow shepherding. It is mainly composed by *Rumex acetosella,* L., *Plantago carinata* Schrad*, Trifolium subterraneum* L., *Cynodon dactylon*(L.) Pers., *Taraxacum dens - leonis Desf.* and *Vulpia myuros* (L.) C. C. Gmel. During the summer, grassland dries

out rapidly and turns into dead matter. Summers are hot and dry, with 30 °C daily average temperature and only 67 mm total precipitation, which are not representative of mean annual 16.7 °C and 572 mm. The average altitude is 256 m above mean sea level. Soils are lixisols with an average thickness of 80 cm. Due to the presence of a clay layer in some of the areas, small water pools may appear in winter after rainy periods. The occurrence of this type of ecosystem in Mediterranean areas worldwide, the need to track the responses to water stress conditions, together with the presence of a FLUXNET eddy covariance flux tower justifies the selection of this site.

## 2.2 Vegetation Biophysical variables

In this work, three different vegetation water content metrics of grassland expressed as Fuel Moisture Content (FMC), Equivalent Water Thickness (EWT) and Canopy Water Content (CWC) as well as other important biophysical variables such as Leaf Area Index (LAI) and Dry Matter (Dm) were calculated. A spatial sampling was established centered in the Eddy Covariance (EC) flux tower using a random sampling scheme. Three sampling zones were defined as concentric rings around the EC by incrementing the radius at equal intervals of 150 m. The number of plots inside each ring was decided accounting for two parameters, the distance to the EC and the area of each ring. A total of 34 square plots with 25m side were randomly located around the EC tower. Plots were marked in the field using 4 stakes, one for each corner (NW-NE-SW-SE). The stakes were positioned in the field with a Leica D-GPS. A color code was used to differentiate the plots in the field according to the sampling zone. Each of the stakes was labeled indicating the zone and plot and also the orientation. This helped the location of the plot once any of the stakes had been found.

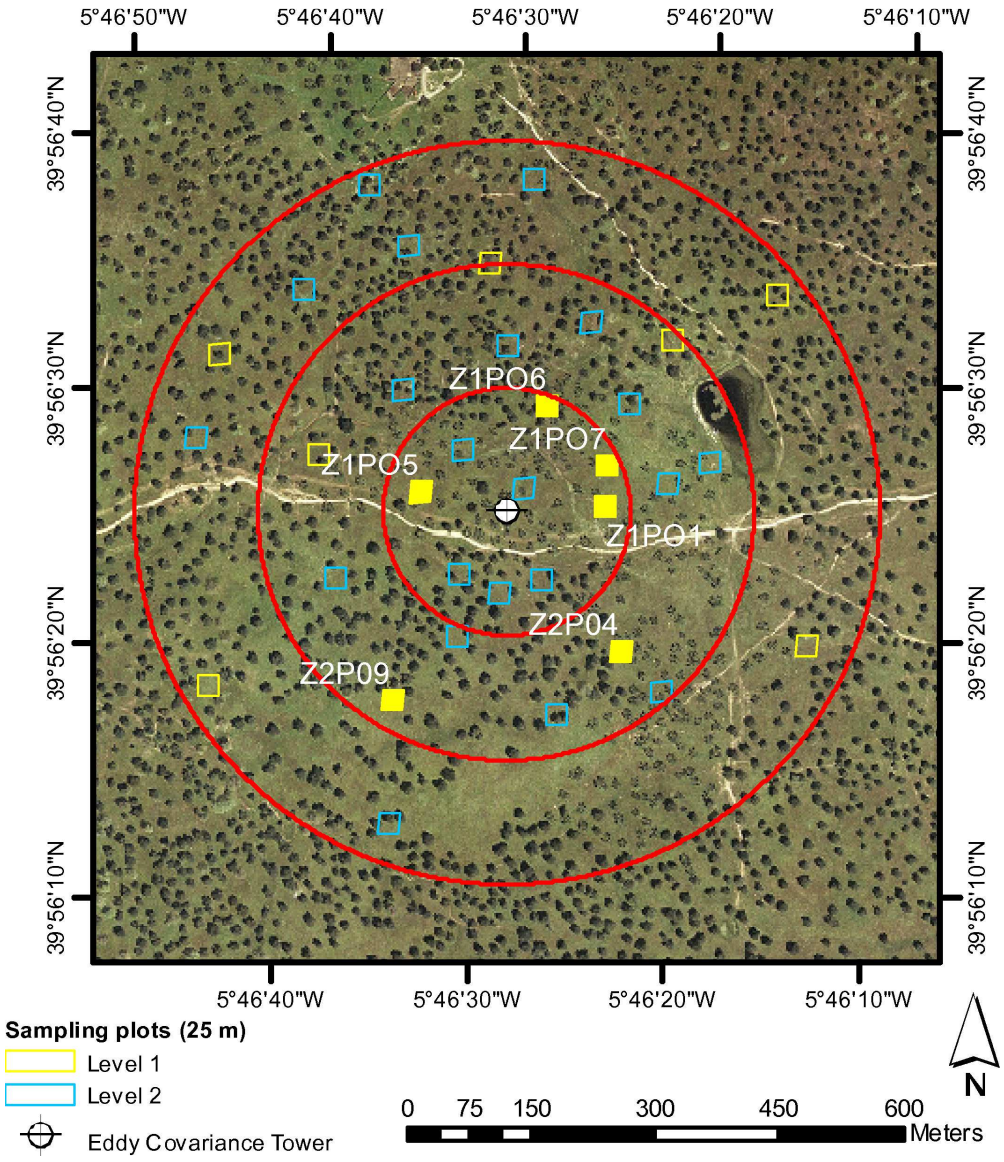


**Figure 7.** Grassland sampling design centered at the EC flux tower showing the two levels initially planned in the sampling strategy. Solid plots indicate those plots that are within the MODIS pixel corresponding to the EC tower.

Then the plots were split in two sampling levels (**Figure 7**) leading to 13 plots for level 1, and 21 for the level 2. Temporal sampling was established to be coincident in time with Landsat 5 and Landsat 7 overpasses, where level 1 plots were sampled coincident with Landsat 5 and level 2 plots with Landsat 7. This intensive strategy would provide up to three measurements every month (**Figure 8**). However, after one year following this sampling strategy, a test was carried out

to evaluate differences between sampling levels using a Kruskal-Wallis non-parametric test. The results showed that there were not statistically significant differences between levels, and therefore the decision of continuing with only one that the level coincident with Landsat 5 overpass was taken. The period covered with this scheme was from April 2009 to April 2011. Furthermore, data collection was only performed after assuring that no rain was forecast during the sampling date and neither occurred in the two previous days in order to avoid collecting superficial water on the leaves.

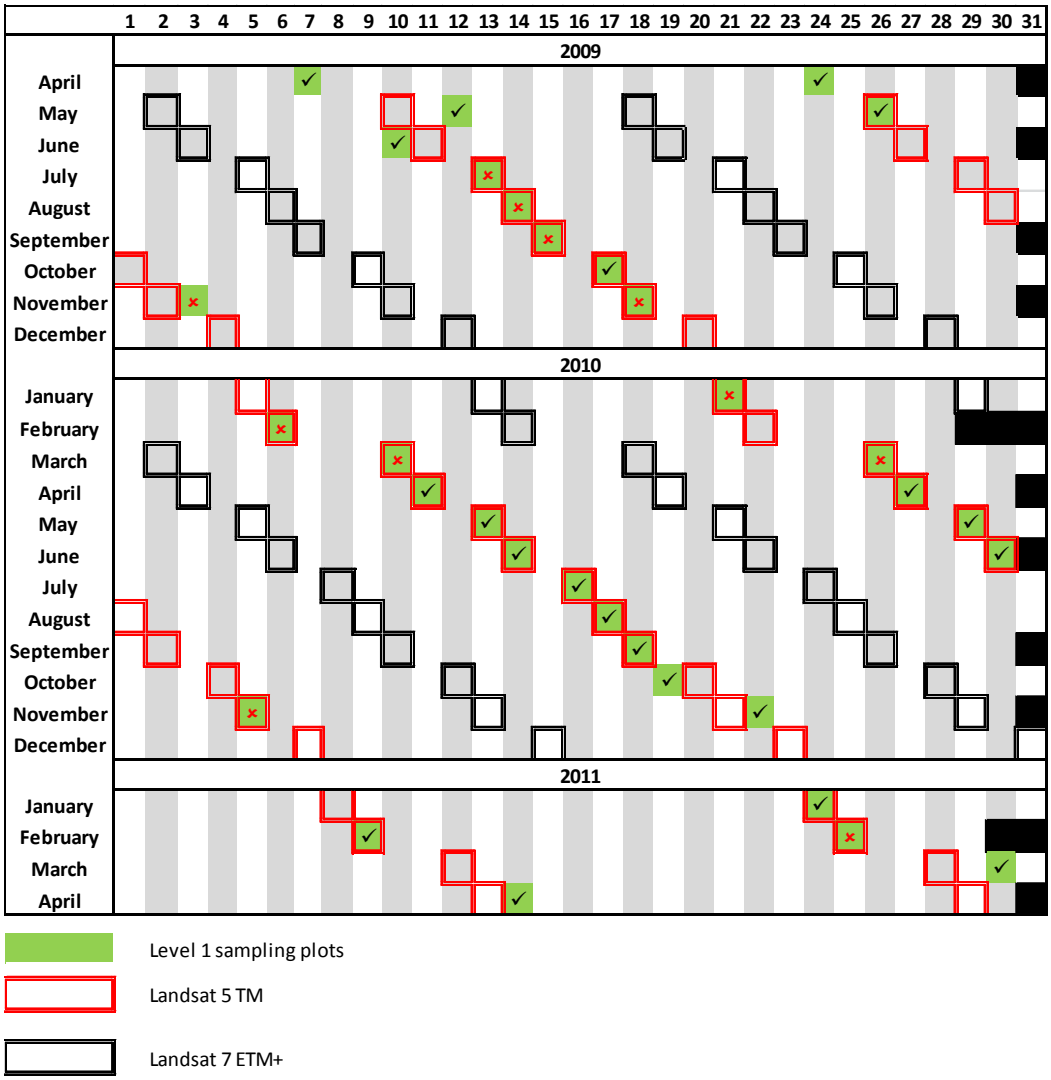


**Figure 8.** Calendar showing the temporal sampling scheme: ✓ denotes data used in the study and × denotes discarded data. Green indicates level 1.

During the summer, the herbaceous layer became completely dry in the study site. Consequently, during the first year it was decided to avoid collecting data during the summer period. However, after analyzing the data, we realized that this strategy would create some inconsistency to follow the temporal evolution of some of the biophysical variables measured, mainly LAI, hence, in order to ensure the time series continuity of at least one phenological year, sampling was conducted throughout the summer of 2010.

Since a part of the personnel in charge of data collection varied during the different campaigns, protocols were established in order to guide the field sampling processes. These protocols described the material and method in a comprehensive and unambiguous way so the homogeneity of the dataset could be ensured.

### 2.2.1 Field Data collection

Three grassland samples were collected from three 25 x 25 $cm^2$ quadrants randomly located within each 25 x 25 m plot. Once the operator reached the plot, he/she positions backwards to it. Then he/she randomly throws in the air the quadrant, falling into the plot and collects the sample at the point the quadrant landed (**Figure 9**a). Each operator was equipped with pen, clippers, zip plastic bags and notebook. Before starting the sampling collection, the operator checks the status of the sample and writes down any incidence related to it. Zip plastic bag are identified writing down on it the ID of the plot, the date and the type of sample collected.

a) b) c)

**Figure 9.** a) Field instrumentation consisting on a 25x25 cm quadrant, clippers, field notebook, zip plastic bags and pen. b) Picture of a frame after the sample has been collected and kept in the zip bag. c) Weighting of collected samples in the field in the trunk of the car to avoid wind during the weighting process.

All rooted plants within the quadrant were collected using the clippers (**Figure 9a,b**) and kept in a zip plastic bag. Additionally, a smaller sample was collected outside of the quadrant but nearby to estimate EWT ($EWT_{Sample}$ hereafter). As EWT requires knowing the leaf area of the sample, this was considered a cost-effective method, since scanning all collected sample inside the quadrant would have been unaffordable with the staff available. On the other hand, using a subsample from the quadrant sample would have introduced uncertainties in the data due to possible loss of fresh weight while it was kept in the zip bag. Sampling personnel was adviced to try to ensure that a representative proportion of surrounding species was kept in the $EWT_{Sample}$. However, the selection of the individuals to be included in the sample depended on the particular criteria of each person so it is not free of potential bias. All samples were weighted in the field using a scale with 0.01 g precision (**Figure 9c**) and then transported in a cooler to the laboratory. Any possible anomaly found during sampling, i.e. superficial wetness, difficulties to remove the soil from the sample or any other incidence, was annotated in the plastic bag to document potential inconsistencies found during the laboratory analyses. Upon arrival to the laboratory, all samples were relocated in a refrigerator and kept there until processing of the samples was carried out.

### 2.2.2 Laboratory processing

After each field campaign the samples were further processed in laboratory in order to obtain the desired metrics, but first a quality control was performed during laboratory processing. Traces of soil, roots, flowers, acorns, etc., in the sampling bag was recorded in the field database. This information was later used to remove from the analysis those samples that presented any incidence, ensuring the quality of the data.

Then, all plants collected in the $EWT_{Sample}$ and a sub-sample from each quadrant was scanned using an Epson Perfection V30 color scanner (Epson American Inc., Long Beach, CA, USA). As will be explained in the following lines, in this case the use of a subsample is justified as only leaf area, and dry weight will be retrieved from the subsample. Leaf area was calculated automatically from the scanned images using the unsupervised classification algorithm ISOCLUS with 16 iterations in PCI Geomatica (PCI Geomatics, Richmond Hill, Ontario, Canada). Finally, all samples were dried by placing them in an oven for 48 hours at a constant temperature of 60°C and weighted again.

Three biophysical variables were obtained during this process: Vegetation water content (expressed as Fuel Moisture Content (FMC), Equivalent Water Thickness (EWT) and Canopy Water Content (CWC)), Dry Matter content (Dm), and Leaf Area Index (LAI). FMC was determined from the fresh and dry weights of both the whole quadrant sample ($FMC_Q$) and the $EWT_{Sample}$ ($FMC_{EWT}$) according to **Equation 4:**

$$FMC\ (\%) = \frac{W_{Fresh} - W_{Dryh}}{W_{Dry}} \cdot 100 \qquad \textbf{(Equation 4)}$$

where $W_{Fresh}$ is the fresh weight (in grams) of the sample measured in the field and $W_{Dry}$ is the oven dried weight.

EWT was estimated from the $EWT_{Sample}$:

$$EWT\ (g \cdot cm^{-2}) = \frac{W_{Fresh} - W_{Dry}}{Area_{Leaf}} \qquad \textbf{(Equation 5)}$$

where $Area_{Leaf}$ is the leaf area of the $EWT_{Sample}$ in $cm^2$

Dm was calculated as:

$$Dm\ (g \cdot cm^{-2}) = \frac{W_{Dry}}{Area_{Leaf}} \qquad \textbf{(Equation 6)}$$

CWC was calculated using two different approaches. In the first one, data from the quadrant and $EWT_{Sample}$ were combined using the following expression:

$$CWC_{EWT}\ (g \cdot cm^{-2}) = EWT_{Sample} \cdot LAI \qquad \textbf{(Equation 7)}$$

where LAI is the leaf area index of the grass within the quadrant and EWT is obtained from **Equation 5**. The grass height in the study site was very short due to cow grazing, so the only way to obtain LAI was by using gravitational methods (He et al. 2007). LAI was estimated from the relation between the biomass-leaf area of a sub-sample inside the quadrant relation and the total quadrant's biomass using the following expression:

$$LAI\ (cm^2 \cdot cm^{-2}) = \frac{\frac{W_{Dry}}{W_{Dry}^{Sub}} \cdot Area_{Leaf}^{Sub}}{Area} \qquad \textbf{(Equation 8)}$$

where $W_{Dry}$ is the total dry weight of the whole sample inside the quadrant, $W_{Dry}^{Sub}$ is the dry weight of a sub-sample of $W_{Dry}$, $Area_{Leaf}^{Sub}$ is the sub-sample leaf area and Area is the total area of the quadrant. This gives as result the total LAI, as it accounts for the green vegetation and the dry vegetation that is still rooted to the soil.

Finally the second approach measured CWC from the fresh and dry weight difference of the sample within the quadrant divided by the area of the quadrant ($CWC_Q$ in **Equation 9**):

$$CWC_Q\ (g \cdot cm^{-2}) = \frac{W_{Fresh} - W_{Dry}}{Area} \qquad \textbf{(Equation 9)}$$

## 2.3 Eddy-covariance measurements

A flux can be defined as the amount of an entity that goes through a known surface per unit of time. Airflow generates great number of eddies that can be measured by high sensitive instrumentation used in the so called Eddy Covariance (EC) system (**Figure 10**). The principle of EC is measuring the vertical fluctuations of a scalar ($CO_2$, $H_2O$, heat) at very high frequency over an area for a known period of time. In essence this method uses the covariance between momentum (wind) and the transport of water vapor ($H_2O$), $CO_2$ and heat to represent these fluxes.

The EC technique allows monitoring the gas exchange and energy fluxes at different spatial scales. The use of these micrometeorological measurements offers advantages among traditional methods including continuous and not disturbing measurements (Baldocchi et al. 1988).

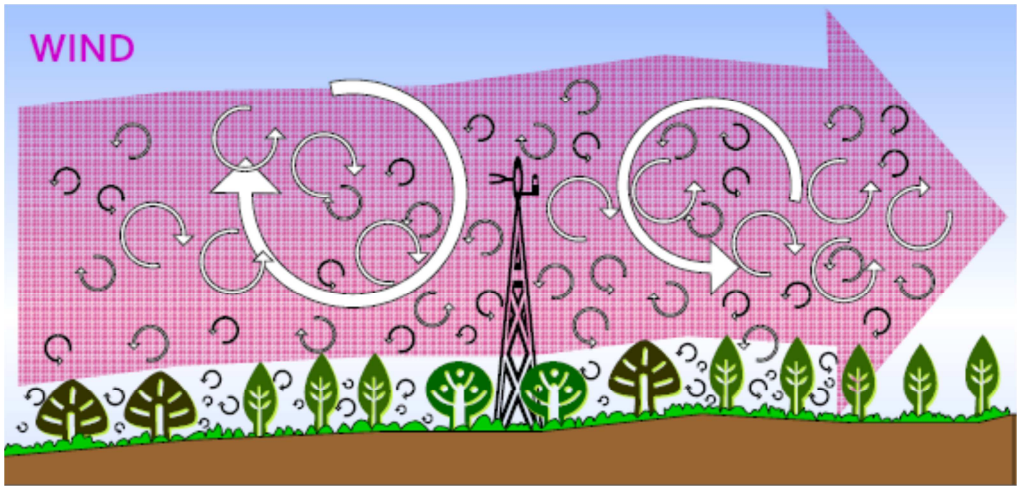


**Figure 10**. Representation of eddies generated by air flow. *Taken from Burba and Anderson (2010).*
*(*http://atoc.colorado.edu/~dcn/ATOC7500b/members/reading/Brief_Intro_Eddy_Covariance.pdf*)*

To make this technique operational, ensuring both the quality and representativeness of the measurements, there are some requirements that need to be addressed which can be a potential source of error. This technique may experience problems due to instrument failure, instrument setup, terrain roughness, etc.

In this study, data from micrometeorological measurements provided by an EC flux tower located at the study site were used. Acquisition and data quality control were carried out by the Centro de Estudios Ambientales del Mediterráneo (CEAM). CEAM provided data for this study following the standards and procedures defined by the national or world-wide flux station networks in which they are included (CARBORED-ES (http://www.ceam.es/carboredes/), CARBOEUROPE-IP (http://www.carboeurope.org/), FLUXNET (http://fluxnet.ornl.gov/). The quality control of EC data includes various steps: basic test using the raw data measured in the field, statistical test and test on the fulfillment of the EC technique requirements (Foken et al. 2005). Gaps in the data due either to sensor or data logger failure were filled using standardized techniques adopted by CarboEurope-IP and FLUXNET networks (Papale et al. 2006), such as the "Marginal Distribution Sampling" method (Reichstein et al. 2005) and the "Artificial Neural Network" method (Papale and Valentini 2003).

The instrumentation of the EC flux tower in our site for the (micro) meteorological measurements is presented in **Table 1.** Data have been collected at this location since May 2003 when the system was set up. Meteorological instruments operating since this date are radiation, air temperature, relative humidity, atmospheric pressure, and wind speed. Sampling frequency for the micrometeorological EC measurements is 10 Hz for the Sonic 3-D anemometer and for the Infra-Red Gas Analyzer.

**Table 1**. Sensors installed at the EC tower in las Majadas de Tiétar study site to measure atmospheric and meteorological variables.

| Variable | | Units | Instrument Type | Instrument model | Start date | Height | Aggregation period |
|---|---|---|---|---|---|---|---|
| **Fc** | **$CO_2$ flux** | $\mu mol.m^{-2}.s^{-1}$ | Sonic 3-D anemometer + IRGA | Sonic R3-50 (Gill) + LI-7500 (LiCor) | 5/15/2003 | 15.5 m | 30 min |
| **LE** | **Latent heat flux** | $W.m^{-2}$ | | | | 15.5 m | 30 min |
| **H** | **Sensible heat flux** | | Sonic 3-D anemometer | Sonic R3-50 (Gill) | | 15.5 m | 30 min |
| **τ** | **Momentum flux** | $Kg.m^{-2}.s^{-1}$ | | | | 15.5 m | 30 min |
| **SWin** | **Short wave incoming radiation** | $W.m^{-2}$ | Pyranometer | CNR4 (Kipp & Zonen) | 4/8/2010 | 15 m | 10 min |
| **SWout** | **Short wave outgoing radiation** | | | | | 15 m | 10 min |
| **LWin** | **Long wave incoming radiation** | | Pyrgeometer | | | 15 m | 10 min |
| **LWout** | **Long wave outgoing radiation** | | | | | 15 m | 10 min |
| **NetRad** | **Net radiation** | | 4 components Net Radiometer | CNR4 (Kipp & Zonen) | 4/8/2010 | 15 m | 10 min |
| **SWin** | **Short wave incoming radiation** | | Pyranometer | CMP22 (Kipp & Zonen) | 2/22/2011 | 15 m | 10 min |

| Variable | | Units | Instrument Type | Instrument model | Start date | Height | Aggregation period |
|---|---|---|---|---|---|---|---|
| **SWdif** | **Diffuse incoming short wave radiation** | W.m$^{-2}$ | Pyranometer | SPN1 (Delta-T) | 2/24/2011 | 15 m | 10 min |
| **WD** | **Wind direction** | Decimal degrees | Sonic 2D anemometer | WindSonic (Gill instruments) | 2/24/2011 | [5m, 9m, 15m] | 10 min |
| **WS** | **Wind speed** | m.s$^{-1}$ | | | | | 10 min |
| **P** | **Precipitation** | mm | Rain Collector | Precipitation Transmiter (Thies Clima) | 5/15/2003 | 1.5 m | 10 min |
| | | | | TRwS 500/503 (MPS systém, spol. s r.o.) | 6/3/2011 | 1.5 m | 10 min |
| **Pa** | **Atmospheric Pressure** | kPa | Barometer | PTB 210 (Vaisala) | 2/24/2011 | 0.8 m | 10 min |
| **RH** | **Relative humidity** | % | Hygrometer | Hygro-thermometer (Thies) in ventilated shelter | 2/24/2011 | [1m, 2m, 4m, 8m, 15m] | 10 min |
| **Ta** | **Air temperature** | °C | Thermometer | | | | 10 min |

With the instrumentation available in the EC flux tower it is possible to obtain a large number of variables of the ecosystem such as the Net Ecosystem Exchange (NEE) and Gross Primary Production (GPP) among others. As this study was oriented to water fluxes estimation between land and atmosphere, we focused in those variables related to Evaporative Fraction (EF) and Evapotranspiration (ET). The EC instruments used for this purpose are the 3-D sonic anemometer and the open path gas analyzer (**Figure 11**).

**Figure 11.** Picture from top of the EC system showing the setup of the sonic anemometer and the open path analyzer. Wiring on top was installed to avoid the birds to place on top of the instruments.

These two instruments work independently; therefore a good synchronization is needed. The 3D sonic anemometer measures the three components of the wind by sending an acoustic signal and measuring the time it takes to travel from two opposite points in three different space dimensions. Elapsed time is due to wind and, therefore, the wind velocity can be retrieved. The sonic anemometer is also capable of measuring temperature (Sonic Temperature) using the same principle, time differences, as does to calculate the wind components. However in this case these differences are due to changes in air density caused by variations in temperature, making the acoustic signal to travel faster or slower. Simultaneously, the gas analyzer measures densities of water vapor and carbon dioxide. Records from both instruments allow estimating the $CO_2$ and $H_2O$ fluxes.

When the estimates using remote sensing are validated using an EC system, it is important to make the evaluation only the in area that is being measured by the EC tower, or footprint. The footprint of the EC tower can be described as the area observed by the EC instrumentation mounted on the tower. Definition of the footprint is important to understand and interpret the fluxes measured with the

instruments as, depending on the area covered by the footprint, different factors can affect the fluxes. The footprint area is always located in the upwind direction (**Figure 12**a) and there are several factors that can modify it:

- The heights at which measurements are taken. If instruments are located near the ground, the footprint will be small and fluxes will be highly affected by the area nearby the EC tower. The opposite occurs when the instruments are located at upper heights. In that case the footprint is larger, but the areas nearby the EC tower present low contributions to the measured fluxes.
- The surface roughness also affects the dimensions of the footprint. When the surface roughness decreases, the size of the footprint increases, and the opposite occurs if the surface roughness increases, since roughness affects turbulence and hence the size of the eddies.
- Thermal stability also modifies the footprint. If thermal conditions are stable, the area is much larger than under unstable conditions, as convection also enhances turbulence and therefore shape of the eddies.

There are many different methods to estimate the EC footprint (Haenel and Grünhage 1999; Horst and Weil 1992; Kljun et al. 2002). In this study the two-dimensional footprint of the EC tower was estimated using the approach of Detto et al. (2006) with the footprint weights in the upwind direction derived using the model of Hsieh et al. (2000) and the weights in the cross wind direction assumed to be normally distributed with standard deviation dependent on the standard deviation of the horizontal crosswind velocity fluctuations (Schmid 1994). This results in a 2D grid (**Figure 12**b) of pixels representing the relative contribution of each pixel to the total EC footprint signal, with the sum of all pixels being 1. When evaluating the high resolution fluxes, each modeled pixel is scaled according to how strong is the contribution of its location to the EC measurement

a)

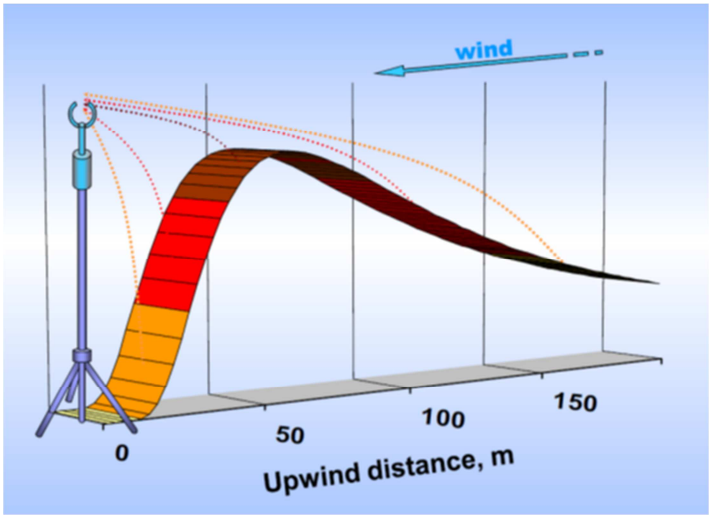


b)

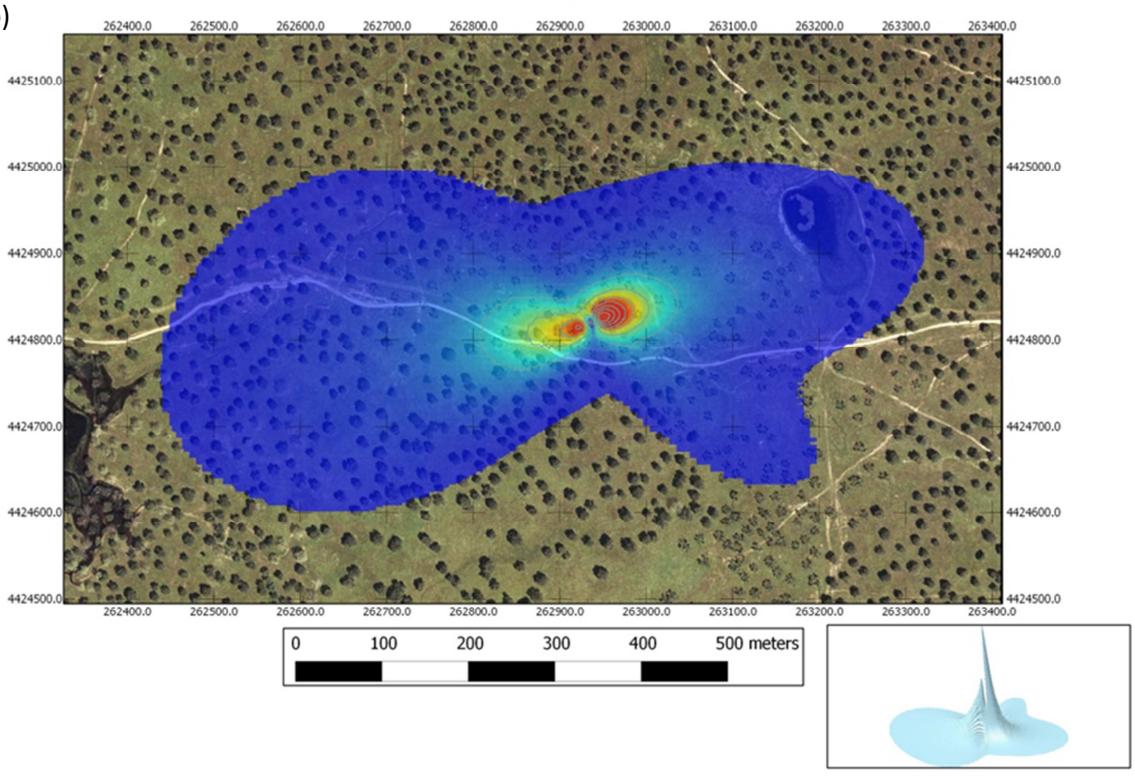


**Figure 12.** a) Visualization of flux contributions to the EC measurements. Taken from Burba and Anderson (2010) (http://atoc.colorado.edu/~dcn/ATOC7500b/members/reading/Brief_Intro_Eddy_Covariance.pdf).b) Cumulative footprint at 12:00 hours for the whole year 2009 in Majadas del Tiétar study site. This latter figure shows how dominant winds in the area have an East-West component.

## 2.4 Soil measurements and soil moisture

Soil measurements were performed at the study site in order to estimate SM, Soil Temperature and Soil Heat Flux (G) using the sensors listed in **Table 2**.

**Table 2.** Sensors installed at Las Majadas del Tiétar study site to measure soil variables.

| Parameter | | Units | Instrument Type | Instrument model | Start date | Height | Aggregation period |
|---|---|---|---|---|---|---|---|
| **SWC** | **Soil water content** | % vol | ThetaProbe (volumetric soil moisture content sensor) | Theta probe ML2X (Delta T) | 4/20/2005 | [-0.04, -1.9] | 10 min |
| **Ts** | **Soil temp.** | °C | Thermocouple | STP01 (Hukseflux) | 2/22/2011 | [-0.02,-0.5] | 10 min |
| | | | | Pt100 (Campbell Scientific) | 2/9/2011 | [-0.02,-0.5] | 10 min |
| **G** | **Soil heat flux** | $W.m^{-2}$ | Heat Flux | PU43 (Hukseflux) | 5/15/2003 | [-0.02] | 10 min |
| | | | | HFP01SC (Hukseflux) | 10/19/2010 | [-0.02,-0.03] | 10 min |

Time Domain Reflectometry (TDR) was used to measure SM. This technique bases its principle on the high dielectric constant ($\varepsilon_r$) of water (80) vs. other materials like soil (6) or air (1). Dielectric materials are those that are not good electricity conductors but that permit displacement of charge.

The TDR device is consisting on two or three metallic parallel rods (conductor) that are introduced into the soil (dielectric medium). The instrument (**Figure 13**a) has a precise receiver that measures time. The TDR unit emits an electromagnetic pulse and the signal is transferred through the rods. The signal is reflected at the end of the rods. The elapsed time since the pulse was emitted and reflected is measured by the receiver unit. This time is related to the propagation velocity of the signal that depends mainly on the amount of water in the soil.

The TDR sensors are installed in the study site at 4 different depths to collect the SM variations (4 cm, 8 cm, 10 cm and 20 cm). Three of these sensors are installed creating a vertical profile and, therefore, not having more than 4 cm displacement on the horizontal plane. The sensors in the vertical profile are located at 10 m from the Eddy Covariance flux tower and the remaining sensors at 8 m distance (**Figure 13**b). SM measurements are continuously recorded every 30 minutes.

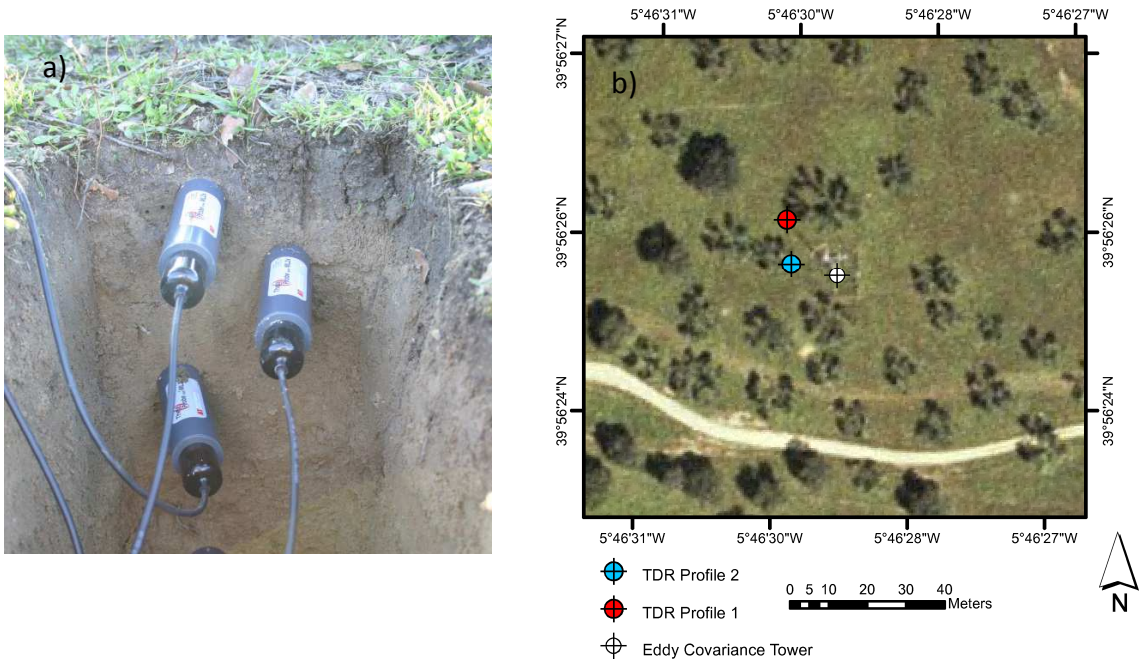


**Figure 13.** a) MLX2 ThetaProbe sensor used in Las Majadas study site. b) Orthophoto showing the location of the TDR sensors used for this study. Red circle points to the TDR sensors at 4cm, 10cm and 20cm. Blue circle points to the TDR sensor at 8 cm.

## 2.5 Spectral information

Different sources of spectral information have been used in this study including both proximal and satellite remote sensing which has allowed a multi-scale analysis of the water fluxes in the proposed site. The following sections include a description of the main characteristics of the spectral datasets used in this work (**Table 3**).

**Table 3.** Brief summary description of spectral data sources used in this study.

| | **ASD Fieldspec3** | **Landsat TM and ETM+** | **TERRA-MODIS** | **MSG-SEVIRI** |
|---|---|---|---|---|
| **Revisit period** | 16 days | 16 days | 2 times a day | 15 minutes |
| **Spatial resolution** | Field scale (25° FOV) | 30 m | 500 m optical | 4 km (Resampled). |
| **Spectral domains** | Optical | Optical/Thermal | Optical/Thermal | Optical/Thermal |
| **Band Wavelengths** | (350 nm - 2500nm @1nm) | B1 (450-520 nm)<br>B2 (520-600 nm))<br>B3(630-690 nm)<br>B4 (760-900 nm)<br>B5 (1550-1750 nm)<br>B6 (10400-12500 nm)<br>B7 (2080-2350 nm) | B1 (620-670 nm)<br>B2 (841-876 nm)<br>B3 (459-479 nm)<br>B4 (545-565 nm)<br>B5 (1230 -1250 nm)<br>B6 (1628-1652 nm)<br>B7 (2105-2155 nm)<br>B31 (10780-11280 nm)<br>B32 11770-12270 nm) | B1 (560-710 nm)<br>B2 (740-880 nm)<br>B3 (1500-1780 nm)<br>B10 ( 11000-13000 nm)<br>B11(12400-14400 nm) |

### 2.5.1 Field spectroscopy

Proximal sensing data were acquired using an ASD FieldSpecTM 3 (http://www.asdi.com/) spectroradiometer (Analytical Spectral Devices Inc, Boulder, Colorado). This instrument samples radiation throughout a fiber bundle cable and distributes it to three different sensors. The first one covers the Visible and the Near InfraRed regions (VNIR), from 350 nm to 1000 nm with a 3 nm of Full Width at Half Maximum (FWHM) and a Spectral Sampling Interval (SSI) of 1.4 nm. The other two sensors cover the SWIR region, splitting it in two ranges, from 1000 nm to 1800 nm (SWIR 1) and from 1800 nm to 2500 nm (SWIR 2). For these sensors, FWHM is 10 nm and SSI is 2 nm. Default configuration provides spectral data interpolated to 1 nm intervals for the full range covered. Spectral measurements were obtained over each 25x25 $m^2$ grassland plot along two transects: NW-SE and NE- SW, based upon the stakes placed during the sampling design (Section 2). Spectra were acquired at approximately 1.2 m height, rendering a sensor footprint diameter of about 53 cm, since nominal FOV is 25° (**Figure 14**). Before measuring each transect, dark current was recorded and removed, and instrument configuration optimized for illumination conditions prior to the measurements in each transect of the plot. A reference spectrum was acquired using a Spectralon® 99% reflective reference panel (Labsphere Inc., North Sutton, NH, USA). All measurements were taken under clear sky conditions within about ±2 hours from local solar noon, to guarantee homogeneous illumination conditions and maximum solar irradiance. Sky conditions were recorded in the field logs, and a quality control checked the spectra to remove those where illumination changes may have occurred after calibration. The ASD was handled without fore optics (http://www.asdi.com/products/accessories/remote-sensing-accessories/foreoptics) to reduce the directional effects on the spectroradiometer's fibers bundle field of view (FOV) (MacArthur et al. 2012).

**Figure 14.** Picture showing proximal sensing data acquisition using an ASD FieldSpec 3 spectroradiometer. One operator is controlling the spectroradiometer and a second operator assists with the white reference panel and writing down any incidences.

With the help of the field notes, spectra were processed and those having any anomaly such as changes in illumination or any instrumental problem where removed to ensure consistence and quality of the temporal series.

### 2.5.2 Landsat

Landsat 5 TM and Landsat 7 ETM+ images available between April 1st 2009 and 31st December 2011 were downloaded from the Land Processes Distributed Active Archive Center (LP DAAC), located at USGS/EROS, Sioux Falls, South Dakota (http://lpdaac.usgs.gov). Images during the study period were atmospherically corrected and converted to surface reflectance using the Landsat Ecosystem and Disturbance Adaptative Processing System (LEDAPS, http://ledapsweb.nascom.nasa.gov/). This model uses the routines developed for Terra MODIS for atmospheric corrections (Vermote et al. 1997). LEDAPS image correction process is summarized in **Figure 15.**

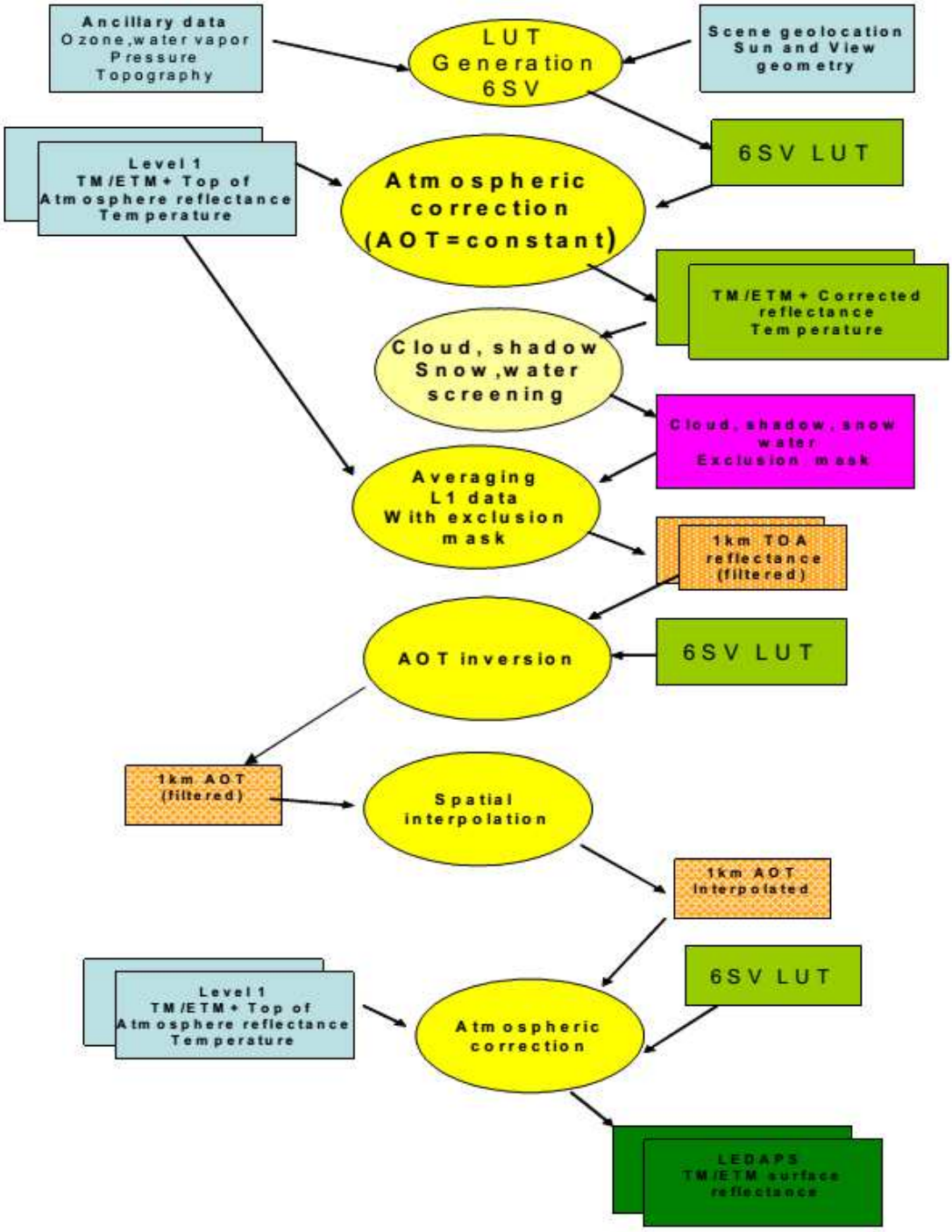


**Figure 15.** LEDAPS algorithm description (Source: LEDAPS surface reflectance description. Version 2.0).

LEDAPS creates a Look-Up Table (LUT) for the whole scene and for each band with information on atmospheric pressure, ozone, geometric distortions and

total column water vapor (W) using the Second Simulation of a Satellite Signal in the Solar Spectrum, Vector, Version 1, (6S V) RTM code (Kotchenova et al. 2006). LEDAPS uses then the Dark Dense Vegetation (DDV) algorithm (Kaufman et al. 1997) to account for the Aerosol Optical Thickness (AOT) directly from the image and LUT. In a first step the image is resampled to 1 km resolution and "dark targets" are selected. AOT is calculated for the blue channel based on the correlation between the blue (0.45–0.52 mm) and SWIR channel (2.2mm) bands. The AOTs for the remaining channels are propagated across the spectrum using a continental aerosol model at 30 m. Quality tests are carried out to find unrealistic values and neglecting those cases were too many are present within the 1 km window. . Then, the AOT is spatially interpolated over the selected dark targets in the scene and together with the ozone, atmospheric pressure, and W, the atmospheric transmittance and spherical albedo are calculated with 6S in order to invert the Top Of the Atmosphere (TOA) reflectance to surface reflectance for each 30-m pixel using: .

$$\rho^{TOA} = \rho_{atm} + \frac{T_d T_u \rho^s}{1 - s_{atm}\rho^s} \qquad \textbf{(Equation 10)}$$

where $\rho^{TOA}$ is the TOA reflectance, $\rho_{atm}$ is the atmospheric intrinsic reflectance, $T_d$ is the downward atmospheric transmission in the direction of light propagation form the TOA surface $T_u$ is the upward atmospheric transmission in the direction of light propagation form the surface to the sensors. $\rho^s$ is the surface reflectance, and $s_{atm}$ is the atmospheric spherical albedo.

Landsat surface reflectance estimated with LEDAPS was validated using our field reflectance data (**Figure 16**) showing good agreement and therefore ensuring the reliability of the atmospheric correction. The small differences can be explained due to dissimilarities in the illumination conditions, due to differences between Landsat overpass time and *in situ* sampling differences in the FOV, especially important over heterogeneous surfaces, or even just differences due to the image correction method. Although LEDAPS creates a cloud mask, we applied on top the Function of Mask (FMask) algorithm (Zhu and Woodcock 2012).

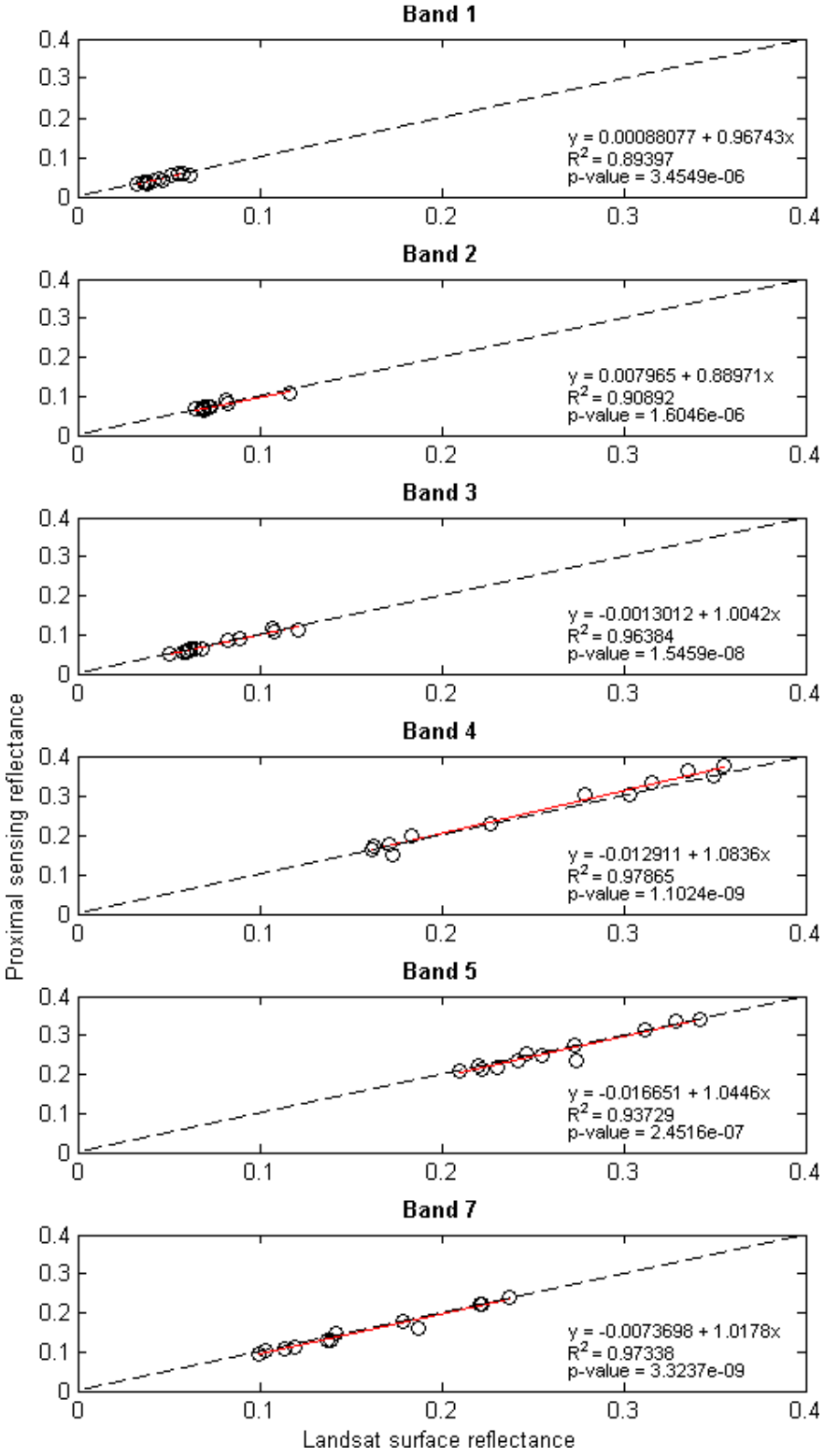


**Figure 16.** Comparison of surface reflectance measured using a field spectroradiometer and Landsat corrected with LEDAPS. Band wavelengths can be found on **Table 3**. Grassland plots without tree canopy was used for this comparison.

### 2.5.3 MODIS

#### 2.5.3.1 Optical Data

MODIS Terra daily surface reflectance (MOD09GA) data from April 1st, 2009 to April 15th, 2011 were downloaded from NASA Land Processes Distributed Active Archive Center (LP DAAC) at the USGS/Earth Resources Observation and Science (EROS) Center, Sioux Falls, South Dakota, USA. This product provide an estimate of the surface spectral reflectance as it would be measured at ground level in the absence of atmospheric scattering or absorption for bands 1 to 7 (469-2130 nm) at 500 m spatial resolution. It provides additional information on sensor and solar angles and quality state at 1 km resolution. A script programmed in Matlab (Mathworks, Batick, Massachusetts, USA) was used to extract, from the image time series, the reflectance values of the MODIS pixel centered in the EC flux tower that includes approximately 80% of the field sampled. The election of a single pixel was preferred to a window of 2 or 3 pixels as there is a cropland area in the north of the study site that could affect the data if an average value had been used. The impact of angular effects on reflectance was reduced by discarding pixels with View Zenith Angles (VZA) wider than 20°. This will also minimize the problems related to the accuracy of the geometrical location of the pixel (Wolfe et al. 2002). Under nadir observations the footprint observed by the sensor presents usually a circular shape, and contributions are usually Gaussian. When viewing geometry changes and the viewing angle is increasing, the footprint is not circular anymore, and contributions are distorted, this translates in uncertainties, especially over heterogeneous areas. Finally, the quality assurance layer was used to eliminate images under clouds, cloud shadows and/or with high atmospheric aerosol content (**Table 4**). We prefer using this product instead of MYD09GA due to the system failure on band 6 on 15 of the 20 detectors in MODIS- Aqua (Wang et al. 2006a).

**Table 4.** Table showing some of the binary codes during this study and their meaning when translated to decimal numbers. Bold numbers indicate those with the highest quality of data.

| Binary Code | Internal snow mask | BRDF performed | Pixel is adjacent to cloud | MOD35 Snow/Ice flag | Internal fire algorithm | Internal cloud algorithm | Cirrus | Aerosols | Land/Water | Cloud Shadow | Cloud State |
|---|---|---|---|---|---|---|---|---|---|---|---|
| **72** | 0 | 0 | 0 | 0 | 0 | 0 | 00 | 00 | 001 | 0 | 00 |
| 74 | 0 | 0 | 0 | 0 | 0 | 0 | 00 | 01 | 001 | 0 | 10 |
| 76 | 0 | 0 | 0 | 0 | 0 | 0 | 00 | 01 | 001 | 1 | 00 |
| 137 | 0 | 0 | 0 | 0 | 0 | 0 | 00 | 01 | 001 | 0 | 01 |
| **136** | 0 | 0 | 0 | 0 | 0 | 0 | 00 | 10 | 001 | 0 | 00 |
| 138 | 0 | 0 | 0 | 0 | 0 | 0 | 00 | 10 | 001 | 0 | 10 |
| 140 | 0 | 0 | 0 | 0 | 0 | 0 | 00 | 10 | 001 | 1 | 00 |
| 142 | 0 | 0 | 0 | 0 | 0 | 0 | 00 | 10 | 001 | 1 | 10 |
| **200** | 0 | 0 | 0 | 0 | **0** | 0 | 00 | 10 | 001 | 0 | 00 |
| 201 | 0 | 0 | 0 | 0 | 0 | 0 | 00 | 11 | 001 | 0 | 01 |
| 206 | 0 | 0 | 0 | 0 | 0 | 0 | 00 | 11 | 001 | 1 | 10 |
| 204 | 0 | 0 | 0 | 0 | 0 | 0 | 00 | 11 | 001 | 1 | 00 |
| 1032 | 0 | 0 | 0 | 0 | 0 | 1 | 00 | 11 | 001 | 0 | 00 |
| 1033 | 0 | 0 | 0 | 0 | 0 | 1 | 00 | 00 | 001 | 0 | 01 |
| 1034 | 0 | 0 | 0 | 0 | 0 | 1 | 00 | 00 | 001 | 0 | 10 |
| 1289 | 0 | 0 | 0 | 0 | 0 | 1 | 01 | 00 | 001 | 0 | 01 |
| 1288 | 0 | 0 | 0 | 0 | 0 | 1 | 01 | 00 | 001 | 0 | 00 |
| 1290 | 0 | 0 | 0 | 0 | 0 | 1 | 01 | 00 | 001 | 0 | 10 |
| 1544 | 0 | 0 | 0 | 0 | 0 | 1 | 10 | 00 | 001 | 0 | 00 |
| 1545 | 0 | 0 | 0 | 0 | 0 | 1 | 10 | 00 | 001 | 0 | 01 |
| 1800 | 0 | 0 | 0 | 0 | 0 | 1 | 11 | 00 | 001 | 0 | 00 |
| 1801 | 0 | 0 | 0 | 0 | 0 | 1 | 11 | 00 | 001 | 0 | 01 |
| 1802 | 0 | 0 | 0 | 0 | 0 | 1 | 11 | 00 | 001 | 0 | 10 |
| 5129 | 0 | 0 | 0 | 1 | 0 | 0 | 00 | 00 | 001 | 0 | 01 |
| **8200** | 0 | 0 | 1 | 0 | 0 | 0 | 00 | 00 | 001 | 0 | 00 |
| 8204 | 0 | 0 | 1 | 0 | 0 | 0 | 00 | 00 | 001 | 1 | 00 |
| 8205 | 0 | 0 | 1 | 0 | 0 | 0 | 00 | 00 | 001 | 1 | 01 |
| 8206 | 0 | 0 | 1 | 0 | 0 | 0 | 00 | 00 | 001 | 1 | 10 |
| 65535 | 1 | 1 | 1 | 1 | 1 | 1 | 11 | 00 | 001 | 1 | 11 |

#### 2.5.3.2 Thermal Data

Daytime and nighttime Ts were obtained from Terra and Aqua daily products: MOD11A1 (https://lpdaac.usgs.gov/products/modis_products_table/mod11a1) and MYD11A1 (https://lpdaac.usgs.gov/products/modis_products_table/myd11a1), respectively. The MOD11A1 product provides per pixel Ts and emissivity for the Terra sensor (acquired at 22:30 and 10:30 local solar time over the equator), while the MYD11A1 provides the same information for the Aqua sensor (acquired at 1:30 and 13:30 local solar time over the equator). These three products contain additional layers with information such as VZA, quality flags assurance or time of the overpass (https://lpdaac.usgs.gov/products/modis_products_table).

#### 2.5.3.3 LAI data

The MODIS MCD15A3 combined (Terra and Aqua) MODIS global LAI and FPAR product is composited every 4 days at 1-kilometer resolution and includes flags with information on the quality of the LAI retrieval (https://lpdaac.usgs.gov/products/modis_products_table/mcd15a3). This product was downloaded from NASA Land Processes Distributed Active Archive Center (LP DAAC) at the USGS/Earth Resources Observation and Science (EROS) Center, Sioux Falls, South Dakota, USA for the dates corresponding to the Landsat images acquisition. The information contained in this product corresponds to four days starting from the date used in the filename.

### 2.5.4 SEVIRI

Data from the Spinning Enhanced Visible and InfraRed Imager (SEVIRI), onboard the geostationary EO platform Meteosat Second Generation (MSG), were obtained from the Department of Geoscience and Natural Resources Management at the University of Copenhagen, Denmark. SEVIRI has 12 spectral bands ranging from the optical to the thermal regions. MSG-SEVIRI permits observing the same surface

at multiple times (every 15 minutes) during the day, which allows for quantifying the morning temperature rise (Stisen et al. 2008b). In this study only 5 SEVIRI bands have been used: three in the optical region (nominal centers at 0.6, 0.8 and 1.6 μm) and 2 in the thermal infrared (nominal centers at 11.2 and 12.0 μm). SEVIRI observes the Earth at a constant viewing angle with a spatial sampling of 3.1km at nadir. In the case of our study area, VZA is close to 46 degrees and, therefore, we resampled the data to a pixel size resolution of 4 km (**Figure 17**).

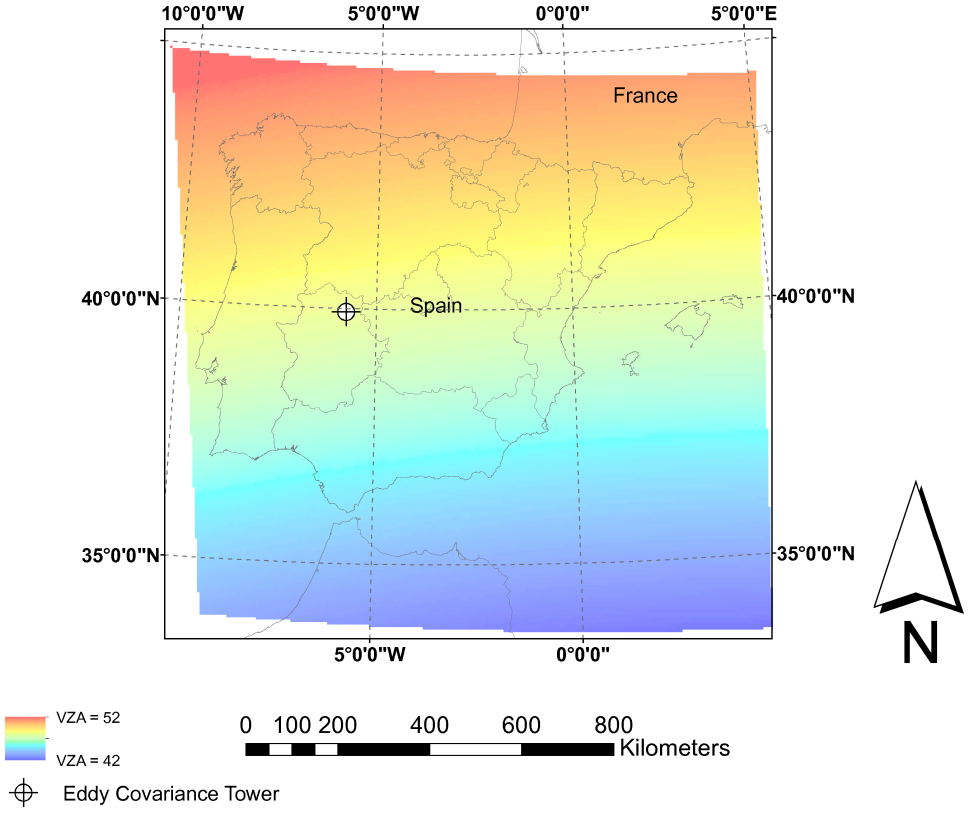


**Figure 17.** VZA from SEVIRI over the Iberian Peninsula.

Four-day Normalized Bidirectionally Adjusted Reflectance (NBAR) was produced for the optical data (Proud et al. 2014). First, the 15-minute directional reflectances were atmospherically corrected using a modified version of the Simplified Method for Atmospheric Correction (SMAC) code (Proud et al. 2010; Rahman and Dedieu 1994). As the atmospheric correction requires information about aerosol optical depth, W, and ozone content, this information is fed into SMAC from the relevant MODIS atmosphere products on a daily basis

(MOD08_D3/MYD08_D3). Then, a semi-empirical Bidirectional Reflectance Distribution Function (BRDF) model, inherited from the MODIS BRDF model (Schaaf et al. 2002) was fitted using all daytime observations in a 4-days period. Modeled BRDF reflectances at local solar noon and observed at nadir were calculated as the NBAR.

Land surface temperature (Ts) was estimated using the two-channel split-window algorithm proposed by Sobrino and Romaguera (2004). The algorithm requires as ancillary data VZA, W, and the emissivity (ε) for both split-window channels. Daytime W was retrieved from the images by using the time-difference split-window algorithm described in Sobrino and Romaguera (2007), while $\varepsilon$ was obtained following the Vegetation Cover Method (VCM) described in Trigo et al. (2008) by using the NBAR NDVI as proxy of the fractional vegetation cover. Using the International Geosphere-Biosphere Program (IGBP) Land Cover map (Loveland and Belward 1997) it gives a calibrated emissivity value for vegetation and soil for each band. Emissivity for each pixel is calculated using **Equation 11**:

$$\varepsilon_{eff} = \varepsilon_{veg} FVC + \varepsilon_{bg}(1 - FVC) \qquad \textbf{(Equation 11)}$$

where FVC is the fraction of vegetation cover, and $\varepsilon_{veg}$ and $\varepsilon_{bg}$ are the vegetation and bare ground emissivities for each channel. FVC was calculated and empirical next relationship with NDVI

$$FCV = \frac{NDVI - NDVI_{soil}}{NDVI_{veg} - NDVI_{soil}} \qquad \textbf{(Equation 12)}$$

where NDVI is the actual NDVI value of theh pixel, $NDVI_{soil}$ is the NDVI minimum NDVI value, and $NDVI_{veg}$ is the NDVI at full canopy cover. In this study the values were empirically defined and $NDVI_{soil}$ was set to 0.18 and $NDVI_{veg}$ was set to 0.70.

### 2.5.5 Spectral indices

In this research different spectral indices have been calculated using the different spectral datasets previously described. In **Table 5** these indices are enumerated using MODIS band numbers as reference in the formulation.

**Table 5.** Spectral indices calculated during the study. MODIS band numbers are used as reference.

| Index | Formula | Reference |
|---|---|---|
| Normalized difference vegetation index (NDVI) | $NDVI = \frac{B_2 - B_1}{B_2 + B_1}$ | (Rouse et al. 1973) |
| Enhanced Vegetation Index (EVI) | $EVI = 2.5 \cdot \left( \frac{B_2 - B_1}{B_2 + 6 \cdot B_1 - 7.5 \cdot B_3} \right)$ | (Huete et al. 2002) |
| Normalized Difference Water Index (NDWI) | $NDWI = \frac{B_2 - B_5}{B_2 + B_5}$ | (Gao 1996) |
| Normalized Difference Infrared Index (NDII) | $NDII = \frac{B_2 - B_6}{B_2 + B_6}$ | (Hardisky et al. 1983) |
| Simple Ratio Water Index (SRWI) | $SRWI = \frac{B_2}{B_5}$ | (Zarco-Tejada et al. 2003) |
| Soil Adjusted Vegetation Index (SAVI) | $SAVI = \left( \frac{B_2 - B_1}{B_2 + B_1 + L} \right) \cdot (1 + L)$ Where L= 0.5 | (Huete 1988) |
| Global Environment Monitoring Index (GEMI) | $GEMI = \eta \cdot (1 - 0.25\eta) - \frac{B_1 - 0.125}{1 - B_1}$ where $\eta = \frac{2 \cdot (B_2^2 - B_1^2) + 1.5 \cdot B_2 + 0.5 \cdot B_2}{B_2 + B_1 + 0.5}$ | (Pinty and Verstraete 1992) |
| Visible Atmospherically Resistant Index (VARI) | $VARI = \frac{B_4 - B_1}{B_4 + B_1 - B_3}$. | (Gitelson et al. 2002a) |
| Global Vegetation Monitoring Index (GVMI) | $GVMI = \frac{(NIR_{REC} + 0.1) - (SWIR_{REC} - 0.02)}{(NIR_{REC} + 0.1) + (SWIR_{REC} - 0.02)}$ | (Ceccato et al. 2002) |

# 3 Vegetation Water Content

## 3.1 Methodology

In this part of the study the VI spectral data (**Table 5**) and the field variables (Section 2.2 and **Figure 5**) corresponding to the plots within the MODIS pixel containing the EC tower have been used (**Figure 18**). We selected the closest valid MODIS image to the field sampling day within ± 5 day window, or the MODIS image acquired before the sampling day in case there were two images separated equally in time. Minimum time lag between field and satellite data is desirable in order to reduce the chances of discrepancy due to animal grazing, which could cause LAI changes in short time periods or rain events.

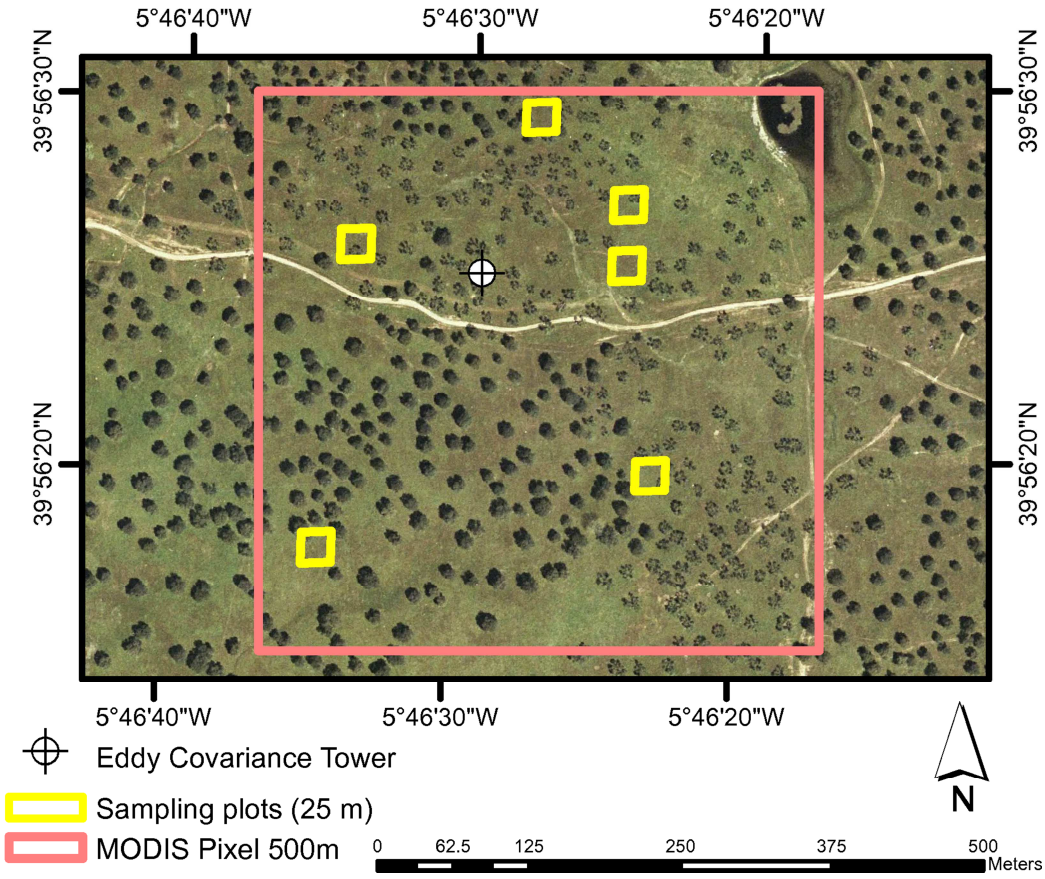


**Figure 18.** Sample plots used in the study and corresponding pixel to the EC tower location.

Based on this information the intra-group, inter-group and overall $R^2$ values between $FMC_Q$, $FMC_{EWT}$, EWT, $CWC_Q$, $CWC_{EWT}$ or LAI, and each of the proximal sensing spectral indexes were calculated to investigate their spatio-temporal variability within the 500 m MODIS pixel. More specifically, the intra-group $R^2$ offers information about the spatial variability, due to the collection of samples at different plots within the MODIS pixel. A linear regression model was created for each sampling day where the biophysical variable and the spectral index were the dependent and the independent variable, respectively. The average $R^2$ of all the regression models for each day provided the intra-group $R^2$. Instead, the inter-group $R^2$ explains the temporal variability due to the collection of the samples on different days. In this case, the biophysical variable and the VI for all plots were averaged for each day. The temporal linear regression model of these averaged values determined the inter-group $R^2$. To explain temporal and spatial variability altogether, the overall $R^2$ fitted in a single regression model including all plots and sampling days for each VI and biophysical variable was obtained.

Later, using the mean values of each biophysical variable and the proximal sensing VI derived from ASD field spectral measurements an univariate linear regression model was applied. The same procedure was repeated for VIs derived from MODIS data. Bootstrapping techniques evaluated the empirical model robustness. According to Richter et al. (2012) this is a valid alternative to traditional leave-one-out methods to validate regression models predictability. 200 bootstrap model simulations were run for each model and the median value of each statistics represented its performance. Root Mean Square Error (RMSE), Relative Root Mean Square Error (RRMSE), Nash-Sutcliffe Efficiency index (NSE), coefficient of determination ($R^2$) and Taylor's diagrams evaluated the models' performance. As recommended in Steyerberg et al. (2001), 200 bootstrap model simulations were run for each model and the median value of each statistics represented its performance. The RMSE measured the error in the estimation of the biophysical variable by each model:

$$RMSE = \sqrt{\frac{1}{n}\sum_{i=1}^{n}(V_{est}^{i} - V_{obs}^{i})^2} \qquad \textbf{(Equation 13)}$$

where $V_{est}^{i}$ is the estimated variable and $V_{obs}^{i}$ is its observed field measurement. RMSE cannot compare the error of different variables with different units. RRMSE addresses this limitation to by dividing the RMSE by the average of the observed values ($\bar{V}_{obs}$) (Richter et al. 2012):

$$RRMSE = 100\frac{RMSE}{\bar{V}_{obs}} \qquad \textbf{(Equation 14)}$$

The NSE indicates the model predictive power which ranges from –∞ to the best predictive power value of 1 (Richter et al. 2012). It establishes if the model performs at least as accurate as the average of observed values through the following expression:

$$NSE = 1 - \frac{\sum_{i=1}^{n}(V_{est}^{i} - V_{obs}^{i})^2}{\sum_{i=1}^{n}(V_{obs}^{i} - \bar{V}_{obs}^{i})^2} \qquad \textbf{(Equation 15)}$$

The determination coefficient ($R^2$) measures the proportion of variance explained by the model and is calculated as:

$$R^2 = 1 - \frac{\sigma_r^2}{\sigma^2} \qquad \textbf{(Equation 16)}$$

where $\sigma_r^2$ represents the residual variance of the model and $\sigma^2$ is the variance of the dependant variable.

The final analysis aimed to compare the performance of the resulting empirical models developed with the RTM-based models for estimating CWC (Trombetti et al. 2008) and FMC (Jurdao et al. 2013). For that Taylor diagrams will be used as they represent a graphical summary of the performance of the models and are used to compare complex models such as those RTM based mentioned before. In these plots the observed variable and its standard deviation (SD) are plotted in the x-axis. RMSE is represented as semicircles centered at the observed data. The correlation coefficient (r) is displayed in the azimuthal position. Best models are closer in the plot to the observed measurement point; therefore they

will have a high r, a low RMSE and a SD similar to the observed values (Taylor 2001).

## 3.2 Results

First, we show temporal trends of all variables involved in this study (**Figure 19**) as a daily average of all sampling plots. All variables except Dm showed similar temporal evolution with a mean peak in spring and secondary peak in the fall. Dm fluctuated throughout the year and exhibited its highest values in the summer. $FMC_{EWT}$ and $CWC_{EWT}$, both calculated from the $EWT_{Sample}$, presented similar trends but in some cases higher values than $FMC_Q$ and $CWC_Q$, calculated from the quadrant sample. The 47% Coefficient of Variation (CV) for Dm was less than for $CWC_Q$ (CV= 95%), $CWC_{EWT}$ (CV=95%), $FMC_Q$ (CV= 60%) and $FMC_{EWT}$ (CV= 56%), but higher than for EWT (CV= 38%). Differences in LAI and CWC values between for years 2009 and 2010 as a consequence of different precipitation can also be noticed, especially during the spring periods with much higher values in 2010.

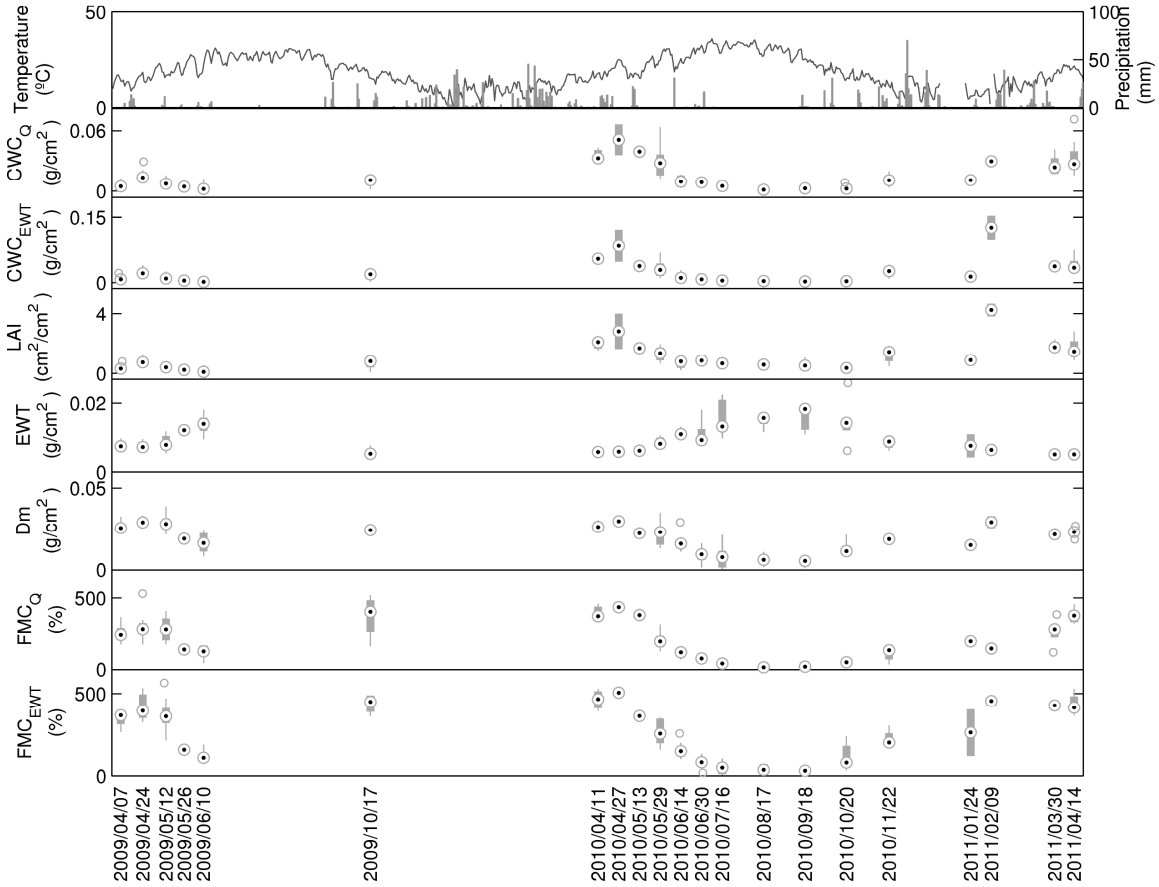


**Figure 19**. Box plot showing the temporal evolution of field biophysical variables measured. Points represent the median of the daily measurements, the boxes indicate the position of the 1st and 3rd quartile, lines delimit the maximum and minimum values, and empty points are outliers. Precipitation is represented using bars and temperature is represented with a solid line.

The spatio-temporal analysis showing the intra-group, intergroup and overall $R^2$ are now presented (**Figure 20**). In this section the obtained results indicated a low intra-group $R^2$ for all the variables suggesting a low spatial variability between plots. On the contrary, the high inter-group $R^2$ also for all variables points to the high temporal variability between sampling dates. The main differences between variables occurred for overall $R^2$. Similar overall and inter-group $R^2$ values for $CWC_{EWT}$ and $FMC_{EWT}$ indicated that the combination of the temporal and spatial factors matched in importance. Instead, overall $R^2$ for $CWC_Q$ and $FMC_Q$ laid in between the inter-group and the intra-group $R^2$ underling the

temporal factor as the main source of variation. VARI had the weakest determination coefficient for all variables while GEMI offers the best $R^2$ of all of them. Those VI that included information in the SWIR region presented better performance those that do not include it in the case of LAI and CWC. In the case of FMC and EWT, VIs more related to chlorophyll content gave better results.

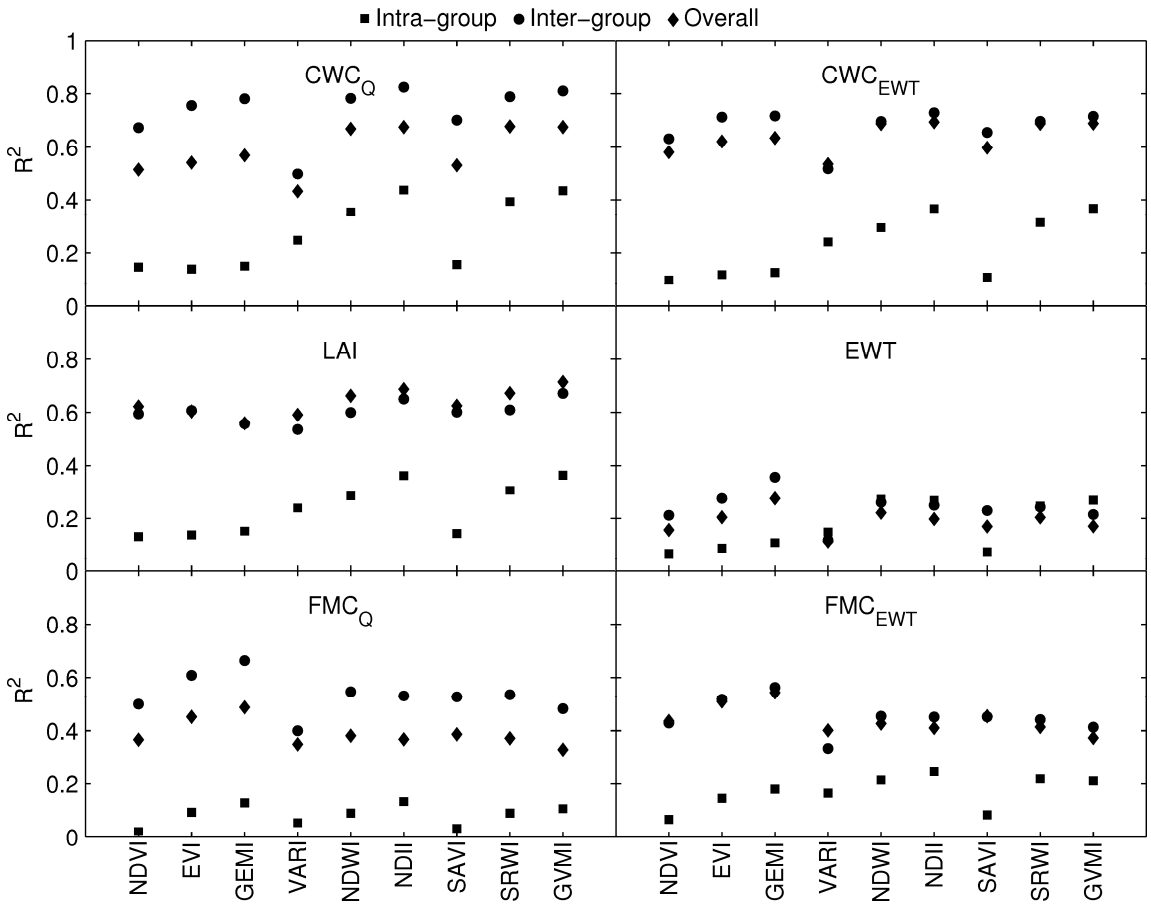


**Figure 20. .** Intra-group (Squares), inter-group (Circles) and overall (Diamonds) $R^2$ values between proximal sensing spectral indexes and biophysical variables measured in the field.

The best univariate empirical boostrap model to predict each of the different biophysical variables using VIs for proximal sensing are shown in **Table 6** for proximal sensing and **Table 7** for MODIS. The model with better statistics to retrieve each variable differed for both data sources. $FMC_{EWT}$ and $FMC_{Q}$ showed the best correlations with GEMI for the proximal data but EVI performed best for MODIS. EWT was best estimated with GEMI in both sensors but presented the lowest $R^2$ and NSE of all the biophysical variables. NDII and GVMI were the best predictors for LAI, $CWC_{EWT}$ and $CWC_{Q}$ with proximal sensing. When using MODIS instead, the best results for LAI were achieved with NDII and GVMI, but EVI did so for $CWC_{EWT}$ and $CWC_{Q}$. When the quadrant sample was used instead of the $EWT_{Sample}$, both FMC and CWC showed better results with lower RRMSE and higher NSE and $R^2$.

**Table 6.** Model performance statistics for all the spectral indices calculated using proximal sensing.

| | | NDVI | EVI | SAVI | GVMI | GEMI | VARI | NDWI | NDII | SRWI |
|---|---|---|---|---|---|---|---|---|---|---|
| **$FMC_{EWT}$** | m | 647.630 | 945.300 | 704.460 | 689.010 | **1184.400** | 686.960 | 1605.930 | 588.980 | 1008.910 |
| | b | -40.257 | -5.692 | -39.240 | 229.320 | **-734.405** | 287.300 | 484.815 | 314.340 | -506.827 |
| | RMSE | 121.640 | 110.910 | 117.450 | 126.640 | **103.827** | 127.510 | 114.009 | 115.540 | 119.168 |
| | RRMSE | 45.305 | 42.442 | 46.730 | 48.252 | **41.047** | 49.091 | 46.963 | 47.363 | 47.125 |
| | NSE | 0.334 | 0.497 | 0.416 | 0.340 | **0.492** | 0.338 | 0.377 | 0.355 | 0.387 |
| | $R^2$ | 0.363 | 0.446 | 0.370 | 0.356 | **0.489** | 0.306 | 0.346 | 0.340 | 0.370 |
| **$FMC_Q$** | m | 543.570 | 794.620 | 591.640 | 578.280 | **999.707** | 579.940 | 1373.980 | 496.630 | 865.516 |
| | b | -39.635 | -10.952 | -38.932 | 186.630 | **-626.932** | 235.460 | 404.829 | 258.230 | -445.343 |
| | RMSE | 84.529 | 75.381 | 84.802 | 87.923 | **68.768** | 90.175 | 81.610 | 83.286 | 83.098 |
| | RRMSE | 40.868 | 35.105 | 41.484 | 41.786 | **34.577** | 45.191 | 38.926 | 39.878 | 40.617 |
| | NSE | 0.452 | 0.576 | 0.466 | 0.391 | **0.631** | 0.346 | 0.497 | 0.497 | 0.508 |
| | $R^2$ | 0.448 | 0.537 | 0.461 | 0.439 | **0.602** | 0.377 | 0.513 | 0.415 | 0.515 |
| **EWT** | m | 0.018 | 0.029 | 0.021 | 0.021 | **0.040** | 0.018 | 0.051 | 0.019 | 0.032 |
| | b | 0.011 | 0.011 | 0.011 | 0.019 | **-0.014** | 0.020 | 0.027 | 0.021 | -0.005 |
| | RMSE | 0.006 | 0.006 | 0.006 | 0.006 | **0.005** | 0.006 | 0.006 | 0.006 | 0.006 |
| | RRMSE | 30.745 | 29.115 | 29.972 | 30.063 | **27.438** | 31.521 | 28.927 | 28.916 | 29.537 |
| | NSE | 0.109 | 0.215 | 0.135 | 0.141 | **0.317** | 0.055 | 0.200 | 0.167 | 0.196 |
| | $R^2$ | 0.115 | 0.238 | 0.162 | 0.128 | **0.282** | 0.078 | 0.190 | 0.154 | 0.191 |
| **LAI** | m | 2.855 | 3.726 | 3.030 | 3.274 | 4.340 | 3.032 | 6.840 | **2.621** | 4.358 |
| | b | -0.298 | -0.024 | -0.262 | 0.883 | -2.622 | 1.147 | 1.983 | **1.268** | -2.287 |
| | RMSE | 0.343 | 0.333 | 0.346 | 0.298 | 0.368 | 0.377 | 0.345 | **0.330** | 0.350 |
| | RRMSE | 34.996 | 33.806 | 35.363 | 31.742 | 36.396 | 37.536 | 34.123 | **31.378** | 32.878 |
| | NSE | 0.577 | 0.577 | 0.607 | 0.664 | 0.512 | 0.525 | 0.599 | **0.646** | 0.609 |
| | $R^2$ | 0.546 | 0.584 | 0.573 | 0.675 | 0.528 | 0.515 | 0.602 | **0.667** | 0.623 |
| **$CWC_{EWT}$** | m | 0.079 | 0.110 | 0.085 | 0.092 | 0.134 | 0.082 | 0.200 | **0.075** | 0.127 |
| | b | -0.015 | -0.009 | -0.014 | 0.018 | -0.090 | 0.025 | 0.050 | **0.029** | -0.075 |
| | RMSE | 0.010 | 0.009 | 0.009 | 0.008 | 0.009 | 0.011 | 0.009 | **0.009** | 0.009 |
| | RRMSE | 46.792 | 36.708 | 44.527 | 38.839 | 38.440 | 49.963 | 40.356 | **38.399** | 39.937 |
| | NSE | 0.567 | 0.698 | 0.596 | 0.677 | 0.679 | 0.471 | 0.650 | **0.686** | 0.658 |
| | $R^2$ | 0.564 | 0.675 | 0.626 | 0.664 | 0.679 | 0.441 | 0.679 | **0.704** | 0.662 |
| **$CWC_Q$** | m | 0.064 | 0.088 | 0.069 | 0.077 | 0.109 | 0.063 | 0.167 | **0.063** | **0.106** |
| | b | -0.013 | -0.008 | -0.012 | 0.014 | -0.075 | 0.020 | 0.041 | **0.023** | **-0.063** |
| | RMSE | 0.007 | 0.006 | 0.007 | 0.005 | 0.006 | 0.009 | 0.006 | **0.005** | **0.006** |
| | RRMSE | 41.944 | 35.841 | 39.743 | 31.580 | 32.304 | 52.680 | 33.303 | **30.272** | **34.636** |
| | NSE | 0.610 | 0.729 | 0.662 | 0.794 | 0.769 | 0.401 | 0.776 | **0.797** | **0.764** |
| . | $R^2$ | 0.647 | 0.753 | 0.670 | 0.783 | 0.747 | 0.433 | 0.776 | **0.797** | **0.800** |

**Table 7.** Model performance statistics for all the spectral indices calculated using MODIS data.

| | | NDVI | EVI | SAVI | GVMI | GEMI | VARI | NDWI | NDII | SRWI |
|---|---|---|---|---|---|---|---|---|---|---|
| **$FMC_{EWT}$** | m | 858.207 | **1727.3** | 1070.83 | 754.058 | 1680.08 | 1024.95 | 2171.22 | 754.537 | 1338.8 |
| | b | -168.470 | **-216.43** | -221.470 | 188.781 | -1141.2 | 293.642 | 541.210 | 294.429 | -776.4 |
| | RMSE | 123.871 | **97.006** | 114.228 | 126.706 | 103.121 | 121.428 | 115.411 | 117.777 | 115.30 |
| | RRMSE | 50.720 | **38.363** | 45.988 | 50.895 | 42.053 | 47.068 | 44.279 | 46.849 | 46.360 |
| | NSE | 0.330 | **0.594** | 0.391 | 0.285 | 0.503 | 0.310 | 0.396 | 0.366 | 0.403 |
| | $R^2$ | 0.300 | **0.638** | 0.410 | 0.266 | 0.484 | 0.379 | 0.378 | 0.377 | 0.409 |
| **$FMC_Q$** | m | 680.604 | **1398.385** | 856.278 | 596.816 | 1392.841 | 800.227 | 1768.936 | 607.301 | 1086.85 |
| | b | -127.720 | **-173.518** | -172.878 | 155.702 | -949.314 | 238.266 | 441.327 | 239.867 | -629.16 |
| | RMSE | 96.390 | **67.325** | 86.849 | 97.229 | 69.457 | 94.083 | 85.320 | 86.381 | 86.950 |
| | RRMSE | 46.088 | **33.811** | 40.820 | 46.824 | 34.713 | 44.918 | 40.759 | 42.163 | 41.466 |
| | NSE | 0.358 | **0.660** | 0.460 | 0.298 | 0.620 | 0.376 | 0.457 | 0.440 | 0.455 |
| | $R^2$ | 0.322 | **0.664** | 0.437 | 0.289 | 0.599 | 0.382 | 0.436 | 0.433 | 0.467 |
| **EWT** | m | 0.023 | **0.059** | 0.031 | 0.021 | 0.065 | 0.026 | 0.077 | 0.024 | 0.048 |
| | b | 0.008 | **0.003** | 0.006 | 0.018 | -0.035 | 0.020 | 0.030 | 0.021 | -0.017 |
| | RMSE | 0.006 | **0.005** | 0.006 | 0.006 | 0.005 | 0.006 | 0.005 | 0.006 | 0.005 |
| | RRMSE | 31.106 | **26.333** | 30.446 | 31.416 | 24.600 | 30.773 | 27.547 | 29.525 | 27.907 |
| | NSE | 0.082 | **0.363** | 0.158 | 0.100 | 0.438 | 0.116 | 0.259 | 0.197 | 0.280 |
| | $R^2$ | 0.085 | **0.351** | 0.146 | 0.082 | 0.405 | 0.093 | 0.328 | 0.214 | 0.255 |
| **LAI** | m | 4.199 | 6.267 | 4.851 | **3.941** | 4.933 | 4.700 | 8.898 | 3.524 | 5.564 |
| | b | -1.067 | -0.708 | -1.154 | **0.659** | -3.098 | 1.181 | 2.176 | 1.189 | -3.283 |
| | RMSE | 0.323 | 0.320 | 0.305 | **0.299** | 0.421 | 0.328 | 0.355 | 0.289 | 0.350 |
| | RRMSE | 30.779 | 32.281 | 28.994 | **27.355** | 44.192 | 33.664 | 34.935 | 28.732 | 35.111 |
| | NSE | 0.665 | 0.615 | 0.695 | **0.687** | 0.336 | 0.629 | 0.572 | 0.739 | 0.579 |
| | $R^2$ | 0.658 | 0.649 | 0.706 | **0.737** | 0.351 | 0.635 | 0.568 | 0.743 | 0.584 |
| **$CWC_{EWT}$** | m | 0.112 | **0.195** | 0.134 | 0.105 | 0.174 | 0.124 | 0.272 | 0.099 | 0.170 |
| | b | -0.034 | **-0.032** | -0.039 | 0.012 | -0.124 | 0.026 | 0.057 | 0.026 | -0.110 |
| | RMSE | 0.009 | **0.007** | 0.008 | 0.009 | 0.009 | 0.010 | 0.008 | 0.008 | 0.008 |
| | RRMSE | 44.456 | **32.708** | 39.790 | 41.267 | 43.871 | 48.434 | 38.446 | 36.061 | 38.874 |
| | NSE | 0.625 | **0.788** | 0.696 | 0.618 | 0.599 | 0.537 | 0.699 | 0.735 | 0.689 |
| | $R^2$ | 0.624 | **0.785** | 0.677 | 0.657 | 0.602 | 0.565 | 0.698 | 0.742 | 0.693 |
| **$CWC_Q$** | m | 0.084 | **0.157** | 0.103 | 0.080 | 0.150 | 0.090 | 0.228 | 0.077 | 0.143 |
| | b | -0.025 | **-0.026** | -0.029 | 0.010 | -0.108 | 0.020 | 0.047 | 0.021 | -0.093 |
| | RMSE | 0.008 | **0.004** | 0.006 | 0.007 | 0.006 | 0.008 | 0.005 | 0.006 | 0.004 |
| | RRMSE | 45.847 | **27.564** | 40.840 | 43.851 | 34.747 | 50.985 | 29.104 | 34.625 | 28.333 |
| | NSE | 0.564 | **0.856** | 0.664 | 0.622 | 0.743 | 0.461 | 0.828 | 0.735 | 0.834 |
| | $R^2$ | 0.486 | **0.869** | 0.680 | 0.609 | 0.746 | 0.470 | 0.827 | 0.730 | 0.832 |

Finally, the comparisons between empirical and physical models using the Taylor diagrams are presented in **Figure 21** and **Figure 22**. We decide to use for this comparison $FMC_Q$ and $CWC_Q$ rather than $FMC_{EWT}$ and $CWC_{EWT}$ as this sample is less prone to uncertainties.

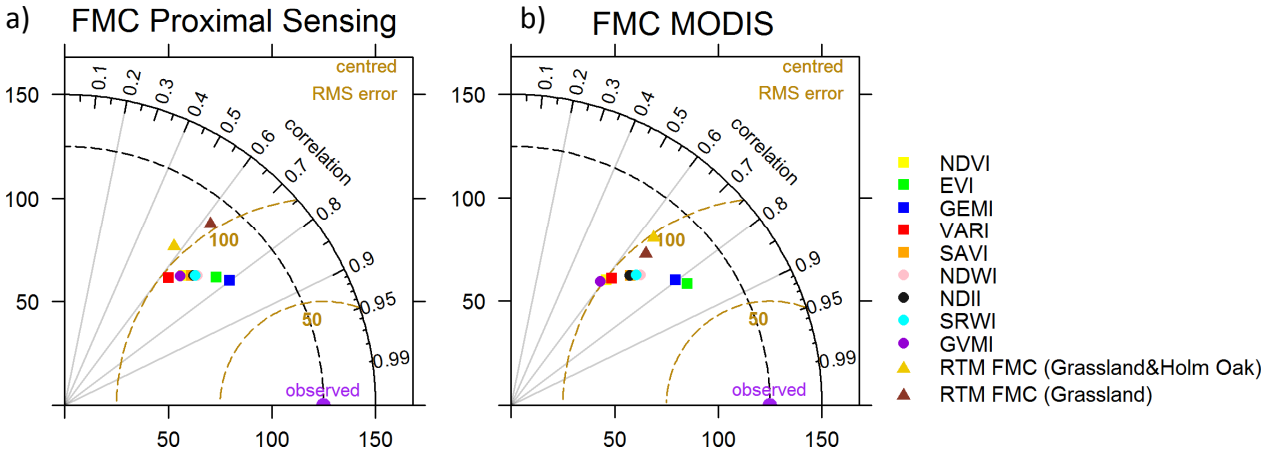


**Figure 21.** Comparison of empirical vs RTM models to estimate FMC with a) proximal sensing and b) MODIS. Square markers are used to represent the spectral indices using NIR information. Circles are used to represent the indices using SWIR information and triangles represent the RTM.

As it can be observed in the FMC plot (**Figure 21**a), RTM presented higher RMSE and lower correlation coefficient than the empirical models whereas RTM SD was the most similar to the observed FMC. In the case of FMC estimated from MODIS (**Figure 21**b), RTM were closer to the empirical models and EVI was the best followed by GEMI, appearing slightly apart from the rest of the models. In the case of proximal sensing, GEMI showed the best results followed by EVI. For CWC (**Figure 22**), the RTM from proximal sensing overestimated the SD and the RMSE of the observed CWC. VARI performed the worst with lower r, a larger RMSE and SD, whilst the NDII did the best followed by the GVMI. At MODIS scale (**Figure 22**), RTM showed a very high overestimation of the CWC SD and EVI and SRWI was the best and VARI the worst. It is noteworthy that MODIS empirical estimates are the closest to the *in situ* measurements. On the other hand, the RTM estimates of CWC showed good correlation values but poor SD results and RMSE.

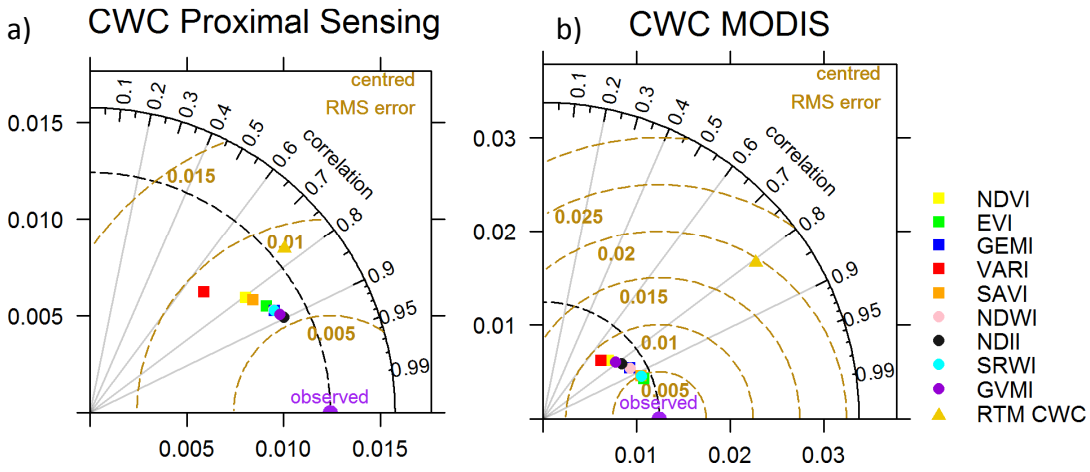


**Figure 22.** Comparison of empirical vs RTM models to estimate CWC with a) proximal sensing and b) MODIS. Square markers are used to represent the spectral indices using NIR information. Circles are used to represent the indices using SWIR information and triangles represent the RTM.

Temporal evolution of the biophysical variables estimated using the best model for proximal sensing and MODIS are shown in (**Figure 23)**. Both sensors predicted well EWT, $FMC_Q$ and $FMC_{EWT}$ but showed an overestimation, especially during the dry season. Contrary, the models for LAI, $CWC_{EWT}$ and $CWC_Q$ adjusted well even during the dry season. It can also be noticed the presence of an anomalous value in those variables affected by LAI. This day the grassland showed a very unusual growth, very dense and high. This made the size of the collected sample very large which could have introduced some noise to the data, probably because a large part of the plant area was outside the frame but was rooted inside the quadrant area. However, this is a hypothesis and could not be confirmed with the field notes, therefore the data was kept for the analysis.

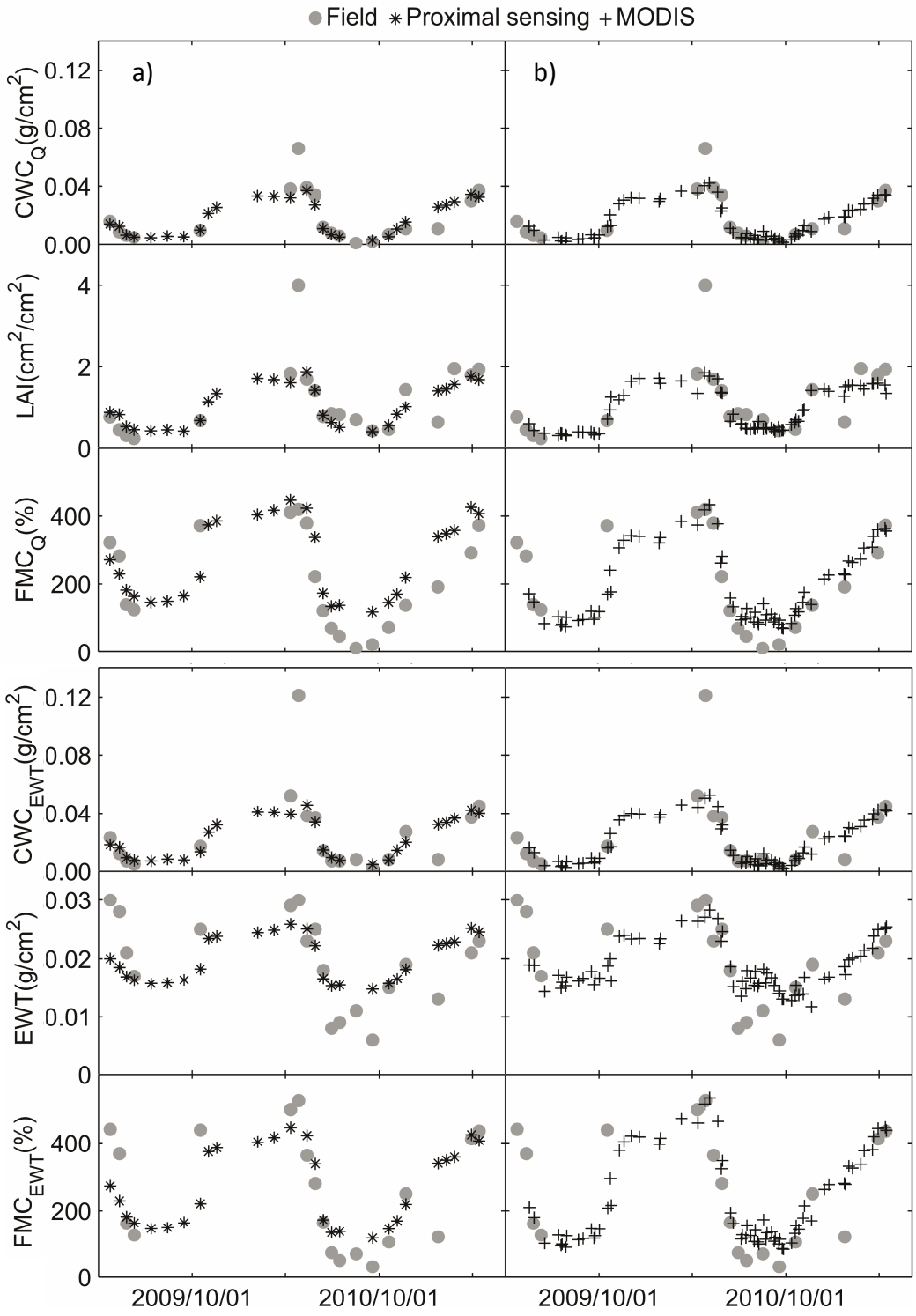


**Figure 23.** Temporal evolution of the observed (circles) and estimated $FMC_{EWT}$, $FMC_Q$, EWT, LAI, $CWC_{EWT}$ and $CWC_Q$ obtained for proximal sensing and MODIS. Left column a) compares observed data and proximal sensing. Right column b) compares observed data and MODIS.

## 3.3 Discussion

The results presented in this study revealed that Dm varied significantly throughout the year (CV=47 %) with high values in the summer. Temporal variation in the plant community structure (species composition and diversity) (Casado et al. 1986) could explain these high CV values for DM. Dm is one of the inputs in widespread leaf level RTM such as PROSPECT (Jacquemoud and Baret 1990) at leaf level, and therefore an accurate estimate of this variable will guarantee good RTM inversions. Summer should be the best time of the year to invert RTM and predict Dm, since leaves are drier and therefore EWT does mask the Dm spectral absorption signal (Riaño et al. 2005). Casas et al. (2014) applied a constant annual Dm value from the literature to successfully predict seasonal variations in EWT and CWC, however, our study confirms that due to the high seasonal variation in Dm, a constant annual value would not work for the ecosystem analyzed.

The spatial variation within the MODIS pixel was not as critical as its temporal trend (**Figure 20**). Therefore, the strategy to capture better the variability of vegetation water content in this ecosystem should be to sample fewer plots but more times. In regards to the sampling protocol, the poor correlations for EWT in **Figure 20** suggest weakness in the sampling strategy for this metric. In addition, $CWC_{EWT}$ and $FMC_{EWT}$, generated from the $EWT_{Sample}$, presented lower inter-group $R^2$ values than $CWC_Q$ and $FMC_Q$, which could be interpreted as a lower characterization of the temporal variability by the $EWT_{Sample}$. Impact of differences in sampling strategy consisting on collecting all plants included in a fixed sampling quadrant or visually selecting a representative sample from outside needs to be further investigated. However, the $EWT_{Sample}$ is subject to operator interpretations and therefore this could lead to bias in the sample. This suggests the need to standardize sampling protocols for the estimation of vegetation biophysical parameters to ensure data quality, repeatability and to facilitate accurate cross comparison from different studies. Some initiatives already exist to facilitate this standardization, as the Global Terrestrial Carbon System (GTOS) guidelines in support of carbon cycle science (Law et al. 2008) or more recent proposals oriented to measure gas concentration using EC like the one presented by Aubinet

and Papale (2014). However, currently there is no international backbone that ensures this and agreement in the protocols between the EC and the Remote Sensing communities is needed to make field datasets comparable.

CWC was better predicted than the other two water content variables, FMC and EWT (**Figure 20**). CWC depends on LAI which is even higher correlated than those two variables. It is possible to have the same FMC and EWT for different LAI and hence different CWC and amount of soil background, which will change its reflectance at canopy level. Yebra et al. (2013) demonstrated through PROSAILH simulations how a very different CWC for the same EWT based on changes of LAI translates into a huge range of NDII values. Our results confirm this theoretical expectation described in Yebra et al. (2013) (**Figure 24**). This issue is especially critical over areas with large annual growth dynamic, such as annual grass or crops.

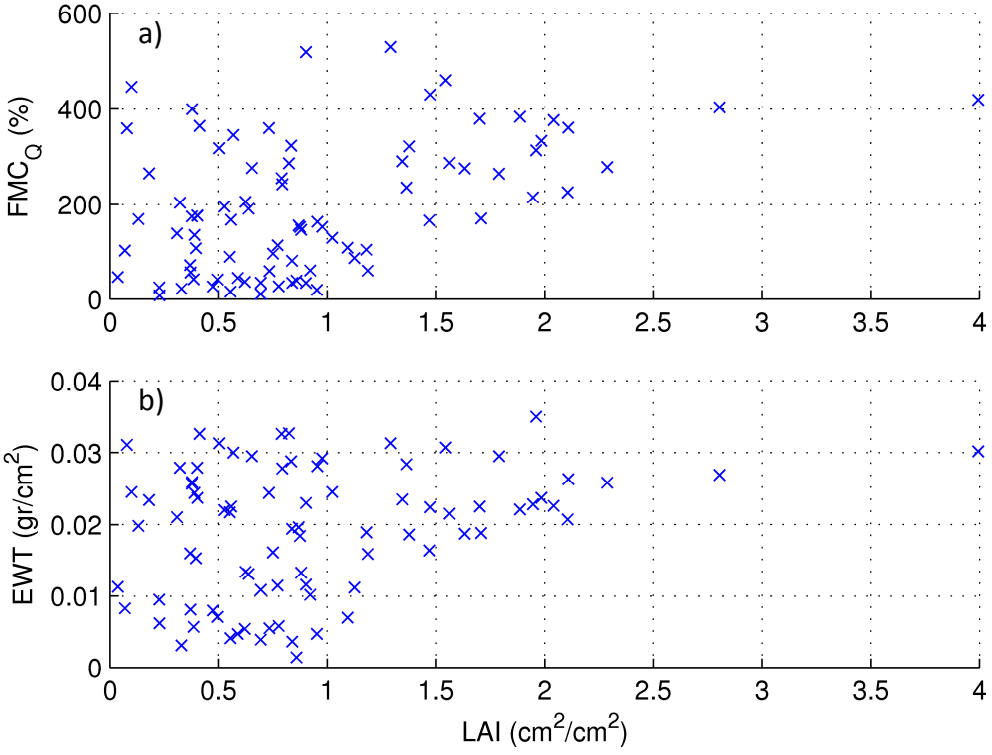


**Figure 24.** Relationship between a) FMC and LAI , and b) EWT and LAI.

The empirical methods estimated FMC and CWC with slightly different results for proximal sensing and MODIS (**Table 6** and **Table 7**). While GEMI and NDII estimated best FMC and CWC respectively from proximal sensing; EVI was the best estimator of both variables from MODIS. Differences can be explained by the fact that proximal sensing provides only nadir measurements while MODIS view observation angle could be up to 20° in our study case (Section 2.5.3.1). Additionally, MODIS pixel included grasslands but also trees, their shades, and other marginal covers such as bare soil and a water pond (**Figure 18**). Summer periods presented slightly lower agreement than the rest of the year with proximal sensing and with MODIS. Our guess is that this effect is caused due to missing data during summer of 2009, which makes the calibration biased for low values. In addition, it is remarkable that MODIS estimations were better than proximal sensing. Differences in the statistics between MODIS and proximal sensing can be explained due to the differences in the observation geometry and FOV, with the proximal sensing data to be more affected by soil signal as a nadir observation is. On the other hand in MODIS observations this effect is reduced and the signal is less affected by the soil. This is especially important during the dry periods because the tree cover is very adapted to hydric stress and hence trees remain almost invariant (Liesenberg et al. 2007). As consequence of this, the spectral indices from MODIS present less variation than those from proximal sensing (**Figure 23**) and can be translated in a better performance of the empirical models.

Casas et al. (2014) found also that GEMI, NDII and EVI had potential to predict water content variables in California (USA), but VARI was their best choice for grasslands (FMC and CWC), chaparral (EWT, FMC and CWC) and a Mediterranean oak forest (EWT). In our study, VARI showed very poor results to estimate FMC, EWT, CWC and better estimates for LAI. This also contradicts other studies that predicted FMC on chaparral (Peterson et al. 2008; Roberts et al. 2006; Stow et al. 2005, 2006). A hypothesis to explain our result is that VARI was developed for homogenous crops with similar LAI (Gitelson et al. 2002b). In this study total LAI was calculated rather than green LAI, which accounts only for the photosynthetic part of the vegetation. When vegetation is growing and is not under

water limited conditions total LAI and green LAI are similar, however, during senescence large differences between both LAIs are expected. As presented here, FMC and EWT are not vegetation water content metrics related to LAI (**Figure 24**) and this explains the weak relationship. CWC is related to LAI and, therefore, a stronger relationship was expected with VARI. However, as it has been previously mentioned, the LAI protocol followed in this study accounts for the total LAI and this reduces the link between LAI and vegetation water content.

The empirical methods calibrated for this specific site outperformed the physical RTM estimates for CWC and FMC (**Figure 21** and **Figure 22**). This confirms the results in Trombetti et al. (2008) were CWC based on RTM also failed to improve results from empirical estimates in Casas et al. (2014) study. Inversion of RTM overcome empirical approaches when structural information of the canopy constrains the model inversion (Casas et al. 2014; Yebra et al. 2008a) and under other situations where multiple observations can be retrieved, by using more robust algorithms that are not based on LUTs such as optimization algorithms. Such information is required to successfully extrapolate a RTM inversion at broader scale.

# 4 Soil Moisture

## 4.1 Methodology

For this study SEVIRI and MODIS were used (Figure 5). Contrary to previous section, MODIS Images with a VZA lower than 55°, instead of 20° were selected in order to reduce angular effects in both VI and Ts but, at the same time maintain as much as possible the temporal resolution. The VIs were obtained from the MOD09GA product. NDVI and NDII were calculated using MODIS bands 1 (red, 0.648 μm), 2 (NIR, 0.854 μm), and 6 (SWIR, 1.640 μm) (**Table 5**).

With MODIS, a proxy to the morning temperature rise of the surface (δTs) was calculated as:

$$\partial Ts = \left| \frac{Ts_{TerraDay} - Ts_{AquaNight}}{\partial t} \right| \qquad \textbf{(Equation 17)}$$

where $Ts_{TerraDay}$ is the Terra Ts during the morning overpass, $Ts_{AquaNight}$ is the Aqua Ts during the night overpass and $\partial t$ is the absolute time difference between the day-night overpasses. Previous studies that combined day and night MODIS overpasses (Guzinski et al. 2013) found improvements in the estimation of the Evaporative Fraction using the triangle technique (Rasmussen et al. 2014; Wang et al. 2006a).

Finally with SEVIRI data, thermal inertia was estimated using the δTs method described in Stisen et al. (2008b) as the slope of the linear fit between Ts and time for all the cloud-free images acquired between 08:00 UTC and 12:00 UTC. Quality of the δTs data neglected the cases where the $R^2$ of the linear fit of the temperature rise was lower than 0.95 (**Figure 25**).

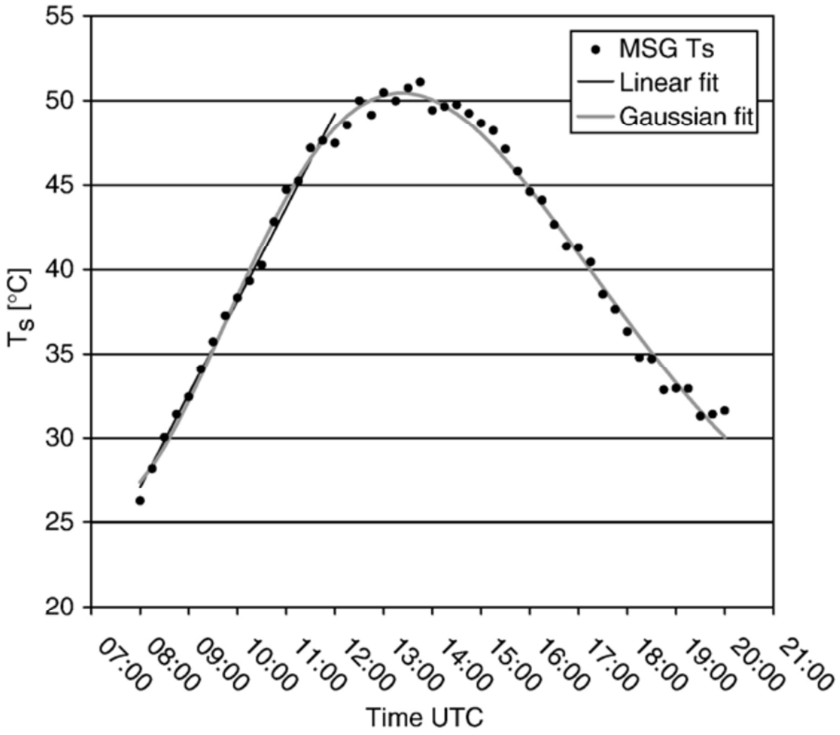


**Figure 25.** δTs from MSG-SEVIRI and linear fitting to morning temperature rise. Taken from Stisen et al. (2008b)

### 4.1.1 TVDI

For this study a window of 50x50 pixels for SEVIRI (200 km side) and 74x74 pixels for MODIS (74 km side) centered at the FLUXNET site was selected ensuring atmospheric homogeneity, sufficient number of pixels and presence of all soil moisture and vegetation cover conditions (**Figure 26**).

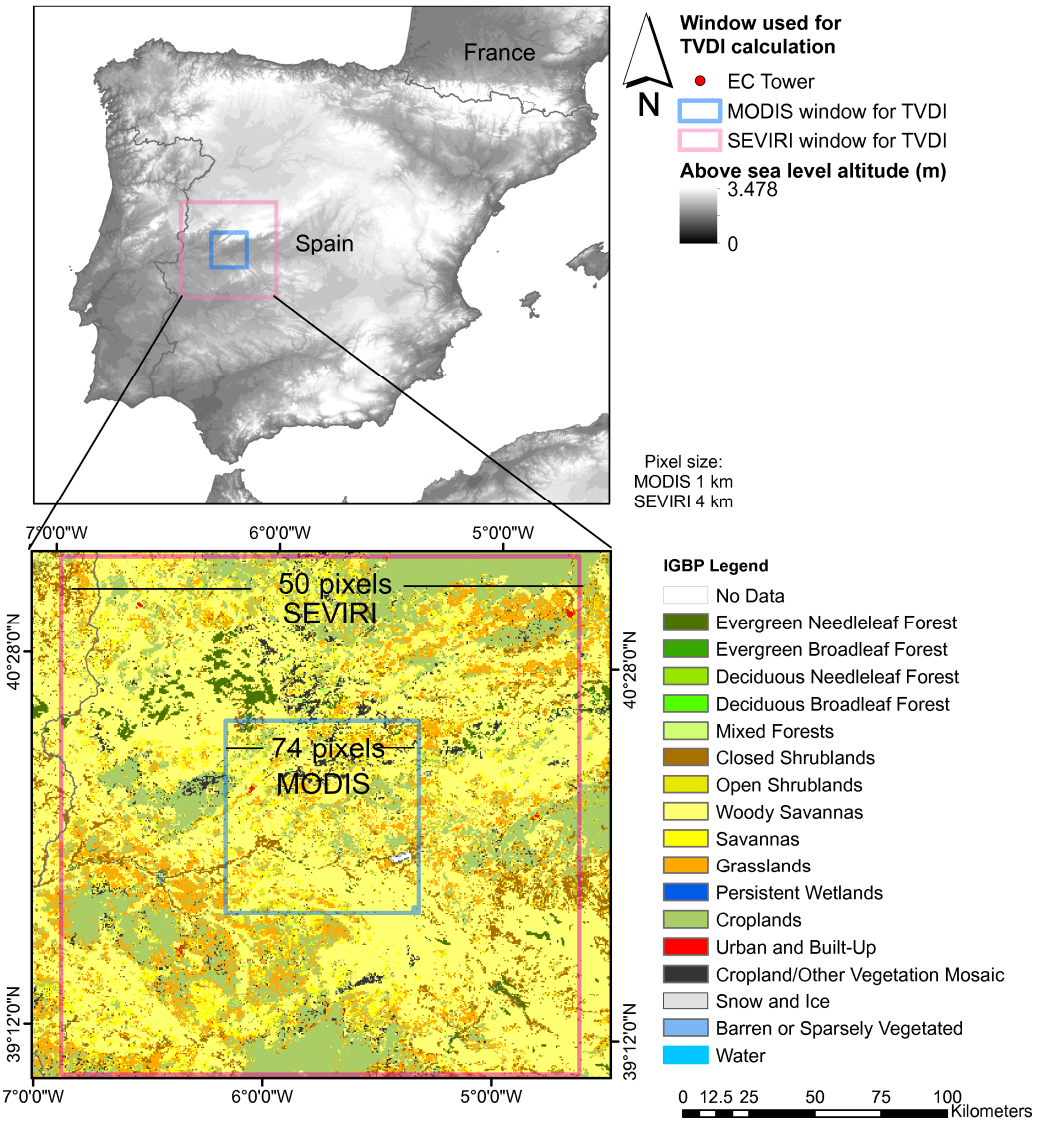


**Figure 26.** Windows used to calculate the TVDI for MODIS and SEVIRI.

Different masks were built for SEVIRI and MODIS images in order to ensure the quality of the pixels. First we created clouds and shadows masks for each scene, based on the quality assesment in the case of MODIS and the cloud mask provided by EUMESAT in the case of SEVIRI (http://www.eumetsat.int/website/home/index.html last accessed 2013/11/15). Then we removed forest, urban areas and water bodies based on MODIS MCD12Q1 IGBP land cover map (https://lpdaac.usgs.gov/products/modis_products_table/mcd12q1) as they present different aerodynamic roughness (Sandholt et al. 2002; Stisen et al. 2008b)

and therefore are not appropriate for TVDI calculation. TVDI was calculated using only unmasked pixels within each spatial window by combining different methods for retrieving the dry and wet edges. For calculating the edges, in a first step we binned the NDVI and NDII in equal length intervals of 0.02, ranging from bare soil (NDVI=0.1 and NDII= -0.4) to the maximum VI found in the triangle. Secondly, we selected the minimum and maximum $\partial T_S$ values found in each of the VI bins. In what we called the "Simple" method, a regression line between the VI bin and the maximum $\partial T_S$ values was computed for the definition of the dry edge. Additionally, the dry edge was also estimated using the method proposed by Tang et al. (2010). The main advantage of this method is that is less sensitive to outliers as it adds additional sub-intervals to the initial bins, and obtains the average of the maximum $\partial T_S$ within the sub-interval falling within the standard deviation (SD) threshold of the bin. The selection of the maximum $\partial T_S$ is based on these two statistics and the relationships with the rest of the intervals. The wet edge was estimated using either the Mean or the Median value of the minima δTs, from the ten bins with highest VI ( **Figure 27**).

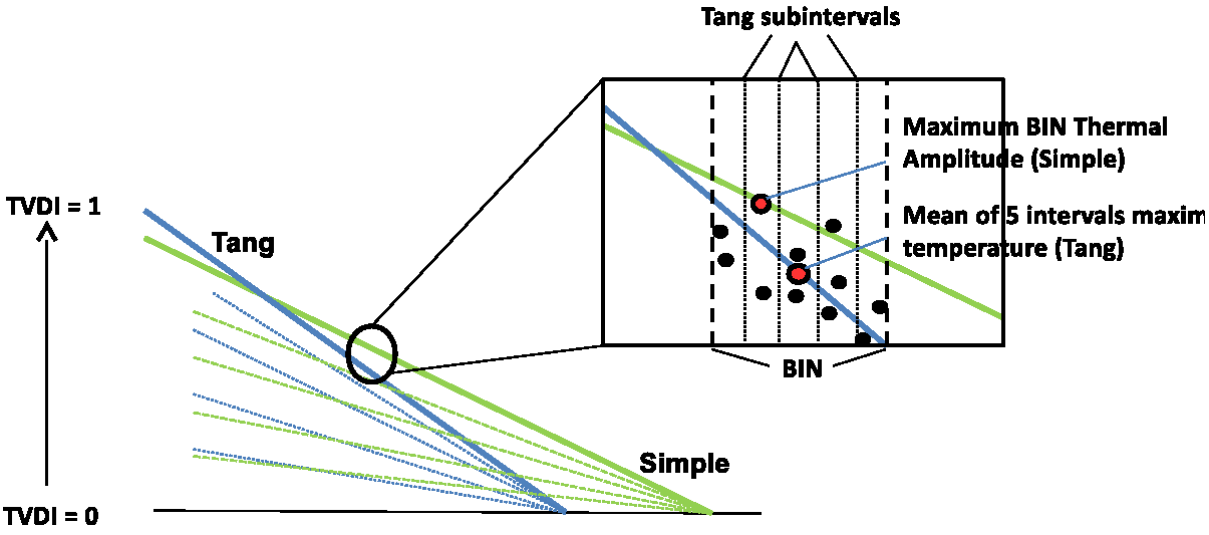


**Figure 27.** Comparison of simple and Tang method to calculate the points that are going to be used in the dry edge calculation. Black dots represent the points in the VI-Ts space, and red dots represent the calculated points with each of the methods.

Once the edges were defined, the TDVI was computed as (Sandholt et al. 2002):

$$TVDI = \frac{\partial Ts - \partial Ts_{Min}}{a + b\,VI - \partial Ts_{Min}} \qquad \textbf{(Equation 18)}$$

where $\partial T_{S\,Min}$ is the value of the wet edge, $a$ and $b$ are the intercept and slope of the dry edge, and VI is the spectral index used, either NDVI or NDII.

The analysis gave a total of 16 different TVDI calculations (2 dry edge methods x 2 wet edge methods x 2 VIs x 2 sensors). Linear regression models between the field TDR SM measurements for each 4 SM depths and the TVDI values from the pixel that contained the TDR instruments were established using a bootstrap technique (Efron and Gong 1983). Taylor diagrams (Taylor 2001) were used to evaluate the models and to select the best performing method at each soil depth. Once the best model was selected, its performance and predictability was evaluated using a second bootstrap with 200 repetitions (Steyerberg et al. 2001) to calculate the RMSE, Nash-Sutcliffe Efficiency index (NSE) and the Determination Coefficient ($R^2$), following the recommendations of Richter et al. (2012). Best performing models will be used in the final analysis to retrieve map SM in summer and winter.

## 4.2 Results

Analysis was carried out only for those dates when both SEVIRI and MODIS data were available to ensure comparability of the models. The results of these comparisons are presented using Taylor diagrams in **Figure 28**. As it can be observed, the performance of those models in which TVDI was calculated using the NDII outperformed those in which the NDVI was used. Regarding the dry edge estimation method, in the case of MODIS images, the Simple method offered the best agreement with observed data with higher correlation values, lower RMSE and more similar SD to field observations.

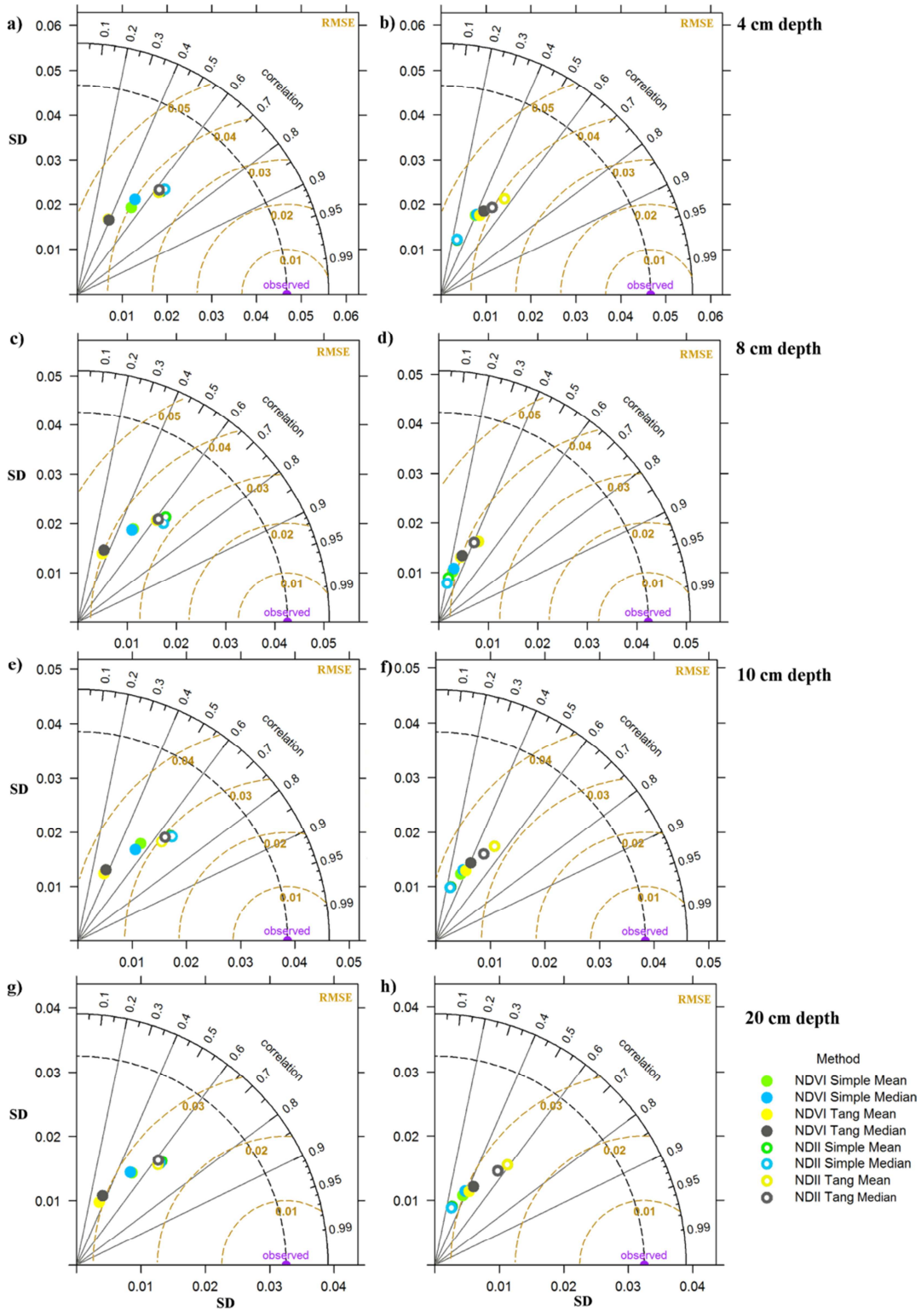


**Figure 28.** Model performance comparison using the Taylor diagrams at four SM depths. Colors indicate different edges/VI combinations. Left column corresponds to MODIS and right column corresponds to SEVIRI.

On the other hand, SEVIRI showed best agreement with dry edge determined using Tang. In terms of soil depth, the agreement was best at 8 and 10 cm for MODIS but at 20 cm for SEVIRI. Detailed statistics of the best models are shown in **Table 8**. Results indicate a statistically better model performance with MODIS than with SEVIRI with higher $R^2$ and NSE values. SD of the statistics was estimated from the bootstrap, and shown in **Table 8**, except for m and b. The statistics showed that for MODIS the fitting parameters of the model (m ´and b´) presented higher SD values. For the error statistics the SD showed very similar values in both platforms.

**Table 8.** Slope (m) and intercept (b) for the fitting equations of the best performing models at each soil depth for MODIS and SEVIRI, and their values using bootstrap in the calibration (m' and b'). Statistics after the bootstrap process include the m', b', RMSE, NSE and $R^2$, together with their SD to the right of these parameters.

| Depth | m | b | m' | *stdv* | b' | *stdv* | RMSE (%Vol) | *stdv* | NSE | *stdv* | $R^2$ | *stdv* | Method |
|---|---|---|---|---|---|---|---|---|---|---|---|---|---|
| **4 cm** | 0.278 | 0.239 | 0.278 | 0.028 | 0.239 | 0.019 | 0.060 | 0.006 | 0.354 | 0.073 | 0.355 | 0.068 | NDII Simple Mean |
| **8 cm** | 0.233 | 0.233 | 0.237 | 0.027 | 0.254 | 0.017 | 0.048 | 0.003 | 0.373 | 0.070 | 0.374 | 0.075 | NDII Simple Mean |
| **10 cm** | 0.215 | 0.215 | 0.215 | 0.023 | 0.222 | 0.015 | 0.043 | 0.003 | 0.392 | 0.063 | 0.386 | 0.071 | NDII Simple Mean |
| **20 cm** | 0.156 | 0.1866 | 0.158 | 0.024 | 0.187 | 0016 | 0.039 | 0.003 | 0.270 | 0.071 | 0.275 | 0.073 | NDII Simple Mean |

| Depth | m | b | m' | *stdv* | b' | *stdv* | RMSE (%Vol) | *stdv* | NSE | *stdv* | $R^2$ | *stdv* | Method |
|---|---|---|---|---|---|---|---|---|---|---|---|---|---|
| **4 cm** | 0.163 | 0.153 | 0.160 | 0.023 | 0.151 | 0.015 | 0.058 | 0.006 | 0.288 | 0.071 | 0.286 | 0.074 | NDII Tang Mean |
| **8 cm** | 0.116 | 0.168 | 0.116 | 0.016 | 0.168 | 0.010 | 0.048 | 0.004 | 0.233 | 0.072 | 0.241 | 0.068 | NDII Tang Mean |
| **10 cm** | 0.120 | 0.152 | 0.119 | 0.014 | 0.151 | 0.009 | 0.043 | 0.003 | 0.291 | 0.074 | 0.296 | 0.073 | NDII Tang Mean |
| **20 cm** | 0.105 | 0.145 | 0.107 | 0.014 | 0.146 | 0.009 | 0.039 | 0.004 | 0.271 | 0.078 | 0.280 | 0.080 | NDII Tang Mean |

In **Figure 29** and **Figure 30,** scatterplots showing the relationship of TVDI values when it is calculated using Tang vs Simple, and Mean vs Median methods to define the dry edge and wet respectively are presented. For both MODIS and SEVIRI images, higher values are observed when Tang is used instead of Simple to define the dry edge, and almost no differences when mean or median are used to define the wet edge.

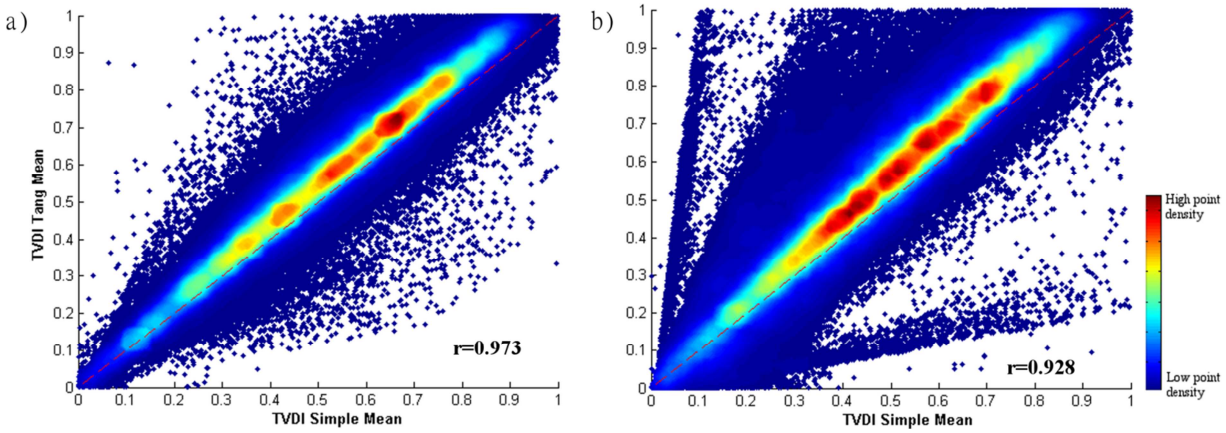


**Figure 29.** MODIS a) SEVIRI b) TVDI image value comparison between Tang and Simple methods to define the dry edge.

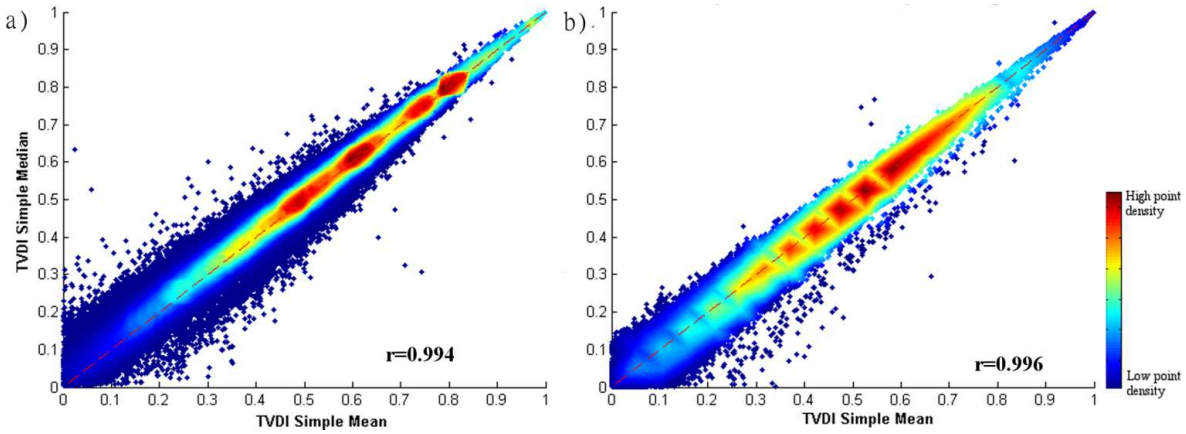


**Figure 30.** MODIS a) SEVIRI b) TVDI image value comparison between Mean and Median to define the wet edge.

## 4.3 Discussion

The best model to estimate SM using MODIS and SEVIRI using the triangle method was found in our case when NDII was used instead of NDVI with an improvement in the model performance in terms of correlation with field observation from 0.5 to 0.65. This can be explained because NDII is more sensitive to SM and highly related to LAI (Wang et al. 2008; Yilmaz et al. 2008; Zarco-Tejada et al. 2003) and therefore highly linked to water stress than NDVI, which is more sensitive to chlorophyll activity. The correspondence between both VIs and thermal amplitude observed with MODIS over all the year indicated that correlation between these two variables is lower with NDII (r= -0.488) than NDVI (r= -0.554). This fact suggests more information represented in the scatter plot when NDII is introduced, probably due to the higher sensitivity of this VI to moisture, both soil and vegetation. Recent studies have also noticed an improvement using NIR/SWIR index among others like NDVI when downscaling SMOS SM (Sánchez-Ruiz et al. 2014). TVDI permits monitoring the spatial and temporal variations in SM over an area of interest as other studies have already shown before (Holzman et al. 2014; Patel et al. 2008; Stisen et al. 2008b; Vicente-Serrano et al. 2004), however using NDII instead of NDVI improved the model performance. NDVI accounts mainly for chlorophyll activity and biomass whilst NDII is also related to biomass and water conditions, and thereby NDII is more related to ET than NDVI is.

Model calibration showed similar results than Sun et al. (2012) who applied a theoretical dry edge to find a $R^2$=0.36 between TVDI and SM for a larger number of points and different profile setup than our study. The statistics at different depths showed that TVDI is best correlated with the SM in the root zone area (8-10 cm) in the case of MODIS. Rapid SM variations at 4 cm depth were not observable by the TVDI as shown in **Table 8**. In contrast, SEVIRI showed the best results at 20 cm depth, which offers more stable SM values. This could be explained due to the constant observation geometry of SEVIRI leading to the TVDI values being more influenced by the tree cover signal (Rasmussen et al. 2010), especially important in

areas such as savannas or woody savannas, that include vegetation types that usually present a deeper root system. Model fitting statistics (m and b) showed very similar values when calculated in the initial stage (no bootstrap) and when calculated using bootstrap (m' and b') suggesting that the coefficients are robust.

Furthermore, TVDI values increase when Tang dry edge is applied. In **Figure 31** an ideal theoretical triangle was plotted defining the hypothetical Simple and Tang dry edges. As it can be observed, Tang's dry edge presents a higher slope than Simple. There are some coincident TVDI values for both methods in the central part of the plot that correspond to the isolines where the two methods intersect. To the left of this area, TVDI is higher for Simple than for Tang, and the opposite occurs to the right. Depending on the relationship between the slopes of the two methods, the same area can present higher TVDI values according to its relative position in the triangle. In our study case we found that the majority of the pixels presented higher TVDI values for Tang, but this could be the opposite for other sites, as the intersection of the isolines could be displaced in a different way.

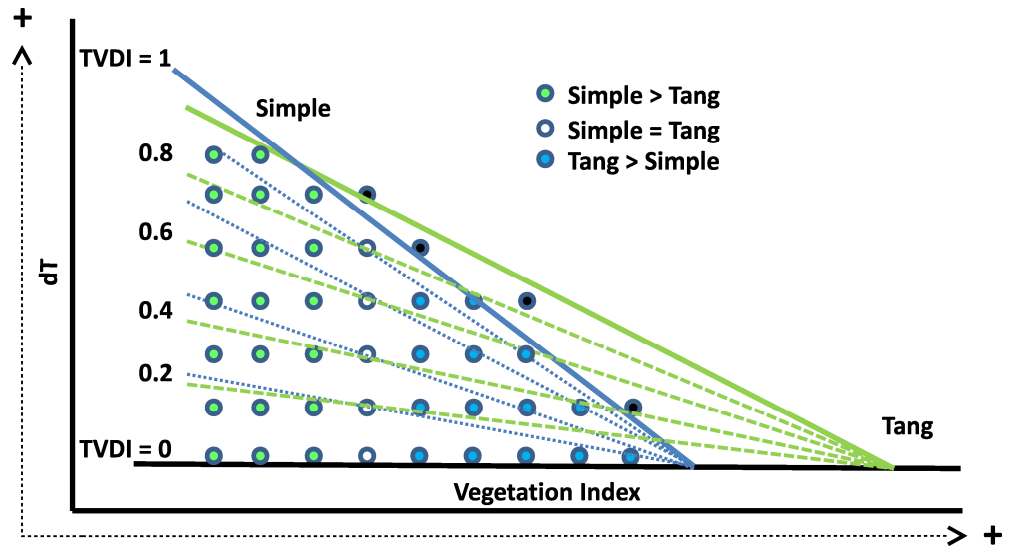


**Figure 31.** Ideal theoretical relationship between TVDI using the Simple (green line) and Tang (blue line) dry edge methods.

Differences in the dry edge slope are explained because Tang method calculates the average value of the maxima of the 5 subintervals inside each bin, while Simple uses single maximum value inside each bin. Additionally, Tang method

test the data selected to calculate the average maximum $\partial Ts$ and later, when the linear regression is established, neglects those points in which the maximum $\partial Ts$ for a given interval is further than $\pm$ 2 times the RMSE away from the $\partial Ts$ of the regression line (Tang et al. 2010). In the case of MODIS the differences in dry edge slope result in steeper slopes when Simple method is applied (**Figure 32**a). This differs from SEVIRI where Tang method presents steeper slopes (**Figure 32**b).

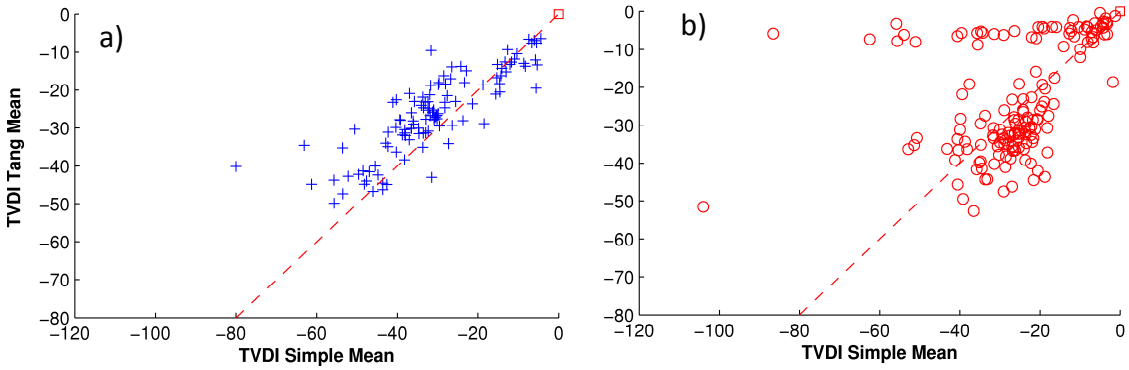


**Figure 32.** Comparison of the dry edge slope values for MODIS (blue crosses) and SEVIRI (red circles) between Tang and Simple methods.

This opposite behavior could be related to the discrepancies between the MODIS 1 km and SEVIRI 4 km spatial resolution. MODIS can better differentiate between bare soil areas and fully vegetated areas than SEVIRI, due to its higher spatial resolution and in some cases, lower viewing angles than SEVIRI. In the case of MODIS, Tang method does not take many points around the intersection of the wet and dry edges, where VI is maximum, and therefore it shows gentler slopes than Simple (**Figure 33**a and b). In the case of SEVIRI, the opposite (**Figure 33**c and d) occurs.

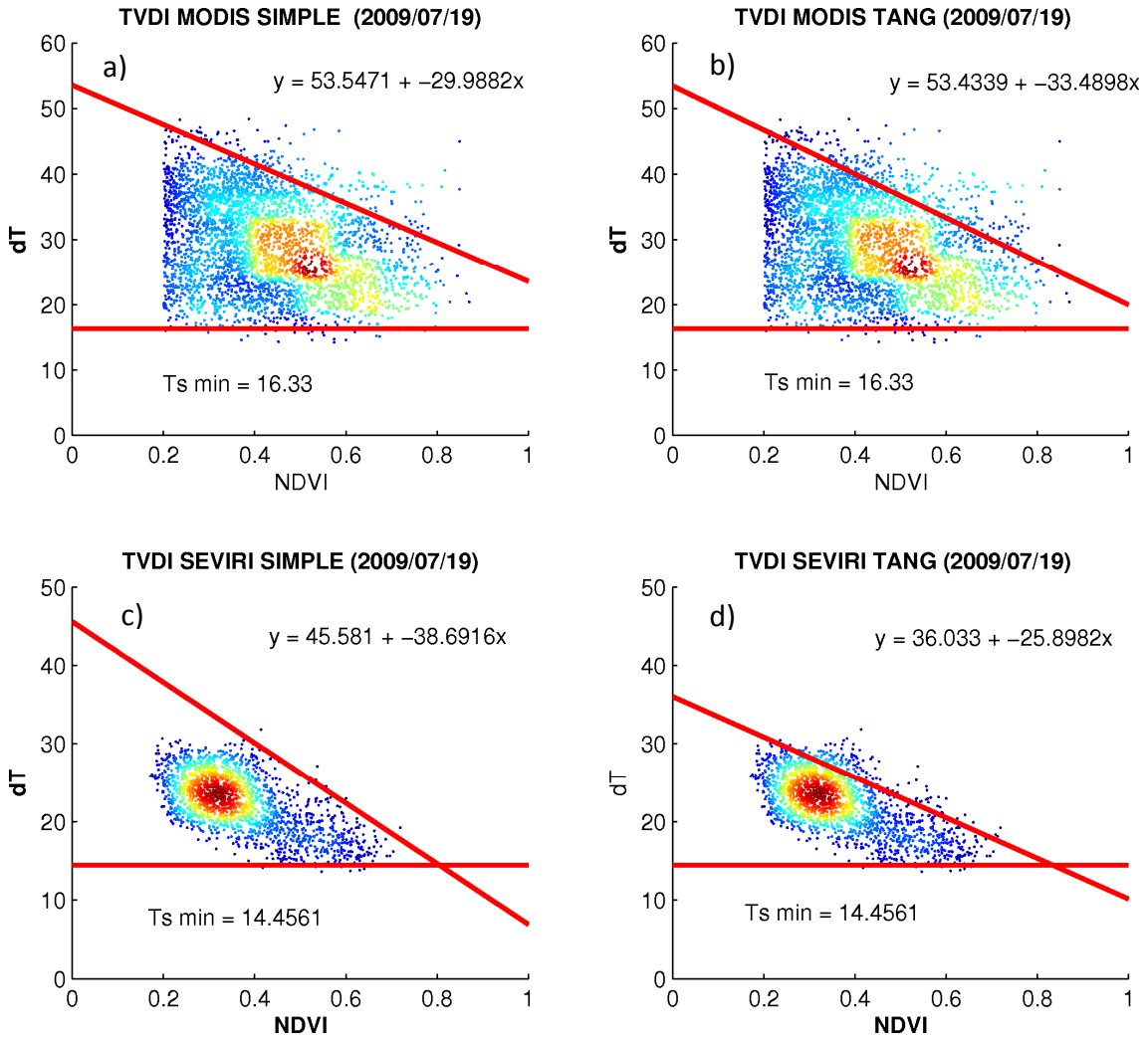


**Figure 33.** Simple and Tang dry edge obtained for the same day (2009/07/19) from MODIS (a and b) and SEVIRI (c and d), respectively. Simple method is shown in the left column and Tang method in the right column. All examples are calculated with the NDVI and Mean for the wet edge.

The edge definition is more accurate for MODIS than for SEVIRI. MODIS presents better spatial resolution that can differentiate pure pixels. The window size is smaller, and therefore more similar weather forcing conditions with a larger number of pixels, and therefore the RMSE interval used in Tang is smaller. Despite MODIS defines the vertex of the triangle better, as pure pixels are more frequent than in SEVIRI, Tang´s algorithm in this study did not select these points for the dry edge definition, probably due to a small number of pixels and therefore the

algorithm did not use them as they were out of the bounds of the RMSE criterion for the point selection.

The theoretical dry edge is defined by those points where zero ET occurs. As Stisen et al. (2008b) mentioned, soil water uptake from the root zone occurs in dense vegetated areas and this leads to lower Ts than the theoretical ones resulting in an observed dry edge usually below the theoretical one. Sun et al. (2012) indicated that the theoretical edge lead to higher correlation values between TVDI and SM. Our results presented best results with methods that showed the less steep slopes in the dry edge in agreement with other studies that found these cases closer to the theoretical dry edge (Goetz 1997; Sun et al. 2012). Long et al. (2012) mentioned the difficulties of low spatial resolution data in distinguishing very wet surfaces using the triangle method over small areas. In our study case we have to consider also the effect of the viewing geometry of the sensor. In our study site SEVIRI observes at a constant viewing angle of 46°. This reduces the fraction of soil observed due to interception of the tree canopy and hence it becomes more difficult to find pure soil areas for the edge definition. On the other hand, the definition of the wet edge using the Mean or Median methods did not show much effect on the final TVDI values since both methods were based on the same points.

Finally, **Figure 34** presents the estimated SM with MODIS images at two different dates (summer and winter) using the empirical model that showed the best results at 10 cm depth with MODIS (NDII with Simple dry edge and Mean wet edge) lower SM values in the dry period (2009/07/19), with irrigated croplands in the center of the scene (black ellipsoid). Other areas with high SM correspond to more vegetated areas corresponding to shrublands and forest. The image corresponding to the cold and wet season (2009/02/18) show higher SM values over the scene. These maps indicate that TVDI is capable of collecting the spatial variations in SM.

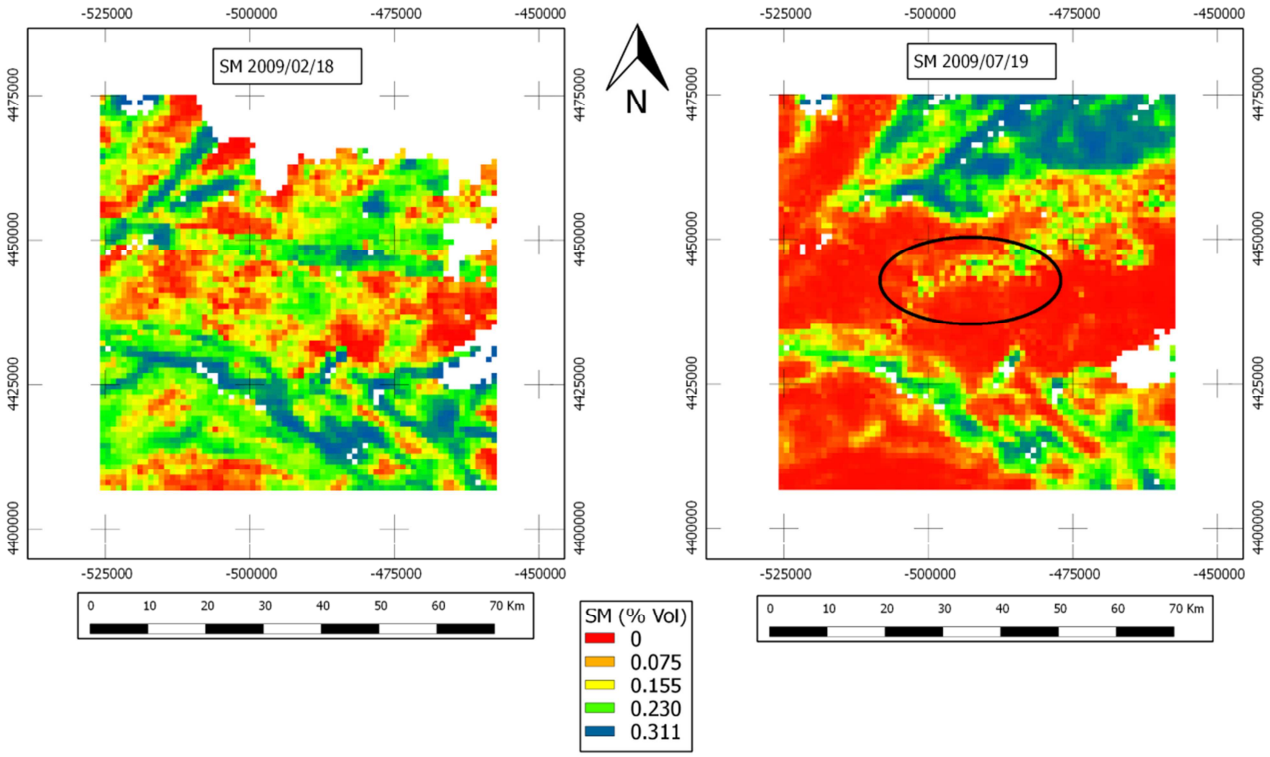


**Figure 34.** SM estimation at 10 cm depth from the best empirical performing model at two different dates (2009/02/18 and 2009/07/19), showing the differences in SM during winter and summer and the spatial variability. Pixels in black were removed by the mask. Black ellipsoid highlights the crop existing north from the EC tower.

# 5 Evaporative Fraction

## 5.1 Methodology

In this section the methods applied to estimate the evaporative fraction (EF) using the triangle method are described. EF has been estimated combining Ts and LAI derived from Landsat and MODIS data for the period from March 2009 to December 2011. Validation of EF was carried out using the Eddy Covariance (EC) flux tower measurements (**Figure 5** and **Figure 35**).

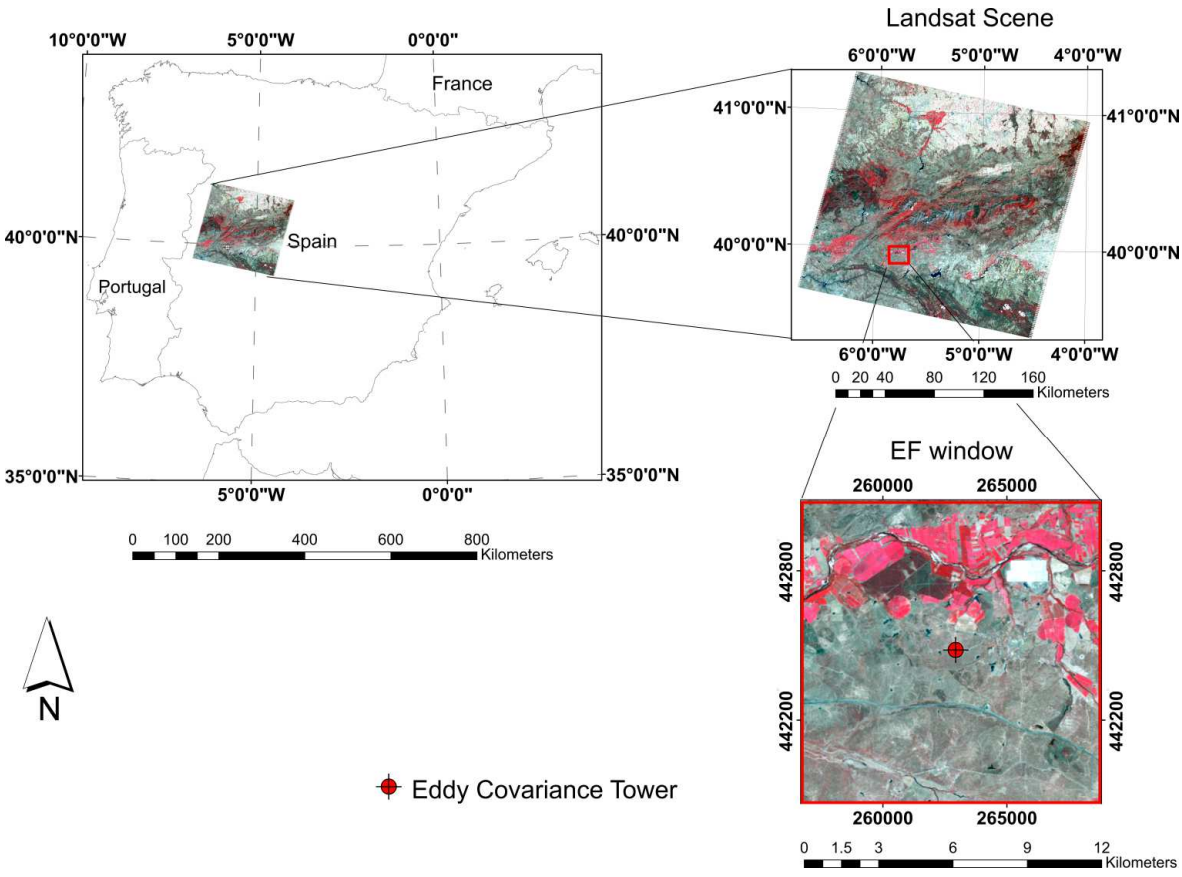


**Figure 35**.Site location and Landsat scene covering the study site area and image window used to calculate EF.

### 5.1.1 Eddy Covariance measurements and footprint

Using the LE measured from the EC flux tower (Section 2.3), EF was calculated using **Equation 1** for every data ranging from 9:00 to 17:00 UTC. Additionally an overpass EF (covering Landsat overpass which for our study site is around 10:50 UTC) was computed as the average of the 5 measurements from 10:00 to 12:00 UTC (**Figure 36**). The decision of using 5 measurements instead of only one corresponding to the overpass time was with the aim of minimizing the potential noise due to some instrumentation errors common when using the EC technique (Massman and Lee 2002).

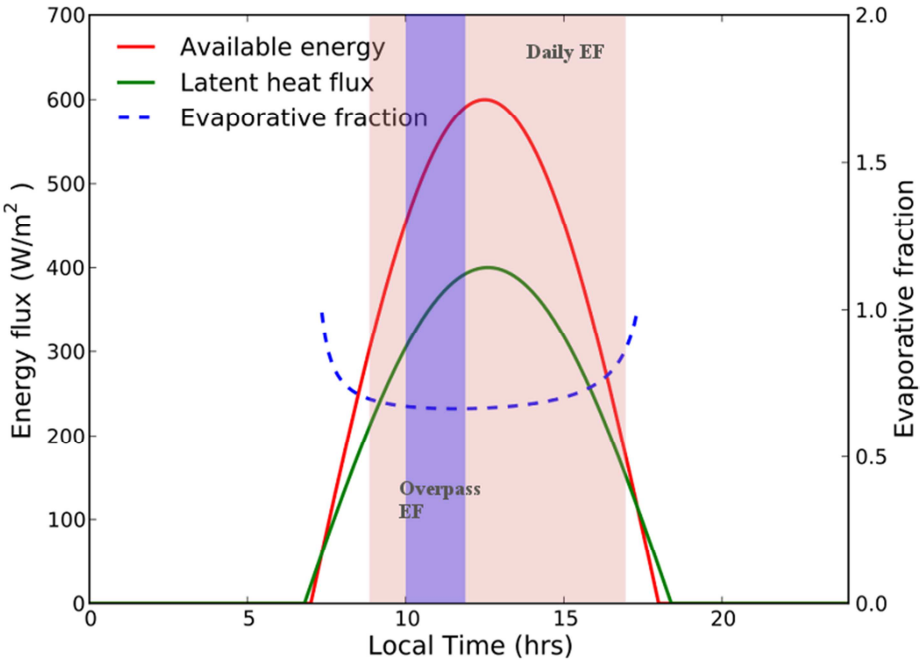


**Figure 36**. Typical daily EF evolution showing the time windows used to calculate daily and overpass EF. Figure modified after Peng et al. (2013).

As explained in Section 2.3, the specific EC tower footprint at the time of Landsat overpass was estimated in order to assign the contributions of each Landsat EF pixel to the total area of influence of the footprint, so the comparison between EF measured from the EC tower and the EF estimated from Landsat could be properly implemented. Landsat pixels were aggregated to the footprint

resolution in this process, and the total contribution was calculated. In those cases in which Landsat presented some areas without data within the footprint, mainly due to the stripes caused by sensor failure in Landsat 7 ETM or clouds; the algorithm was forced to calculate the EF based only on the valid pixels within the footprint (**Figure 37**).

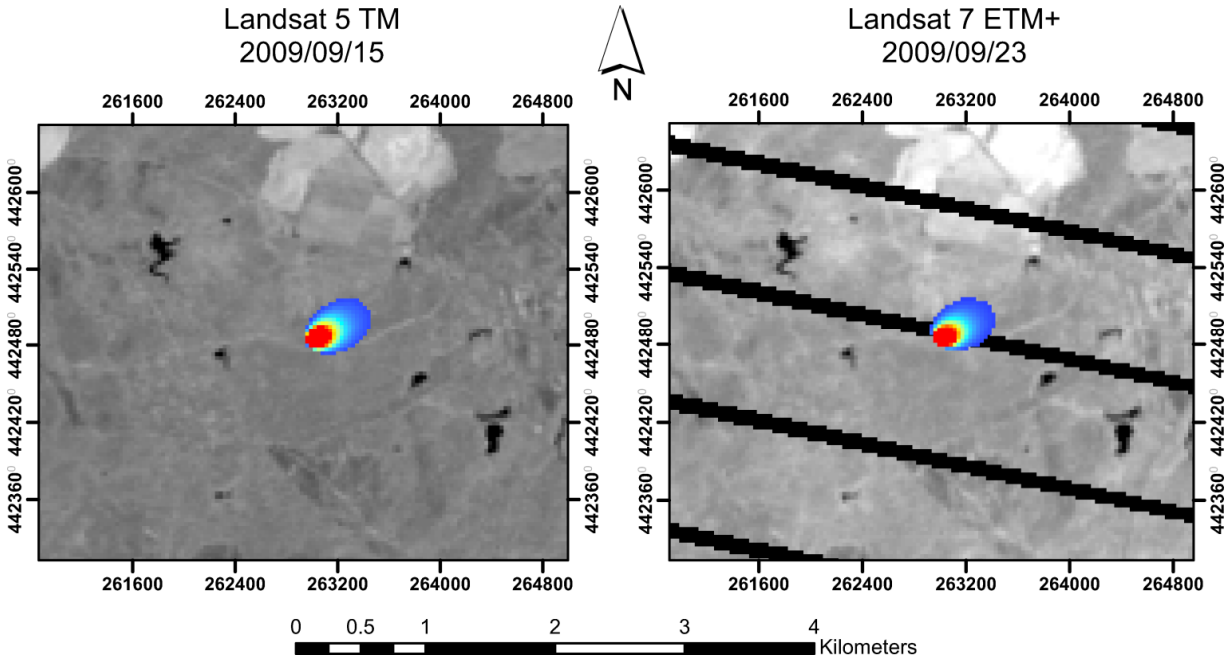


**Figure 37.** Band 1 surface reflectance of Landsat 5 TM and Landsat 7 ETM+ comparison. When the footprint is within the stripe area, only the valid pixels are used to calculate the contribution.

Statistics of the comparison between EF measured from the EC tower and estimated from Landsat data were obtained using bootstrap with 200 repetitions (Schlesinger and Bernhardt 2013) and following the recommendations by Richter et al. (2012)

### 5.1.2 Satellite pre-processing

For this study the LEDAPS corrected Landsat images (Section 2.5.2) were post processed by filtering out the low quality pixels affected by atmospheric disturbances and cloudy pixels. After that, a 12 km by 12 km window centered in

the EC tower was extracted from the scenes (**Figure 35**). This window dimension ensures enough number of pixels to calculate the edges of the triangle and at the same time guarantee homogeneous atmospheric forcing conditions. Finally, urban areas and larger water bodies included in the scene window where removed using a mask. This mask was generated by visually selecting these two different land cover types.

A decision tree regression algorithm proposed by Gao et al. (2012) was used to downscale the 1km MODIS LAI (Section 2.5.3.3) to 30m using Landsat optical data. First, MODIS LAI previous date to the Landsat overpass was selected to carry out the following steps. This algorithm aggregates the atmospherically corrected surface reflectance data from Landsat (bands 1-5 and 7) to match the 1 km pixel resolution of MODIS. Those 1 km LAI pixels with the best quality flags (SCF_QC=0 best result possible) are extracted to reduce the noise in the regression. A further mask is applied to the data selecting only the 1 km LAI pixels that show low spectral variability (CV < 20%) of the Landsat reflectances 30 m scale, ensuring the homogeneity of the pixel in the calibration of the regression tree. A total of 14 LAI classes were selected in the calibration tree process. Once the model is trained at the MODIS scale, LAI maps are produced at Landsat scale by applying the regression tree to the original reflectance Landsat at 30m (Gao et al. 2012). The resulting LAI image presented some noise, present as salt and pepper effect, therefore a low pass mean filter using a 3x3 pixel windows was applied to remove this effect in the scene (**Figure 38**). This noise could be due to border effects between covers with very different LAI.

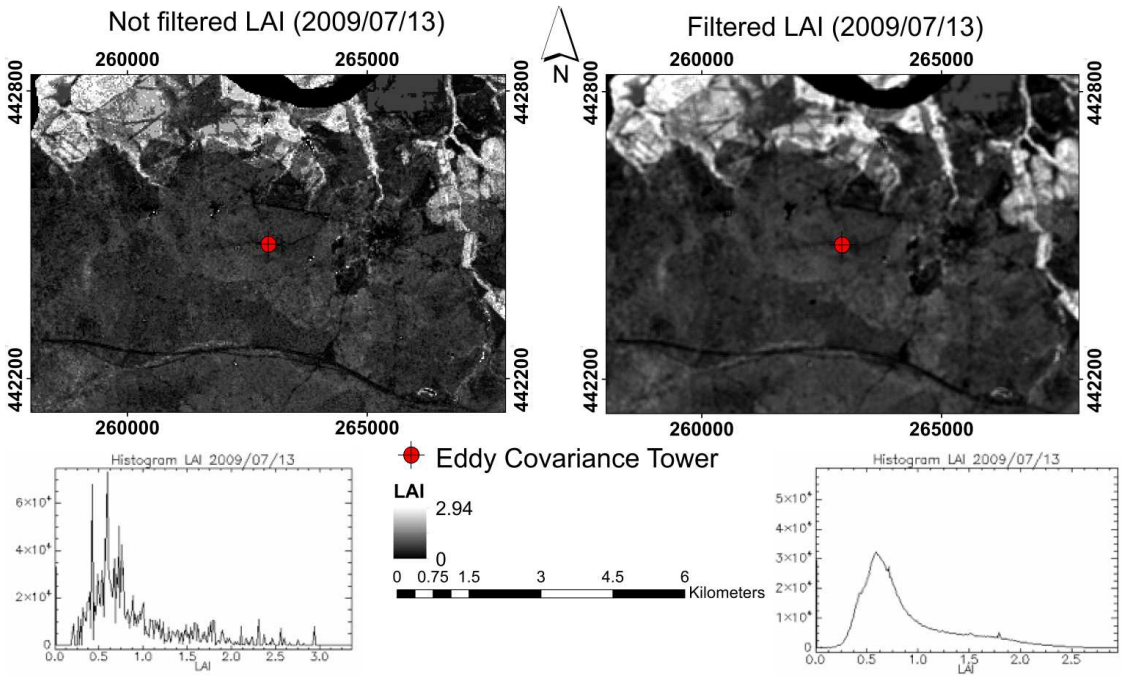


**Figure 38.** Smoothing effect of the 3x3 low pass filter.

### 5.1.3 Evaporative fraction using Landsat (Triangle method)

Taking into account the uncertainties found in LST retrieval using a single thermal band (Vlassova et al. 2014) and also the fact that the triangle method, is based on the relative position of the LST-VI pairs (Venturini et al. 2004); we decided to calculate the triangle (**Figure 4**) using Landsat brightness temperature (BT), together with the downscaled LAI. The bin step in the calculation of the edges of the triangle was configured at 0.2 and the maximum bin temperature was used to calculate the dry edge fitting line using Tang method (Tang et al. 2010) as it showed in the previous chapter that is less sensible to the presence of outliers. To calculate the wet edge the Variable Maximum Vegetation Index (Vari Max VI) method was used. This method obtains $Ts_{min}$ as the value of the dry edge that corresponds to a LAI that corresponds to those areas of full vegetation density, where transpiration is occurring at its maximum rate. In our case the maximum LAI is either the maximum LAI found in the scene or a LAI of 3.5, whichever is higher. The value of LAI=3.5 was chosen based on the maximum values observed in the study area during the field sampling campaigns (**Figure 19**).

Once the edges of the triangles were calculated for each date, the results were checked to remove those dates where the triangle was not properly defined, according to three different parameters extracted from the triangle calculation.

1) The number of pixels in the window used to calculate the edges of the triangle. Only those with at least 75% of the total possible were selected. With this decision we guarantee the comparability and temporal consistency of the data, as well as having enough pixels to calculate the edges of the triangle and removal of those dates in which cloud mask reduces the number of good quality pixels available for edge definition.

2) The $R^2$ value of the dry edge fitting line; only those dates where this value is higher than 0.9 were selected. With this criterion those dates in which the dry edge presents noise are removed leaving only those dates where the dry edge is sharp.

3) The number of points used to define the dry edge. Only those dates in which at least 10 points are used for the calculation of the dry edge were selected. Tang method removes points to improve the calculation of the dry edge based on the RMSE. This might lead to high $R^2$ values but in some cases without a large enough range of LAI values. Using those dates where at least 10 points are used for the definition will ensure the quality of the data and having representative points over the full range of LAI, as in our study case the bin step was set to 0.2. This simple quality procedure ensures the quality and representativeness of the triangles used for the estimation of $\phi$.

The $\phi$ parameter was estimated using the two step scheme proposed by Stisen et al. (2008b) that uses a non-linear interpolation rather than the linear proposed by Jiang and Islam (2001) and modified to work with LAI instead of a VI. This interpolation method first obtains the lower bound of $\phi$ for each interval of LAI between $LAI_{Max}$ ($\phi_{max}$) and $LAI_{Min}$ ($\phi_{min}$) (**Figure 4**) using the next equation

$$\phi_{i,min} = \phi_{max}\left[\frac{LAI_i - LAI_{min}}{LAI_{max} - LAI_{min}}\right]^2 \qquad \textbf{(Equation 19)}$$

As potential ET is assumed to occur for wet conditions, a fixed $\phi_{max}$ was assigned to the upper bound independently of the vegetation cover. Once the upper and lower bounds for each LAI interval are defined, we interpolate linearly within each LAI interval between the lowest and highest Ts following the next equation:

$$\phi_i = \frac{Ts_{i,max} - Ts_i}{Ts_{i,max} - Ts_{i,min}} \left(\phi_{max} - \phi_{i,min}\right) + \phi_{i,min} \qquad \textbf{(Equation 20)}$$

And $\Delta$ was calculated from the temperature at the wet edge (in °C) as in **Equation 21**. This temperature was used as a surrogate to the actual air temperature required to calculate Δ in order to avoid using ground data and assuming that $\left[\frac{\Delta}{\Delta+\gamma}\right]$ is not very sensitive to small changes of T

$$\Delta = \frac{4098 * \left[0.6108 * \exp(\frac{17.27 * T}{T + 237.3})\right]}{(T + 237.3)^2} \qquad \textbf{(Equation 21)}$$

while $\gamma$ was calculated at a fixed atmospheric pressure of 100 KPa using **Equation 22**:

$$\gamma = \frac{c_p * P}{\varepsilon\lambda} = 0.665 * 10^{-3} * P \qquad \textbf{(Equation 22)}$$

where P is the atmospheric pressure, $\varepsilon$ is the ratio molecular weight of water vapor/dry air (0.622), $c_p$ is the specific heat at constant pressure ($1.013*10^{-3}$ MJ $kg^{-1}$ $C^{-1}$) and $\lambda$ is the latent heat of vaporization (2.45 MJ $kg^{-1}$). Then EF was calculated using **Equation 3** in Section 1.3.

Finally the contributions of the footprint estimated as in Section 2.3 were used for each coincident day to compare EF Landsat estimated with those measured by the EC system during Landsat overpass. Furthermore, in order to analyze scale issues in EF estimation, we compared both the footprint aggregated Landsat EF values as well as the single pixel values over the flux tower. To validate the estimates and the different methods used to calculate EF from Landsat, we have used the EC EF as reference. Due to the small number of available Landsat scenes during the study period, a higher robustness in the estimation of the different

statistics -determination coefficient ($R^2$), Root Mean Square Error (RMSE), bias and Mean Absolute Error (MAE) - was obtained by using bootstrap with 200 repetitions.

## 5.2 Results

### 5.2.1 EF measured with the EC tower

Results of the daily and overpass EFs calculated from the EC tower is presented in **Figure 39**. EF temporal evolution exhibits lowest values during the summer, coincident with the driest and warmest period of the year in Mediterranean ecosystems. The opposite occurs in winter, where most of the rainy events occurred at the study site. The EF daily variability, expressed as the Standard Deviation (SD) (**Figure 39**), shows much higher values for daytime than the overpass EF, which barely pass above 0.2 and higher during winter time.

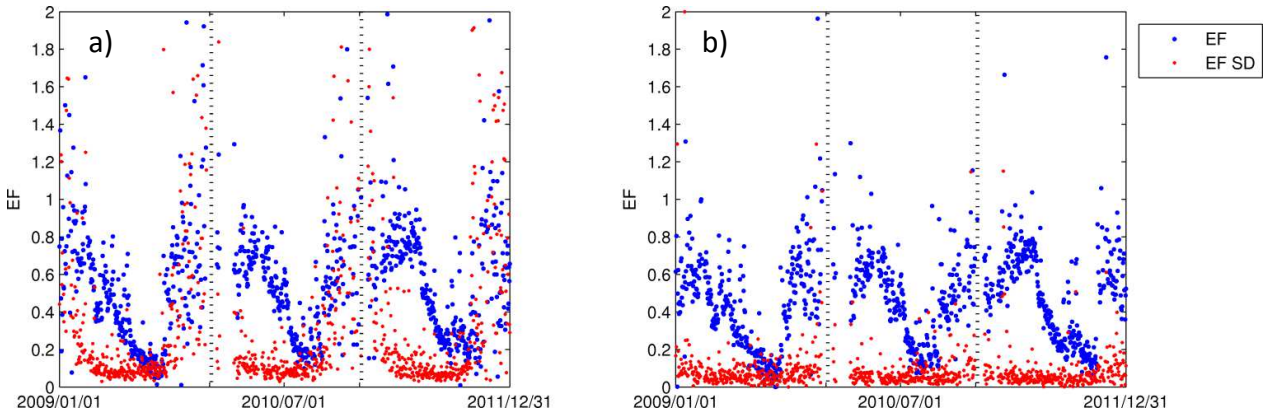


**Figure 39.** EF and SD of EF calculated from the EC system from 2009/01/01 to 2011/12/31. Left plot presents the results of daily EF values. Right plot presents the overpass EF results.

The relationship between daytime and overpass EF indicated that daytime EF shows higher values than overpass EF ($\overline{EF}_{\text{Daily}}$ = 0.52 vs $\overline{EF}_{\text{Overpass}}$ = 0.32) (**Figure 40**) which agrees with the daily EF trends described by different authors (Gentine et al. 2007; Lhomme and Elguero 1999). Correlation analysis between the two EFs

showed high agreement ($R^2$=0.960) when the SD is lower than 0.2, however when all data is included the $R^2$ drops to 0.68.

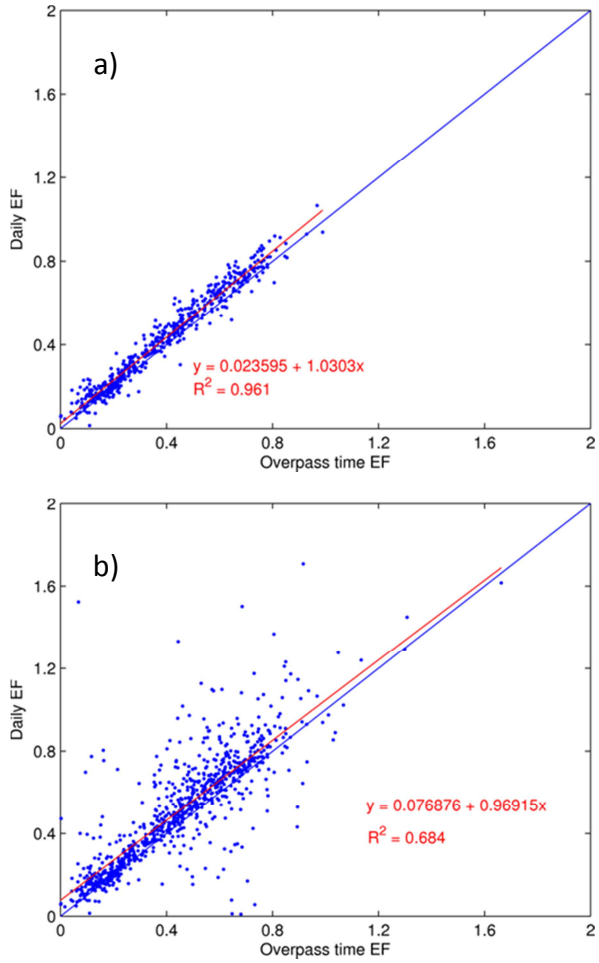


**Figure 40.** Scatterplot comparing daily EF and overpass EF. a) Image presenting the relationship with only those data where the EF SD is lower than 0.2 are plotted. b) image presenting the relationship with all the dataset.

The different footprints calculated over the study period are presented in **Figure 41**. As it can be observed, the predominant footprint direction is E-W and in most of the cases the 80% of contribution is at a distance shorter than 1 km, except for the date 2011/05/08 where the footprint covered a much larger area due to stability conditions. However, due to the presence of sparse trees in the area, the footprint calculation is challenging and this footprint has to be considered an approximation of the actual footprint, likely with a more irregular shape.

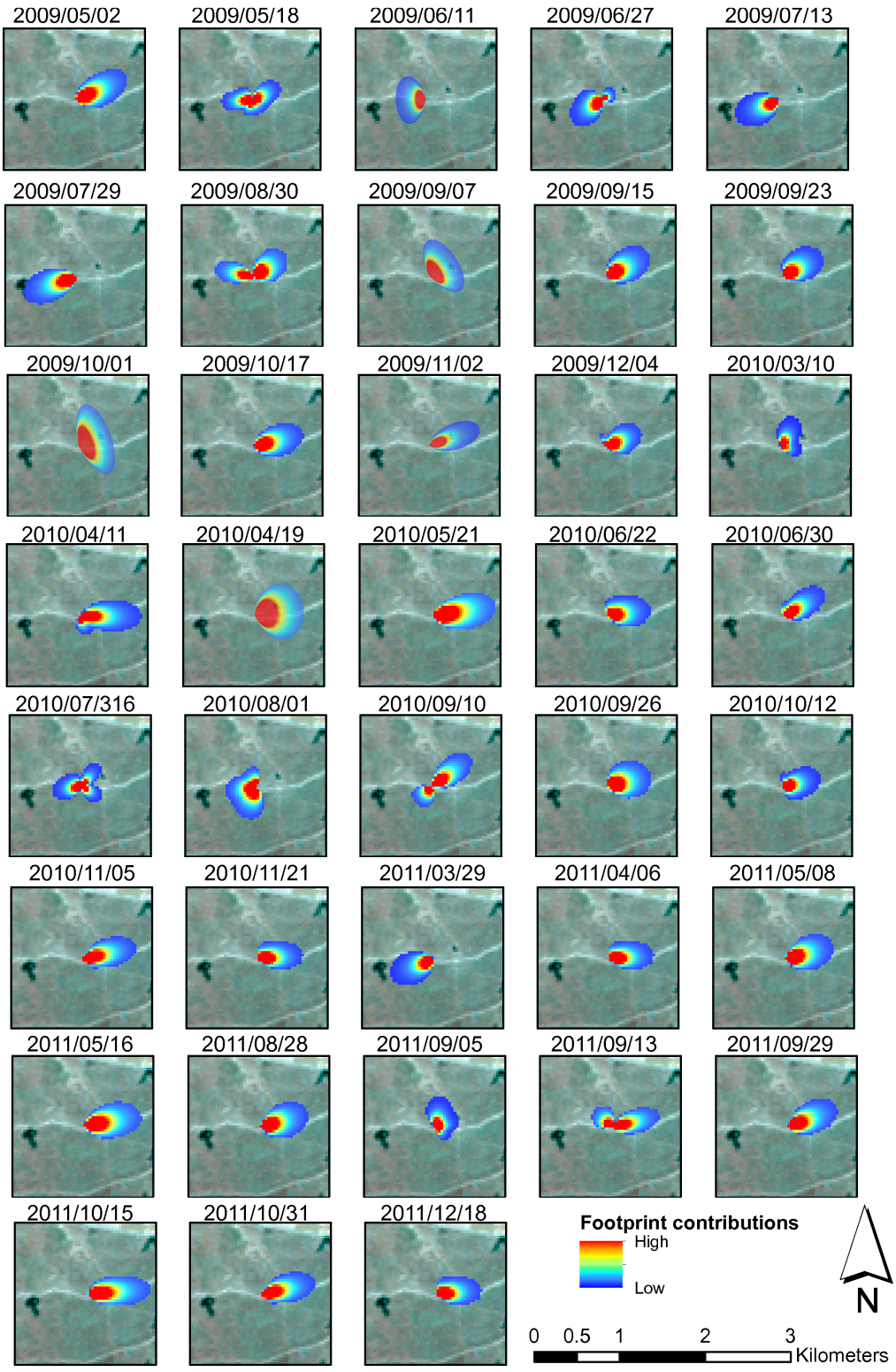


**Figure 41.** Calculated footprints centered at the EC flux tower using data within the overpass temporal window data. Background image corresponds to a Landsat 5 TM false color composite over the study area. .

Once the footprint was calculated we plotted the hourly temporal evolution of EF and Rn for the coincident dates (**Figure 42**) to better understand these differences. In our study case the typical U shape of EF (Gentine et al. 2007; Lhomme and Elguero 1999; Peng et al. 2013) is not recognizable in most of the cases; only in 2011/11/06 this pattern is clearly observable. On the other hand a rapid increase in the EF in the afternoon is clearer over the wet period (2009/09/23, 2009/11/02 or 2009/12/04 among others). During the dry periods the daily EF values showed very low variation causing a flat pattern and, therefore, low EF SD values.

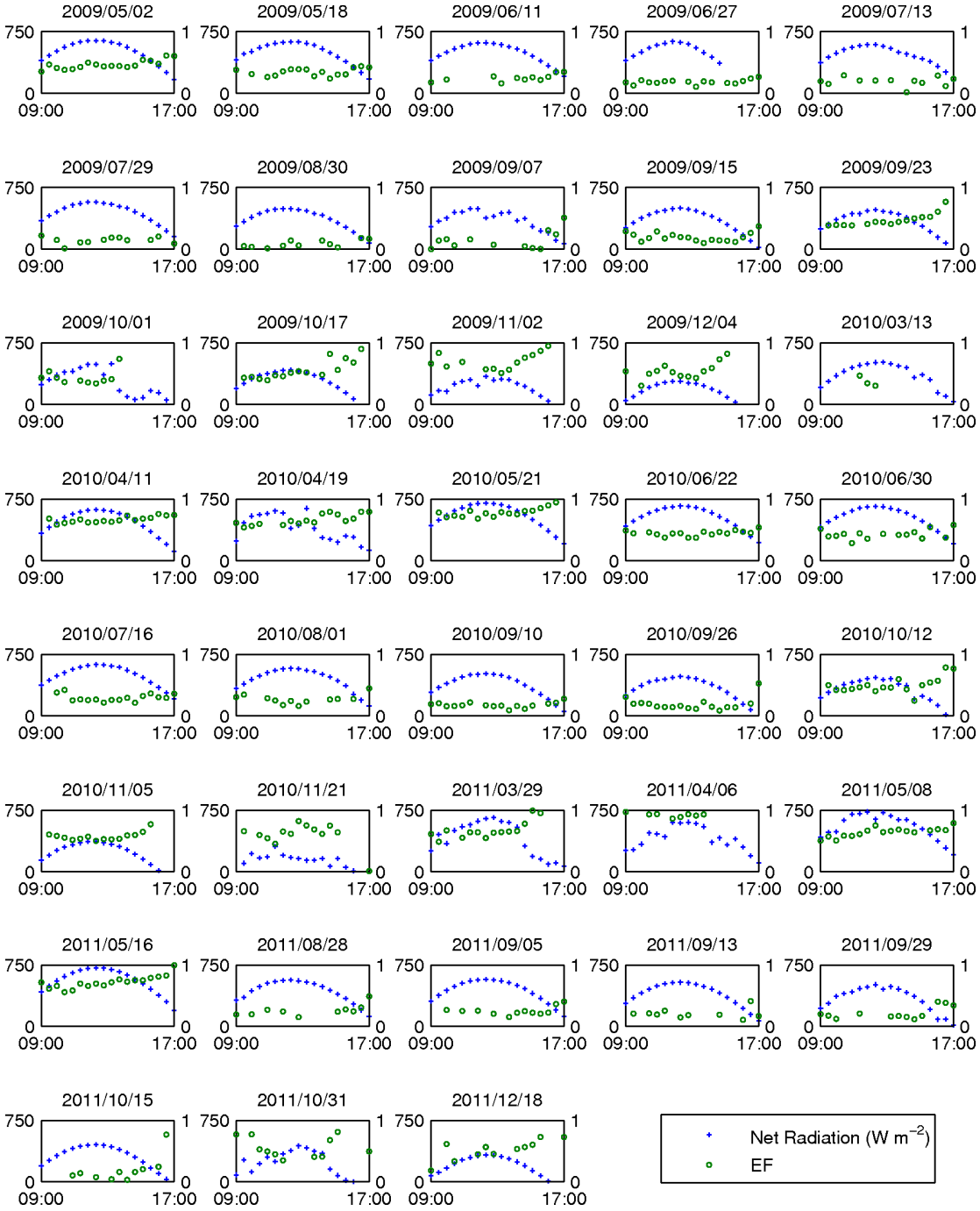


**Figure 42.** EF intra-day variations and Net Radiation for those days where the footprint was calculated.

### 5.2.2. EF calculated from Landsat

**Table 9** summarizes the results obtained for those dates corresponding to Landsat overpass. It includes parameters related to the wet/dry edges calculations, and the EF obtained from the EC tower and the Landsat estimates. As it can be observed there are some missing values due to erroneous data in the EC system, which made impossible either calculating the footprint contributions or the EF, or in other cases due to the Landsat 7 ETM+ stripes falling within the EC tower location. From the 45 dates originally selected for the study, a total of 18 dates were removed based on the criteria defined in Section 5.1.3, leaving a maximum of 27 usable scenes. The scenes removed corresponded mainly to rainy and cloudy periods. Another 5 dates with low quality or no data measured by the EC tower were removed leaving a total of 22 dates for the validation process (out of the 45 cloud-free scenes that were originally processed).

**Table 9.** Summary table presenting the results obtained from Landsat to calculate EF. Data in italic data corresponds to those selected dates after applying the filter to select the best dates. Bold data highlighted the dates used for validation. Dry edge Intercept indicates the value where the line intercepts the y axis. Dry edge slope shows the value of the slope of the dry edge. Wet edge value presents the intercept of the wet edge with the y axis. The dry edge points indicates the number of points used for the calculation of the dry edge and the % Points shows the percentage of points used for the edges calculation from the total possible in the window. EF presents the value of the evaporative fraction measured by the eddy covariance tower presenting the standard deviation value (EF SD) or either the EF value obtained with Landsat for the footprint (EF footprint) or from the pixel over the EC tower(EF pixel).

| Date | *Triangle information* | | | | | | Eddy Covariance | | | | Landsat EF | |
|---|---|---|---|---|---|---|---|---|---|---|---|---|
| | | | | | | | Daily | | Overpass | | | |
| | *Dry Edge Intercept* | *Dry Edge Slope* | *Wet Edge value* | *$R^2$* | *Dry Edge Points* | *% Points* | EF | EF SD | EF | EF SD | EF Footprint | EF Pixel |
| *2009-03-31* | *44.04* | *-6.69* | *26.36* | *0.99* | *11.00* | *77.04* | - | - | - | - | - | *0.36* |
| ***2009-05-02*** | ***39.45*** | ***-5.07*** | ***25.88*** | ***0.91*** | ***11.00*** | ***83.73*** | ***0.46*** | ***0.07*** | ***0.43*** | ***0.04*** | ***0.42*** | ***0.36*** |
| ***2009-05-18*** | ***45.92*** | ***-7.82*** | ***25.07*** | ***0.99*** | ***11.00*** | ***84.00*** | ***0.34*** | ***0.06*** | ***0.32*** | ***0.05*** | ***0.30*** | ***0.32*** |

| | | | | | | | | | | | | |
|---|---|---|---|---|---|---|---|---|---|---|---|---|
| ***2009-06-11*** | ***47.41*** | ***-6.76*** | ***28.53*** | ***0.99*** | ***10.00*** | ***95.31*** | ***0.25*** | ***0.06*** | ***0.22*** | ***-*** | ***0.24*** | ***0.24*** |
| ***2009-06-27*** | ***46.98*** | ***-7.91*** | ***27.40*** | ***0.97*** | ***10.00*** | ***95.35*** | ***0.18*** | ***0.04*** | ***0.19*** | ***0.02*** | ***0.32*** | ***0.35*** |
| ***2009-07-13*** | ***43.70*** | ***-5.33*** | ***29.62*** | ***0.98*** | ***10.00*** | ***95.33*** | ***0.16*** | ***0.10*** | ***0.17*** | ***0.14*** | ***0.26*** | ***0.26*** |
| ***2009-07-29*** | ***51.95*** | ***-7.68*** | ***30.81*** | ***0.95*** | ***11.00*** | ***95.36*** | ***0.14*** | ***0.06*** | ***0.09*** | ***0.06*** | ***0.32*** | ***0.34*** |
| ***2009-08-30*** | ***43.21*** | ***-4.79*** | ***27.10*** | ***0.95*** | ***14.00*** | ***95.39*** | ***0.05*** | ***0.10*** | ***0.06*** | ***0.06*** | ***0.19*** | ***0.21*** |
| *2009-09-07* | *35.04* | *-3.24* | *24.14* | *0.99* | *10.00* | *82.51* | - | - | - | - | *1.74* | *1.93* |
| ***2009-09-15*** | ***34.28*** | ***-4.22*** | ***20.08*** | ***0.99*** | ***13.00*** | ***95.40*** | ***0.19*** | ***0.07*** | ***0.20*** | ***0.06*** | ***0.30*** | ***0.30*** |
| 2009-09-23 | 33.93 | -3.44 | 22.37 | 0.88 | 14.00 | 83.30 | 0.52 | 0.22 | 0.40 | 0.02 | 0.48 | 0.49 |
| 2009-10-01 | 27.09 | -2.54 | 18.56 | 0.89 | 14.00 | 91.15 | - | - | - | - | 1.75 | 1.93 |
| ***2009-10-17*** | ***30.42*** | ***-4.40*** | ***15.65*** | ***0.98*** | ***12.00*** | ***95.39*** | ***0.61*** | ***0.26*** | ***0.45*** | ***0.04*** | ***0.56*** | ***0.55*** |
| 2009-11-02 | 23.89 | -3.95 | 13.52 | 0.99 | 10.00 | 70.64 | 0.50 | 0.56 | 0.49 | 0.11 | 1.70 | 1.93 |
| 2009-12-04 | 17.55 | -3.47 | 6.60 | 0.80 | 9.00 | 94.86 | - | - | - | - | 0.67 | 0.67 |
| 2010-02-06 | 18.59 | -2.76 | 10.54 | 0.98 | 6.00 | 95.13 | - | - | - | - | - | 0.92 |
| 2010-03-10 | 16.51 | -1.39 | 12.79 | 0.88 | 9.00 | 95.05 | 0.37 | 0.09 | 0.37 | 0.09 | 2.07 | 2.09 |
| ***2010-04-11*** | ***33.88*** | ***-4.68*** | ***21.38*** | ***0.99*** | ***10.00*** | ***95.29*** | ***0.67*** | ***0.05*** | ***0.62*** | ***0.03*** | ***1.10*** | ***1.13*** |
| 2010-04-19 | 24.26 | -1.08 | 21.34 | 0.91 | 11.00 | 69.65 | - | - | - | - | 1.73 | 1.93 |
| *2010-05-05* | *36.68* | *-5.30* | *21.59* | *0.98* | *10.00* | *82.75* | - | - | - | - | - | *0.84* |
| ***2010-05-21*** | ***44.07*** | ***-6.62*** | ***26.56*** | ***0.99*** | ***11.00*** | ***81.77*** | ***0.80*** | ***0.09*** | ***0.73*** | ***0.05*** | ***0.64*** | ***0.64*** |
| ***2010-06-22*** | ***51.61*** | ***-8.63*** | ***28.62*** | ***0.98*** | ***11.00*** | ***81.59*** | ***0.45*** | ***0.04*** | ***0.43*** | ***0.03*** | ***0.44*** | ***0.41*** |
| ***2010-06-30*** | ***42.74*** | ***-6.12*** | ***26.81*** | ***0.99*** | ***11.00*** | ***95.31*** | ***0.43*** | ***0.08*** | ***0.38*** | ***0.07*** | ***0.26*** | ***0.26*** |
| ***2010-07-16*** | ***49.06*** | ***-7.06*** | ***30.69*** | ***0.99*** | ***10.00*** | ***95.31*** | ***0.29*** | ***0.06*** | ***0.31*** | ***0.07*** | ***0.28*** | ***0.31*** |
| ***2010-08-01*** | ***47.17*** | ***-6.51*** | ***25.29*** | ***0.99*** | ***13.00*** | ***95.34*** | ***0.27*** | ***0.08*** | ***0.24*** | ***0.05*** | ***0.17*** | ***0.16*** |
| ***2010-09-10*** | ***40.22*** | ***-5.07*** | ***23.19*** | ***0.94*** | ***14.00*** | ***82.95*** | ***0.18*** | ***0.04*** | ***0.18*** | ***0.03*** | ***0.21*** | ***0.23*** |
| ***2010-09-26*** | ***33.77*** | ***-4.02*** | ***20.25*** | ***0.92*** | ***14.00*** | ***83.36*** | ***0.17*** | ***0.12*** | ***0.17*** | ***0.03*** | ***0.27*** | ***0.29*** |
| ***2010-10-12*** | ***24.10*** | ***-1.94*** | ***17.59*** | ***0.98*** | ***13.00*** | ***81.34*** | ***0.50*** | ***0.13*** | ***0.44*** | ***0.04*** | ***0.59*** | ***0.61*** |
| 2010-11-05 | 22.69 | -2.19 | 16.97 | 0.95 | 8.00 | 95.30 | 0.86 | 0.83 | 0.54 | 0.03 | 1.12 | 1.20 |
| 2010-11-21 | 13.91 | -1.13 | 10.88 | 0.90 | 10.00 | 38.01 | - | - | - | - | 1.69 | 1.93 |
| 2011-01-24 | 12.84 | -3.24 | 4.42 | 0.95 | 7.00 | 94.64 | 0.85 | 1.80 | 0.70 | 0.04 | | 1.33 |
| 2011-02-01 | 11.43 | -1.08 | 8.62 | 0.50 | 11.00 | 80.07 | 0.84 | 1.14 | 0.45 | 0.11 | - | - |
| *2011-02-09* | *13.14* | *-2.09* | *7.60* | *0.94* | *11.00* | *92.78* | *0.47* | *0.39* | - | - | - | *1.54* |
| 2011-02-25 | 19.54 | -0.73 | 17.56 | 0.54 | 10.00 | 95.06 | 0.81 | 0.32 | 0.56 | 0.16 | - | 2.83 |
| 2011-03-29 | 20.09 | -0.61 | 18.49 | 0.85 | 10.00 | 92.79 | - | - | - | - | 1.83 | 1.93 |
| 2011-04-06 | 23.37 | -2.57 | 16.58 | 0.98 | 9.00 | 32.76 | - | - | - | - | 1.90 | 1.93 |
| 2011-05-08 | 36.20 | -5.77 | 20.95 | 0.94 | 11.00 | 59.19 | - | - | - | - | - | 1.38 |
| 2011-05-16 | 36.48 | -5.10 | 23.12 | 1.00 | 9.00 | 95.37 | 0.72 | 0.10 | 0.64 | 0.06 | 0.76 | 0.74 |
| ***2011-08-28*** | ***42.45*** | ***-5.23*** | ***24.87*** | ***0.96*** | ***15.00*** | ***82.24*** | ***0.26*** | ***0.09*** | ***0.23*** | ***0.04*** | ***0.16*** | ***0.18*** |
| ***2011-09-05*** | ***35.41*** | ***-3.49*** | ***23.67*** | ***0.95*** | ***14.00*** | ***95.29*** | ***0.25*** | ***0.07*** | ***0.26*** | ***0.01*** | ***0.27*** | ***0.28*** |
| *2011-09-13* | *40.89* | *-4.35* | *26.26* | *0.96* | *14.00* | *82.08* | *0.21* | *0.08* | *0.20* | *0.05* | *0.23* | - |
| ***2011-09-29*** | ***33.14*** | ***-4.82*** | ***20.39*** | ***0.97*** | ***12.00*** | ***82.65*** | ***0.21*** | ***0.10*** | ***0.16*** | ***0.06*** | ***0.20*** | ***0.23*** |
| ***2011-10-15*** | ***32.85*** | ***-4.08*** | ***19.98*** | ***0.92*** | ***13.00*** | ***81.33*** | ***0.13*** | ***0.21*** | ***0.08*** | ***0.06*** | ***0.32*** | ***0.37*** |
| 2011-10-31 | 13.38 | -1.12 | 12.39 | 1.00 | 2.00 | 0.68 | - | - | - | - | 1.74 | 1.93 |
| 2011-12-18 | 12.08 | -1.26 | 8.92 | 0.66 | 10.00 | 81.88 | 0.57 | 1.51 | 0.49 | 0.12 | 1.71 | 1.93 |

**Figure 43** shows the timeseries of EF, both the observed from EC and the predicted from Landsat. As guessed, there is much more available data during the spring and summer seasons than for winter and autumn, and EF follows the expected trend for the Mediterranean ecosystems with high EF values just after the cold and wet season where the vegetation is green and soil is wet, and very low EF values during the dry and warm period where the soil becomes dry and the vegetation cures (**Figure 43**).

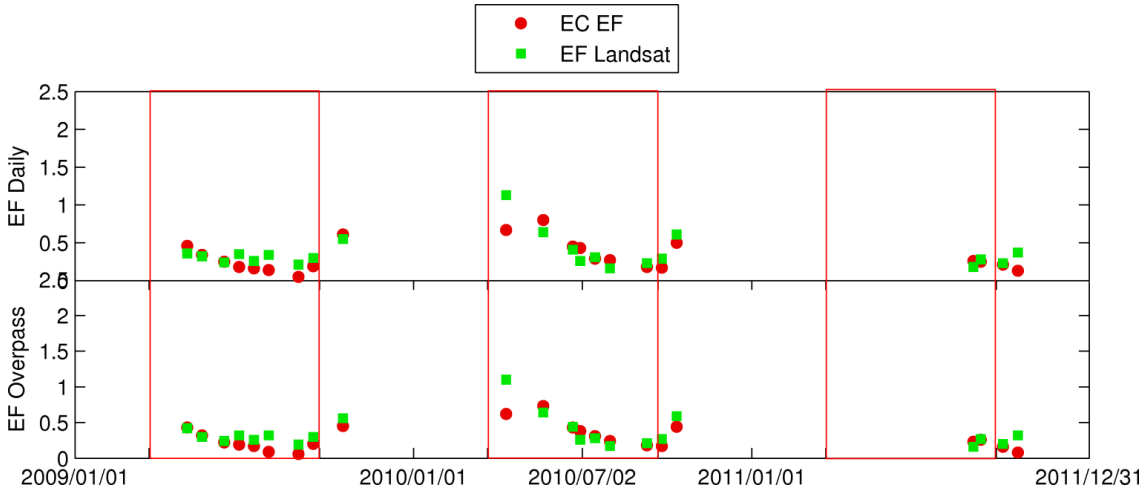


**Figure 43.** EF observed (EC) and estimated (Landsat) for the whole study period. Red boxes indicate the periods corresponding to the Spring and Summer were the rainy events are less frequent.

The comparison between the calculated EF from Landsat and the reference EF from the EC using footprint contributions and the pixel is presented in **Figure 44** and bootstrap statistics are presented in **Table 10**. Higher agreement between Landsat and measured EF is observed when the comparison is carried out using the overpass data. Results indicated very similar statistics in case of using the footprint data or the pixel value although the latter one presents slightly better statistics. Daily EF presented the lower $R^2$ value ($R^2$=0.583) of all compared methods and highest $R^2$ was found for the overpass EF when compared with the tower pixel value ($R^2$=0.645). On the other hand other error statistics like MAE (MAE or RMSE) showed slightly better results when daily data are used.

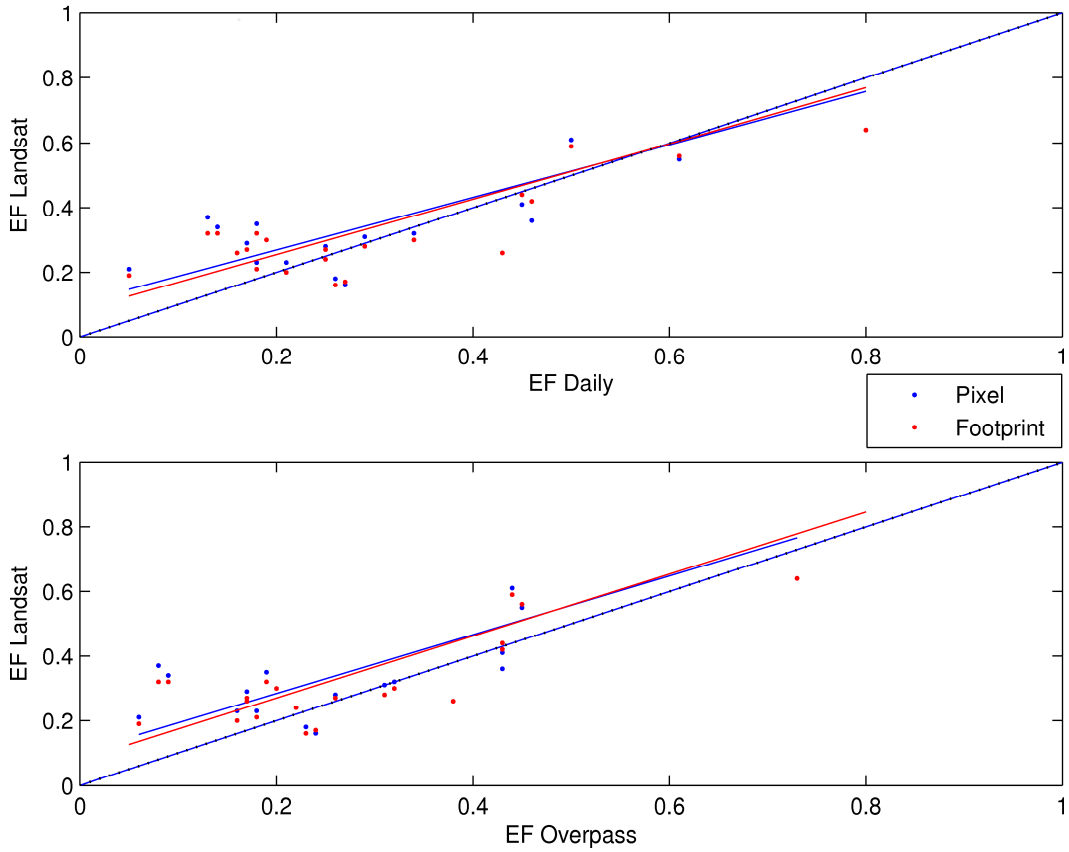


**Figure 44.** Observed vs. predicted relationships between reference daily EF value or overpass EF measured with the EC versus the EF calculated from Landsat. Blue dots represent the Landsat pixel value at the EC tower, while red dots represent the aggregated Landsat values at the footprint scale.

**Table 10.** Validation statistics of EF estimated using Landsat compared with the EC measurements using bootstrap with 200 repetitions.

| **Footprint** | **RMSE** | **RMSE SD** | **$R^2$** | **$R^2$ SD** | **Bias** | **Bias SD** | **MAE** | **MAE SD** |
|---|---|---|---|---|---|---|---|---|
| **Daily EF** | 0.153 | 0.031 | 0.583 | 0.128 | 0.043 | 0.031 | 0.116 | 0.018 |
| **Overpass EF** | 0.141 | 0.036 | 0.638 | 0.125 | 0.061 | 0.028 | 0.104 | 0.021 |
| **Pixel** | **RMSE** | **RMSE SD** | **$R^2$** | **$R^2$ SD** | **Bias** | **Bias SD** | **MAE** | **MAE SD** |
| **Daily EF** | 0.145 | 0.035 | 0.633 | 0.114 | 0.065 | 0.029 | 0.103 | 0.022 |
| **Overpass EF** | 0.142 | 0.034 | 0.645 | 0.118 | 0.068 | 0.028 | 0.104 | 0.021 |

## 5.3. Discussion

The results of the EF measured by the EC system showed that the assumption of EF daily preservation in this ecosystem cannot be guaranteed. This is an important finding, as this assumption can lead to large errors in daily ET estimates (Crago and Brutsaert 1996; Gentine et al. 2007; Lhomme and Elguero 1999; Peng et al. 2013). Several studies have already mentioned that the assumption of constant EF during daytime hours is valid under clear skies and constant weather forcing conditions (Crago and Brutsaert 1996; Shuttleworth et al. 1989). In this study we have shown that daily EF fluctuates during the day using the SD as an indicator of this variation. Higher SD values were observed during autumn and winter coincident with the rainy periods at the study site and therefore more prone to changing weather forcing conditions (**Figure 39**a). In the case of the overpass EF this EF fluctuation was much smaller, first as a consequence of using a smaller number of measurements (5 against 17), and second due to the time window used, which contains less variable data under constant weather forcing conditions (**Figure 36**). The comparison between daily EF and overpass EF using the data from the EC are in agreement with the results found by Peng et al. (2013) where $R^2$ close to 1 was found under clear sky conditions for grasslands and savannas at 11:00 UTC. When we eliminated those values with a SD higher than 0.2 we found an increase in $R^2$ resulting in values up to 0.96 (**Figure 40**). The authors also observed a decrease in the $R^2$ under cloudy sky conditions, and in our case when all data is used the $R^2$ decreased down to 0.68 (**Figure 40**).

A more detailed study of those days coincident with Landsat overpass revealed interesting features. Different diurnal behaviors where observed depending on the season. In summer very low daily EF variation was observed (**Figure 42**) while in spring and autumn the diurnal trends of EF presented a rather constant evolution until noon but then EF increased in the afternoon. In winter the EF presented an inverted U diurnal shape reaching higher EF values in the afternoon. Following the findings of Gentine et al. (2007) we could explain these differences in the EF evolution during the year. The authors showed that soil EF

($EF_S$) presented very low variation during the day, especially when low LAI values occur. In our study site, the grassland layer in summer becomes cured with very low LAI values and, therefore, we also expect that the EF measured by the EC system is mostly controlled by $EF_S$. The opposite happens during spring or autumn, where the constant values during the morning and the rapid increase in the afternoon suggest that the EF is mainly controlled by canopy EF ($EF_C$) (**Figure 45**). Finally, in winter the diurnal evolution suggest a combination of both $EF=EF_S+EF_C$ coincident with the period were both vegetation and soil are not water limited.

These differences in the shape indicate a much larger difference between the EF calculated during the sensor overpass time and the daily EF, especially in winter, which could lead to larger errors in the daily ET estimates (Crago and Brutsaert 1996; Gentine et al. 2007; Lhomme and Elguero 1999; Peng et al. 2013) in this type of climate and ecosystem. On the other hand these differences between daily and overpass estimates are much lower during spring and summer, and therefore allowing the retrieval of ET using the EF self-preservation more accurately.

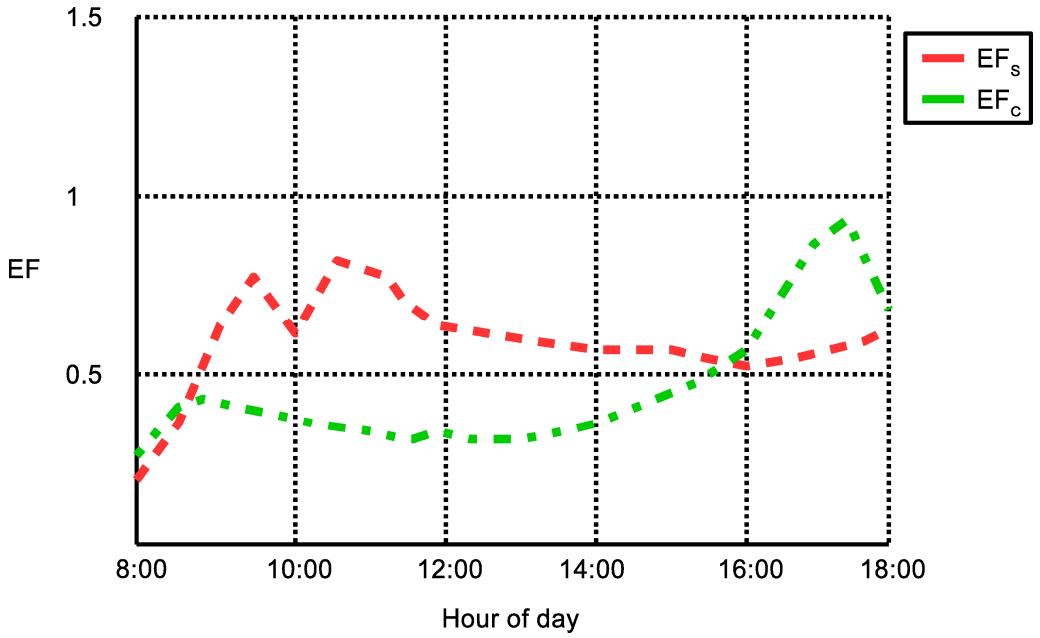


**Figure 45.** Modeled $EF_C$ and $EF_S$ for LAI value of 2.5. Modified after Gentine et al. (2007).

The modified triangle approach using the LAI instead of a VI showed good results. The substitution of the VI offered some advantages. Firstly, LAI is a biophysical parameter which provides to the interpretation of the triangle a more physical meaning and helps in the calculation of the edges as it removes the effect of saturation of VI for very dense canopies (de Tomás et al. 2014). The Vari Max VI method used to define the wet edge guaranteed that the minimum temperature calculation is based on the areas with most dense vegetation. In this study the LAI was downscaled from MODIS LAI resolution (1 km) to Landsat resolution (30 m) using a trained regression tree algorithm. Results strongly depend on how the training stage is carried out. In our study case a total of 45 Landsat scenes were used and a total of 14 LAI classes were defined in the training stage. Though usually application of filters is not recommended as they modified the pixel value, in our case this was preferred to reduce the noise of the Landsat resolution LAI outputs and remove most of the spikes present in the histogram (**Figure 46**).

MODIS LAI product has been already validated ensuring the quality of the product (McColl et al. 2011; Weiss et al. 2007). Most of this validation have been carried out over homogenous areas, however, recently a study validated the quality of this product over the study area (Durá et al. 2013) showing that although there are some problems with the LAI estimation in this type of ecosystem, the use of a product that combines Terra and Aqua (MCD15) reduced the errors in LAI estimates.

**Figure 46.** Histograms showing the effect of applying the low pass filter effect on LAI.

Only those dates in which the definition of the edges of the triangle was properly calculated were used in the analysis. One of the weaknesses of the triangle method is that often requires a qualitative visual check of the triangles and the edge definition. This reduces the applicability of the method making it less operational and increases the uncertainties of the results. In our study the selection was carried out using an simple automatic criteria based on the triangle statistics obtained for each date, just based on the window size and the number of pixels. This process makes the triangle technique more operational and robust when dealing with long time series as automatically removes those dates subject to errors due to a poor definition of the triangle space. Many studies applied the triangle technique to calculate EF (de Tomás et al. 2014; Garcia et al. 2014; Sandholt et al. 2002; Stisen et al. 2008b; Venturini et al. 2004; Venturini et al. 2008; Wang et al. 2006b), however, in these studies it is not fully clear the criteria used to select the usable data, and how the filtering of the data was performed

Estimates of EF using Landsat were compared in this study to daily and overpass EF using bootstrap techniques. The results of this comparison presented

better statistics when using overpass EF rather than daily EF (**Table 10**) which was expected as these values are closer in time and therefore the chances of varying weather conditions that could introduce noisy data is smaller. On the other hand the differences in the performing statistics are not that large. We hypothesize that this is a consequence of the method used to retrieve EF from Landsat. As it was previously mentioned in the discussion, in this study we selected the best data based on the triangle statistics. This method removed most of the days in the rainy periods, in which the triangle method showed some problems. In addition most of the dates selected for this study are coincident with those in which the EF presented very low daily variation and consequently, daily and overpass EF are very similar (Peng et al. 2013). We expect that a larger temporal dataset covering a larger range of EF would have resulted in larger differences between daily and overpass EF; however, this statement needs to be confirmed in future studies increasing the Landsat time series with the new Landsat 8 sensor.

The methodology used in this study using the footprint contributions to first get a EF value from Landsat and later compare it with the EC EF measurements ensures the spatial comparability of the data and, to our knowledge, this type of comparison has not been carried out to validate EF estimates though it was done in the case of ET (Guzinski et al. 2014). In our study EF showed small differences between pixel and footprint values. As mentioned on section 2.3 and showed on **Figure 41**, the largest footprint contributions are within the area nearby the EC. On the other hand, we used Landsat 7 that presents a striping problem that leads to some unusable date. We fixed this issue by using only the pixels free of problems as contributors of the total footprint. This solution seemed to work well as the EF in the ecosystem is very homogeneous.

Recent studies have used a very similar approach to calculate EF to the one used in this study (de Tomás et al. 2014) using scintillometer field data for EF validation and over a cropland. The results for Landsat differ slightly from the ones presented here, they obtained slightly higher $R^2$ ($R^2$= 0.77). In our case the validation was carried out using EC instead of scintillometer measurements.

Moreover, in their case the validation was carried for only 7 dates, whilst in our case a larger data set was used. This indicates that the methodology used in this study is fully operational for this type of ecosystem achieving similar results to those over more homogenous areas such as croplands

# 6 Conclusions

This study showed a profound analysis of water fluxes by analyzing different processes, such as water content on vegetation, soil moisture and evaporative fraction/evapotranspiration, at different spatio-temporal scales. We used SEVIRI, MODIS; Landsat and proximal remote sensing as sources of spectral and thermal information and different *in situ* measurements collected either manually, like in the case of the vegetation variables, or using different instruments that measure in continuous.

The capabilities of remote sensing platforms to retrieve different vegetation biophysical variables were shown at two different spatial scales, MODIS and proximal sensing. A complete analysis of three metrics, EWT, FMC and CWC, to measure vegetation water content at two scales was presented, followed by other variables like Dm and LAI. Regarding the temporal changes in water content metrics, it can be concluded that these changes are more critical than their spatial variation within the MODIS pixel, and more effort should be done collecting temporal variations rather than spatial variations. Differences in the estimation of the field variables from spectral data depending on the field protocol used were found with higher correlations between field measured and estimated FMC and CWC when sampling strategy consist on collecting all plants included in the sampling quadrant instead of visually selecting a representative sample from outside. This can be due to subjective decisions taken by the operator when collecting the $EWT_{Sample}$. Protocol standardization in order to make different datasets comparable should be seriously considered by the community to make different dataset comparable both spatially and temporally.

The analysis of other variables showed that, due to the high seasonal Dm variability, a constant annual value should not be used to estimate EWT from FMC in this ecosystem. Among the evaluated spectral indices of this study, VARI provided the worst results in all cases. The empirical estimators differed between sensors. Better correlations between field and spectral data were found using

MODIS than proximal sensing, probably due to differences in view angles and canopy observed. The comparison between RTM estimates and empirical methods showed that the later ones improves results obtained from RTM inversions proposed to estimate FMC (Jurdao et al. 2013) and CWC (Trombetti et al. 2008).

Regarding soil moisture estimation, we presented an evaluation of how some of the factors involved in the triangle parameterization affect the final TVDI value and the implications in the final model performance for estimating SM. NDII results overcame NDVI for SM monitoring at all soil depths. The variations in the results at different depths pointed out the importance of the viewing geometry of the sensor and spatial resolution. The Simple method showed better results than Tang for the definition of the dry edge using MODIS but Tang worked better with SEVIRI. The comparison between the methods for defining the wet edge did not show significant differences. The spatial scale of SEVIRI and its viewing geometry showed difficulties in finding pure pixels to define the edges of the triangle.

Our recommendations for future applications of the triangle method in Mediterranean climates are:

- NDII or other NIR/SWIR indices in the triangle definition is recommended instead of NDVI, as it improves the model performance to estimate SM.
- Over complex areas combining different ecosystems, high spatial resolution or mid resolution data performs better. Low viewing angle differentiates pure surfaces (bare soil and pure vegetation cover) helping to properly calculate the edges.
- The method to define the dry edge that presents less steep slopes should be used as this usually presents better results.

Further research is needed to address how the substitution of NDVI with NDII or similar indices based on SWIR data perform for different ecosystems, eg. in energy limited systems vs. water limited systems and for environments different than the Mediterranean.

In the last part of this thesis we aimed to estimate EF using the triangle method. A new triangle modification was evaluated using LAI, resulting in good EF estimates. Regarding the selection of valid triangles, a simple method was

presented which is less prone to errors and user interpretations. Furthermore, we showed that the assumption of constant daily EF values may not be valid for this type of ecosystem under certain conditions and even during clear sky days. We studied the temporal evolution of EF using and EC system showing that EF present a temporal evolution, seasonally and daily, that can lead to good results of daily ET estimates during summer but large errors during other seasons of the year. This suggests that before applying the triangle technique to retrieve daily ET the EF temporal evolution of the ecosystem should be previously understood in order to evaluate its applicability.

Finally small differences were found when instead of a single pixel all footprint contributions were calculated. However in other regions, especially if the EC tower is located close to other ecosystems, the footprint contributions should be calculated.

# 7 References

Allen, R.G., Tasumi, M., & Trezza, R. (2007). Satellite-based energy balance for mapping evapotranspiration with internalized calibration (METRIC)—Model. *Journal of irrigation and drainage engineering, 133*, 380-394

Anderson, M.C., Kustas, W.P., & Norman, J.M. (2007). Upscaling Flux Observations from Local to Continental Scales Using Thermal Remote Sensing. *Agron. J., 99*, 240-254

Anderson, M.C., Norman, J.M., Diak, G.R., Kustas, W.P., & Mecikalski, J.R. (1997). A two-source time-integrated model for estimating surface fluxes using thermal infrared remote sensing. *Remote Sensing of Environment, 60*, 195-216

Aubinet, M., & Papale, D. (2014). The ICOS Ecosystem protocol for gas concentration measurements. In, *EGU General Assembly Conference Abstracts*. Viena

Bach, H., & Mauser, W. (1994). Modelling and model verification of the spectral reflectance of soils under varying moisture conditions. In, *Geoscience and Remote Sensing Symposium, 1994. IGARSS '94. Surface and Atmospheric Remote Sensing: Technologies, Data Analysis and Interpretation., International* (pp. 2354-2356 vol.2354)

Baldocchi, D.D., Hincks, B.B., & Meyers, T.P. (1988). Measuring Biosphere-Atmosphere Exchanges of Biologically Related Gases with Micrometeorological Methods. *Ecology, 69*, 1331-1340

Baret, F., Jacquemoud, S., Guyot, G., & Leprieur, C. (1992). Modeled analysis of the biophysical nature of spectral shifts and comparison with information content of broad bands. *Remote Sensing of Environment, 41*, 133 - 142

Bastiaanssen, W.G.M., Menenti, M., Feddes, R.A., & Holtslag, A.A.M. (1998). A remote sensing surface energy balance algorithm for land (SEBAL). 1. Formulation. *Journal of Hydrology, 212–213*, 198-212

Bowyer, P., & Danson, F.M. (2004). Sensitivity of spectral reflectance to variation in live fuel moisture content at leaf and canopy level. *Remote Sensing of Environment, 92*, 297 - 308

Brutsaert, W., & Sugita, M. (1992). Application of self-preservation in the diurnal evolution of the surface energy budget to determine daily evaporation. *Journal of Geophysical Research: Atmospheres, 97*, 18377-18382

Burba, G., & Anderson, D. (2010). *A Brief Practical Guide to Eddy Covariance Flux Measurements: Principles and Workflow Examples for Scientific and Industrial Applications*. LI-COR

Carlson, T.N., Gillies, R.R., & Schmugge, T.J. (1995). An interpretation of methodologies for indirect measurement of soil water content. *Agricultural and Forest Meteorology, 77*, 191-205

Carlson, T.N., Perry, E.M., & Schmugge, T.J. (1990). Remote estimation of soil moisture availability and fractional vegetation cover for agricultural fields. *Agricultural and Forest Meteorology, 52*, 45-69

Casado, M.A., de Miguel, J.M., Sterling, A., Peco, B., Galiano, E.F., & Pineda, F.D. (1986). Production and spatial structure of Mediterranean pastures in different stages of ecological succession. *Vegetatio, 64*, 75-86

Casas, A., Riaño, D., Ustin, S.L., Dennison, P., & Salas, J. (2014). Estimation of water-related biochemical and biophysical vegetation properties using multitemporal airborne hyperspectral data and its comparison to MODIS spectral response. *Remote Sensing of Environment, 148*, 28-41

Ceccato, P., Flasse, S., Tarantola, S., Jacquemoud, S., & Grégoire, J.-M. (2001). Detecting vegetation leaf water content using reflectance in the optical domain. *Remote Sensing of Environment, 77*, 22 - 33

Ceccato, P., Gobron, N., Flasse, S., Pinty, B., & Tarantola, S. (2002). Designing a spectral index to estimate vegetation water content from remote sensing data: Part 1: Theoretical approach. *Remote Sensing of Environment, 82*, 188 - 197

Chaves, M.M., Maroco, J., #227, P., o., Pereira, J., & S., o. (2003). Understanding plant responses to drought — from genes to the whole plant. *Functional Plant Biology, 30*, 239-264

Cheng, Y.-B., Ustin, S.L., Riaño, D., & Vanderbilt, V.C. (2008). Water content estimation from hyperspectral images and MODIS indexes in Southeastern Arizona. *Remote Sensing of Environment, 112*, 363 - 374

Chuvieco, E., Aguado, I., Cocero, D., & Riaño, D. (2003). Design of an empirical index to estimate fuel moisture content from NOAA-AVHRR images in forest fire danger studies. *International Journal of Remote Sensing, 24*, 1621-1637

Chuvieco, E., Cocero, D., Riaño, D., Martin, P., Martínez-Vega, J., de la Riva, J., & Pérez, F. (2004). Combining NDVI and surface temperature for the estimation of live fuel moisture content in forest fire danger rating. *Remote Sensing of Environment, 92*, 322 - 331

Chuvieco, E., Wagtendok, J., Riaño, D., Yebra, M., & Ustin, S. (2009). Estimation of fuel conditions for fire danger assessment. *Earth observation of wildland fires in Mediterranean ecosystems, Springer, Berlin Heidelberg* (pp. 83-96)

Crago, R., & Brutsaert, W. (1996). Daytime evaporation and the self-preservation of the evaporative fraction and the Bowen ratio. *Journal of Hydrology, 178*, 241-255

Danson, F., Steven, M.D., Malthus, T.J., & Clark, J.A. (1992). High-spectral resolution data for determining leaf water content. *International Journal of Remote Sensing, 13*, 461-470

Datt, B. (1999). Remote sensing of water content in Eucalyptus leaves. *Australian Journal of Botany, 47*, 909-923

Dawson, T.E., & Ehleringer, J.R. (1991). Streamside trees that do not use stream water. *Nature, 350*, 335-337

de Tomás, A., Nieto, H., Guzinski, R., Salas, J., Sandholt, I., & Berliner, P. (2014). Validation and scale dependencies of the triangle method for the evaporative fraction estimation over heterogeneous areas. *Remote Sensing of Environment, 152*, 493-511

Desbois, N., Deshayes, M., & Beudin, A. (1997). *A Review of Remote Sensing Methods for the Study of Large Wildland Fires*. Protocol for fuel moisture content measurements

Detto, M., Montaldo, N., Albertson, J.D., Mancini, M., & Katul, G. (2006). Soil moisture and vegetation controls on evapotranspiration in a heterogeneous Mediterranean ecosystem on Sardinia, Italy. *Water Resources Research, 42*, W08419

Durá, E., Mendiguren, G., Pacheco-Labrador, J., Martín, M.P., Riaño, D., Iturrate, M., Gimeno, C., & Carrara, A. (2013). Validación de productos MODIS relacionados con la estimación de flujos de carbono en un ecosistema de dehesa. *Geofocus, 13-1*, 291-310

Efron, B., & Gong, G. (1983). A Leisurely Look at the Bootstrap, the Jackknife, and Cross-Validation. *The American Statistician, 37*, 36-48

Eichinger, W.E., Parlange, M.B., & Stricker, H. (1996). On the Concept of Equilibrium Evaporation and the Value of the Priestley-Taylor Coefficient. *Water Resources Research, 32*, 161-164

Foken, T., Göockede, M., Mauder, M., Mahrt, L., Amiro, B., & Munger, W. (2005). Post-Field Data Quality Control. In X. Lee, W. Massman, & B. Law (Eds.), *Handbook of Micrometeorology* (pp. 181-208): Springer Netherlands

Gamon, J.A., Field, C.B., Roberts, D.A., Ustin, S.L., & Valentini, R. (1993). Functional patterns in an annual grassland during an AVIRIS overflight. *Remote Sensing of Environment, 44*, 239-253

Gao, B.-c. (1996). NDWI A normalized difference water index for remote sensing of vegetation liquid water from space. *Remote Sensing of Environment, 58*, 257 - 266

Gao, F., Anderson, M.C., Kustas, W.P., & Wang, Y. (2012). Simple method for retrieving leaf area index from Landsat using MODIS leaf area index products as reference. *Journal of Applied Remote Sensing, 6*, 063554-063551-063554-063515

García, M., Chuvieco, E., Nieto, H.e., ctor, & Aguado, I. (2008). Combining AVHRR and meteorological data for estimating live fuel moisture content. *Remote Sensing of Environment, 112*, 3618 - 3627

Garcia, M., Fernández, N., Villagarcía, L., Domingo, F., Puigdefábregas, J., & Sandholt, I. (2014). Accuracy of the Temperature–Vegetation Dryness Index using MODIS under water-limited vs. energy-limited evapotranspiration conditions. *Remote Sensing of Environment, 149*, 100-117

Gentine, P., Entekhabi, D., Chehbouni, A., Boulet, G., & Duchemin, B. (2007). Analysis of evaporative fraction diurnal behaviour. *Agricultural and Forest Meteorology, 143*, 13-29

Gentine, P., Entekhabi, D., & Polcher, J. (2011). The Diurnal Behavior of Evaporative Fraction in the Soil–Vegetation–Atmospheric Boundary Layer Continuum. *Journal of Hydrometeorology, 12*, 1530-1546

Gitelson, A.A., Kaufman, Y.J., Stark, R., & Rundquist, D. (2002a). Novel algorithms for remote estimation of vegetation fraction. *Remote Sensing of Environment, 80*, 76-87

Gitelson, A.A., Stark, R., Grits, U., Rundquist, D., Kaufman, Y., & Derry, D. (2002b). Vegetation and soil lines in visible spectral space: A concept and technique for remote estimation of vegetation fraction. *International Journal of Remote Sensing, 23*, 2537-2562

Goetz, S.J. (1997). Multi-sensor analysis of NDVI, surface temperature and biophysical variables at a mixed grassland site. *International Journal of Remote Sensing, 18*, 71-94

Green, R.O., Conel, J.E., & Roberts, D.A. (1993). Estimation of aerosol optical depth, pressure elevation, water vapor, and calculation of apparent surface reflectance from radiance measured by the airborne visible/infrared imaging spectrometer (AVIRIS) using a radiative transfer code. In (pp. 2-11)

Guzinski, R., Anderson, M.C., Kustas, W.P., Nieto, H., & Sandholt, I. (2013). Using a thermal-based two source energy balance model with time-differencing to estimate surface energy fluxes with day-night MODIS observations. *Hydrology and Earth System Sciences, 17*, 2809-2825

Guzinski, R., Nieto, H., Jensen, R., & Mendiguren, G. (2014). Remotely sensed land-surface energy fluxes at sub-field scale in heterogeneous agricultural landscape and coniferous plantation. *Biogeosciences Discuss., 11*, 4857-4908

Haenel, H.D., & Grünhage, L. (1999). Footprint Analysis: A Closed Analytical Solution Based On Height-Dependent Profiles Of Wind Speed And Eddy Viscosity. *Boundary-Layer Meteorology, 93*, 395-409

Hardisky, M.A., Klemas, V., & Smart, R.M. (1983). The influence of soil salinity, growth form, and leaf moisture on the spectral radiance of Spartina alterniflora canopies. *Photogrammetric Engineering & Remote Sensing, 49*, 77-83

Hassan, Q., Bourque, C., Meng, F.-R., & Cox, R. (2007). A Wetness Index Using Terrain-Corrected Surface Temperature and Normalized Difference Vegetation Index Derived from Standard MODIS Products: An Evaluation of Its Use in a Humid Forest-Dominated Region of Eastern Canada. *Sensors, 7*, 2028-2048

He, Y., Guo, X., & Wilmshurst, J.F. (2007). Comparison of different methods for measuring leaf area index in a mixed grassland. *Canadian Journal of Plant Science, 87*, 803-813

Holzman, M.E., Rivas, R., & Bayala, M. (2014). Subsurface Soil Moisture Estimation by VI–LST Method. *Geoscience and Remote Sensing Letters, IEEE, PP*, 1-5

Horst, T.W., & Weil, J.C. (1992). Footprint estimation for scalar flux measurements in the atmospheric surface layer. *Boundary-Layer Meteorology, 59*, 279-296

Hsieh, C.-I., Katul, G., & Chi, T.-w. (2000). An approximate analytical model for footprint estimation of scalar fluxes in thermally stratified atmospheric flows. *Advances in Water Resources, 23*, 765-772

Huemmrich, K.F. (2001). The GeoSail model: a simple addition to the SAIL model to describe discontinuous canopy reflectance. *Remote Sensing of Environment, 75*, 423-431

Huete, A. (1988). A soil-adjusted vegetation index (SAVI). *Remote Sensing of Environment, 25*, 295-309

Huete, A., Didan, K., Miura, T., Rodriguez, E.P., Gao, X., & Ferreira, L.G. (2002). Overview of the radiometric and biophysical performance of the MODIS vegetation indices. *Remote Sensing of Environment, 83*, 195-213

Jackson, R.D., Reginato, R.J., & Idso, S.B. (1977). Wheat canopy temperature: A practical tool for evaluating water requirements. *Water Resources Research, 13*, 651-656

Jacquemoud, S., & Baret, F. (1990). PROSPECT: A model of leaf optical properties spectra. *Remote Sensing of Environment, 34*, 75-91

Jacquemoud, S., Baret, F., Andrieu, B., Danson, F.M., & Jaggard, K. (1995). Extraction of vegetation biophysical parameters by inversion of the PROSPECT + SAIL models on sugar beet canopy reflectance data. Application to TM and AVIRIS sensors. *Remote Sensing of Environment, 52*, 163-172

Jasechko, S., Sharp, Z.D., Gibson, J.J., Birks, S.J., Yi, Y., & Fawcett, P.J. (2013). Terrestrial water fluxes dominated by transpiration. *Nature, 496*, 347-350

Jiang, L., & Islam, S. (2001). Estimation of surface evaporation map over Southern Great Plains using remote sensing data. *Water Resources Research, 37*, 329-340

Jurdao, S., Yebra, M., Guerschman, J.P., & Chuvieco, E. (2013). Regional estimation of woodland moisture content by inverting Radiative Transfer Models. *Remote Sensing of Environment, 132*, 59-70

Kaufman, Y.J., Wald, A.E., Remer, L.A., Bo-Cai, G., Rong-Rong, L., & Flynn, L. (1997). The MODIS 2.1-μm channel-correlation with visible reflectance for use in remote sensing of aerosol. *Geoscience and Remote Sensing, IEEE Transactions on, 35*, 1286-1298

Kerr, Y. (2007). Soil moisture from space: Where are we? *Hydrogeology Journal, 15*, 117-120

Kljun, N., Rotach, M.W., & Schmid, H.P. (2002). A Three-Dimensional Backward Lagrangian Footprint Model For A Wide Range Of Boundary-Layer Stratifications. *Boundary-Layer Meteorology, 103*, 205-226

Kotchenova, S.Y., Vermote, E.F., Matarrese, R., & Klemm, J.F.J. (2006). Validation of a vector version of the 6S radiative transfer code for atmospheric correction of satellite data. Part I: Path radiance. *Applied Optics, 45*, 6762-6774

Kustas, W.P., & Norman, J.M. (2000). A two-source energy balance approach using directional radiometric temperature observations for sparse canopy covered surfaces. *Agronomy Journal, 92*, 847-854

Law, B., Arkebauer, T., Campbell, J., Chen, J., Sun, O., Schwartz, M., van Ingen, C., & Verma, S. (2008). Terrestrial carbon observations: protocols for vegetation sampling and data submission. In. Rome, Italy: Terrestrial Carbon Observations Panel of the Global Terrestrial Observing System

Lhomme, J.P., & Elguero, E. (1999). Examination of evaporative fraction diurnal behaviour using a soil-vegetation model coupled with a mixed-layer model. *Hydrol. Earth Syst. Sci., 3*, 259-270

Li, F., Kustas, W.P., Anderson, M.C., Prueger, J.H., & Scott, R.L. (2008). Effect of remote sensing spatial resolution on interpreting tower-based flux observations. *Remote Sensing of Environment, 112*, 337-349

Li, Z.-L., Tang, R., Wan, Z., Bi, Y., Zhou, C., Tang, B., Yan, G., & Zhang, X. (2009). A Review of Current Methodologies for Regional Evapotranspiration Estimation from Remotely Sensed Data. *Sensors, 9*, 3801-3853

Liesenberg, V., Galvão, L.S., & Ponzoni, F.J. (2007). Variations in reflectance with seasonality and viewing geometry: Implications for classification of Brazilian savanna physiognomies with MISR/Terra data. *Remote Sensing of Environment, 107*, 276-286

Long, D., Singh, V.P., & Scanlon, B.R. (2012). Deriving theoretical boundaries to address scale dependencies of triangle models for evapotranspiration estimation. *Journal of Geophysical Research: Atmospheres, 117*, D05113

Loveland, T.R., & Belward, A.S. (1997). The IGBP-DIS global 1km land cover data set, DISCover: First results. *International Journal of Remote Sensing, 18*, 3289-3295

MacArthur, A., MacLellan, C.J., & Malthus, T. (2012). The Fields of View and Directional Response Functions of Two Field Spectroradiometers. *Geoscience and Remote Sensing, IEEE Transactions on, 50*, 3892-3907

Massman, W.J., & Lee, X. (2002). Eddy covariance flux corrections and uncertainties in long-term studies of carbon and energy exchanges. *Agricultural and Forest Meteorology, 113*, 121-144

McCabe, M.F., & Wood, E.F. (2006). Scale influences on the remote estimation of evapotranspiration using multiple satellite sensors. *Remote Sensing of Environment, 105*, 271-285

McColl, K.A., Pipunic, R.C., Ryu, D., & Walker, J.P. (2011). Validation of the MODIS LAI product in the Murrumbidgee Catchment, Australia. In, *MODSIM 2011 - 19th International Congress on Modelling and Simulation - Sustaining Our Future: Understanding and Living with Uncertainty* (pp. 1973-1979)

Menenti, M., & Choudhury, B.J. (1993). Parameterization of land surface evaporation by means of location dependent potential evaporation and surface temperature range.

*Exchange processes at the land surface for a range of space and time scales. Proc. international symposium, Yokohama, 1993*, 561-568

Minacapilli, M., Iovino, M., & Blanda, F. (2009). High resolution remote estimation of soil surface water content by a thermal inertia approach. *Journal of Hydrology, 379*, 229-238

Monteith, J.L. (1965). Evaporation and environment. *Symposia of the Society for Experimental Biology, 19*, 205-234

Moran, M.S., Clarke, T.R., Inoue, Y., & Vidal, A. (1994). Estimating crop water deficit using the relation between surface-air temperature and spectral vegetation index. *Remote Sensing of Environment, 49*, 246-263

Moran, M.S., Peters-Lidard, C.D., Watts, J.M., & McElroy, S. (2004). Estimating soil moisture at the watershed scale with satellite-based radar and land surface models. *Canadian Journal of Remote Sensing, 30*, 805-826

Nieto, H., Guzinski, R., Jensen, R., Sandholt, I., & Jensen, K.H. (2013). TSEBRTM: Coupling a canopy Radiative Transfer model with a Two Source Energy Balance Model for the Estimation of Surface Energy Fluxes with Dual-Angle Land Surface Temperature In, *TR32-HOBE International Symposium* Bonn, Germany

Papale, D., Reichstein, M., Aubinet, M., Canfora, E., Bernhofer, C., Kutsch, W., Longdoz, B., Rambal, S., Valentini, R., Vesala, T., & Yakir, D. (2006). Towards a standardized processing of Net Ecosystem Exchange measured with eddy covariance technique: algorithms and uncertainty estimation. *Biogeosciences, 3*, 571-583

Papale, D., & Valentini, R. (2003). A new assessment of European forests carbon exchanges by eddy fluxes and artificial neural network spatialization. *Global Change Biology, 9*, 525-535

Patel, N.R., Anapashsha, R., Kumar, S., Saha, S.K., & Dadhwal, V.K. (2008). Assessing potential of MODIS derived temperature/vegetation condition index (TVDI) to infer soil moisture status. *International Journal of Remote Sensing, 30*, 23-39

Peng, J., Borsche, M., Liu, Y., & Loew, A. (2013). How representative are instantaneous evaporative fraction measurements of daytime fluxes? *Hydrol. Earth Syst. Sci., 17*, 3913-3919

Peñuelas, J., Savé, R., Marfà , O., & Serrano, L. (1992). Remotely measured canopy temperature of greenhouse strawberries as indicator of water status and yield under mild and very mild water stress conditions. *Agricultural and Forest Meteorology, 58*, 63 - 77

Peterson, S.H., Roberts, D.A., & Dennison, P.E. (2008). Mapping live fuel moisture with MODIS data: A multiple regression approach. *Remote Sensing of Environment, 112*, 4272-4284

Pinty, B., & Verstraete, M.M. (1992). GEMI: a non-linear index to monitor global vegetation from satellites. *Plant Ecology, 101*, 15-20

Price, J.C. (1990). Using spatial context in satellite data to infer regional scale evapotranspiration. *Geoscience and Remote Sensing, IEEE Transactions on, 28*, 940-948

Priestley, C.H.B., & Taylor, R.J. (1972). On the Assessment of Surface Heat Flux and Evaporation Using Large-Scale Parameters. *Monthly Weather Review, 100*, 81-92

Proud, S.R., Fensholt, R., Rasmussen, M.O., & Sandholt, I. (2010). A comparison of the effectiveness of 6S and SMAC in correcting for atmospheric interference of Meteosat Second Generation images. *Journal of Geophysical Research: Atmospheres, 115*, D17209

Proud, S.R., Zhang, Q., Schaaf, C., Fensholt, R., Rasmussen, M.O., Shisanya, C., Mutero, W., Mbow, C., Anyamba, A., Pak, E., & Sandholt, I. (2014). The Normalization of Surface Anisotropy Effects Present in SEVIRI Reflectances by Using the MODIS BRDF Method. *Geoscience and Remote Sensing, IEEE Transactions on, PP*, 1-14

Rahman, H., & Dedieu, G. (1994). SMAC: a simplified method for the atmospheric correction of satellite measurements in the solar spectrum. *International Journal of Remote Sensing, 15*, 123-143

Rasmussen, M.O., Pinheiro, A.C., Proud, S.R., & Sandholt, I. (2010). Modeling Angular Dependences in Land Surface Temperatures From the SEVIRI Instrument Onboard the

Geostationary Meteosat Second Generation Satellites. *Geoscience and Remote Sensing, IEEE Transactions on, 48*, 3123-3133

Rasmussen, M.O., Sørensen, M.K., Wu, B., Yan, N., Qin, H., & Sandholt, I. (2014). Regional-scale estimation of evapotranspiration for the North China Plain using MODIS data and the triangle-approach. *International Journal of Applied Earth Observation and Geoinformation, 31*, 143-153

Reichstein, M., Falge, E., Baldocchi, D., Papale, D., Aubinet, M., Berbigier, P., Bernhofer, C., Buchmann, N., Gilmanov, T., Granier, A., Grünwald, T., Havránková, K., Ilvesniemi, H., Janous, D., Knohl, A., Laurila, T., Lohila, A., Loustau, D., Matteucci, G., Meyers, T., Miglietta, F., Ourcival, J.-M., Pumpanen, J., Rambal, S., Rotenberg, E., Sanz, M., Tenhunen, J., Seufert, G., Vaccari, F., Vesala, T., Yakir, D., & Valentini, R. (2005). On the separation of net ecosystem exchange into assimilation and ecosystem respiration: review and improved algorithm. *Global Change Biology, 11*, 1424-1439

Riaño, D., Vaughan, P., Chuvieco, E., Zarco-Tejada, P.J., & Ustin, S.L. (2005). Estimation of fuel moisture content by inversion of radiative transfer models to simulate equivalent water thickness and dry matter content: analysis at leaf and canopy level. *Geoscience and Remote Sensing, IEEE Transactions on, 43*, 819-826

Richter, K., Atzberger, C., Hank, T.B., & Mauser, W. (2012). Derivation of biophysical variables from Earth observation data: validation and statistical measures. *Journal of Applied Remote Sensing, 6*, 063557-063551-063557-063523

Roberts, D.A., Dennison, P.E., Peterson, S., Sweeney, S., & Rechel, J. (2006). Evaluation of Airborne Visible/Infrared Imaging Spectrometer (AVIRIS) and Moderate Resolution Imaging Spectrometer (MODIS) measures of live fuel moisture and fuel condition in a shrubland ecosystem in southern California. *Journal of Geophysical Research: Biogeosciences, 111*, G04S02

Roerink, G.J., Su, Z., & Menenti, M. (2000). S-SEBI: A simple remote sensing algorithm to estimate the surface energy balance. *Physics and Chemistry of the Earth, Part B: Hydrology, Oceans and Atmosphere, 25*, 147-157

Rouse, J.W., Haas, R.H., Deering, D.W., & Schell, J.A. (1973). Monitoring the vernal advancement and retrogradation (green wave effect) of natural vegetation. In (p. 87). Greenbelt, MD: Goddard Space Flight Center

Ryu, Y., Baldocchi, D.D., Kobayashi, H., van Ingen, C., Li, J., Black, T.A., Beringer, J., van Gorsel, E., Knohl, A., Law, B.E., & Roupsard, O. (2011). Integration of MODIS land and atmosphere products with a coupled-process model to estimate gross primary productivity and evapotranspiration from 1 km to global scales. *Global Biogeochemical Cycles, 25*, GB4017

Sánchez-Ruiz, S., Piles, M., Sánchez, N., Martínez-Fernández, J., Vall-llossera, M., & Camps, A. (2014). Combining SMOS with visible and near/shortwave/thermal infrared satellite data for high resolution soil moisture estimates. *Journal of Hydrology, 516*, 273-283

Sandholt, I., Rasmussen, K., & Andersen, J. (2002). A simple interpretation of the surface temperature/vegetation index space for assessment of surface moisture status. *Remote Sensing of Environment, 79*, 213-224

Schaaf, C.B., Gao, F., Strahler, A.H., Lucht, W., Li, X., Tsang, T., Strugnell, N.C., Zhang, X., Jin, Y., Muller, J.-P., Lewis, P., Barnsley, M., Hobson, P., Disney, M., Roberts, G., Dunderdale, M., Doll, C., d'Entremont, R.P., Hu, B., Liang, S., Privette, J.L., & Roy, D. (2002). First operational BRDF, albedo nadir reflectance products from MODIS. *Remote Sensing of Environment, 83*, 135-148

Schlesinger, W.H., & Bernhardt, E.S. (2013). Chapter 6 - The Biosphere: Biogeochemical Cycling on Land. In W.H. Schlesinger, & E.S. Bernhardt (Eds.), *Biogeochemistry (Third Edition)* (pp. 173-231). Boston: Academic Press

Schmid, H.P. (1994). Source areas for scalars and scalar fluxes. *Boundary-Layer Meteorology, 67*, 293-318

Schmugge, T. (1978). Remote Sensing of Surface Soil Moisture. *Journal of Applied Meteorology, 17*, 1549-1557

Seguin, B., & Itier, B. (1983). Using midday surface temperature to estimate daily evaporation from satellite thermal IR data. *International Journal of Remote Sensing, 4*, 371-383

Sepulcre-Cantó, G., Zarco-Tejada, P.J., Jiménez-Muñoz, J.C., Sobrino, J.A., de Miguel, E., & Villalobos, F.J. (2006). Detection of water stress in an olive orchard with thermal remote sensing imagery. *Agricultural and Forest Meteorology, 136*, 31 - 44

Shuttleworth, W., Gurney, R., Hsu, A., & Ormsby, J. (1989). FIFE: the variation in energy partition at surface flux sites. *IAHS Publ, 186*, 67-74

Sims, D.A., & Gamon, J.A. (2003). Estimation of vegetation water content and photosynthetic tissue area from spectral reflectance: a comparison of indices based on liquid water and chlorophyll absorption features. *Remote Sensing of Environment, 84*, 526-537

Smith, R.C.G., & Choudhury, B.J. (1991). Analysis of normalized difference and surface temperature observations over southeastern Australia. *International Journal of Remote Sensing, 12*, 2021-2044

Sobrino, J.A., & Romaguera, M. (2004). Land surface temperature retrieval from MSG1-SEVIRI data. *Remote Sensing of Environment, 92*, 247-254

Sobrino, J.A., & Romaguera, M. (2007). Water-vapour retrieval from Meteosat 8/SEVIRI observations. *International Journal of Remote Sensing, 29*, 741-754

Steyerberg, E.W., Harrell Jr, F.E., Borsboom, G.J.J.M., Eijkemans, M.J.C., Vergouwe, Y., & Habbema, J.D.F. (2001). Internal validation of predictive models: Efficiency of some procedures for logistic regression analysis. *Journal of Clinical Epidemiology, 54*, 774-781

Stisen, S., Jensen, K.H., Sandholt, I., & Grimes, D.I.F. (2008a). A remote sensing driven distributed hydrological model of the Senegal River basin. *Journal of Hydrology, 354*, 131-148

Stisen, S., Sandholt, I., Nørgaard, A., Fensholt, R., & Eklundh, L. (2007). Estimation of diurnal air temperature using MSG SEVIRI data in West Africa. *Remote Sensing of Environment, 110*, 262-274

Stisen, S., Sandholt, I., Nørgaard, A., Fensholt, R., & Jensen, K.H. (2008b). Combining the triangle method with thermal inertia to estimate regional evapotranspiration — Applied to MSG-SEVIRI data in the Senegal River basin. *Remote Sensing of Environment, 112*, 1242-1255

Stow, D., Niphadkar, M., & Kaiser, J. (2005). MODIS-derived visible atmospherically resistant index for monitoring chaparral moisture content. *International Journal of Remote Sensing, 26*, 3867-3873

Stow, D., Niphadkar, M., & Kaiser, J. (2006). Time series of chaparral live fuel moisture maps derived from MODIS satellite data. *International Journal of Wildland Fire, 15*, 347-360

Sugita, M., & Brutsaert, W. (1991). Daily evaporation over a region from lower boundary layer profiles measured with radiosondes. *Water Resources Research, 27*, 747-752

Sun, L., Sun, R., Li, X., Liang, S., & Zhang, R. (2012). Monitoring surface soil moisture status based on remotely sensed surface temperature and vegetation index information. *Agricultural and Forest Meteorology, 166–167*, 175-187

Syed, T.H., Famiglietti, J.S., Chambers, D.P., Willis, J.K., & Hilburn, K. (2010). Satellite-based global-ocean mass balance estimates of interannual variability and emerging trends in continental freshwater discharge. *Proceedings of the National Academy of Sciences*

Taiz, L., & Zeiger, E. (2010). *Plant Physiology*. Sinauer Associates, Incorporated

Tang, R., Li, Z.-L., & Tang, B. (2010). An application of the Ts–VI triangle method with enhanced edges determination for evapotranspiration estimation from MODIS data in arid and semi-arid regions: Implementation and validation. *Remote Sensing of Environment, 114*, 540-551

Taylor, K.E. (2001). Summarizing multiple aspects of model performance in a single diagram. *Journal of Geophysical Research: Atmospheres, 106*, 7183-7192

Trigo, I.F., Peres, L.F., DaCamara, C.C., & Freitas, S.C. (2008). Thermal Land Surface Emissivity Retrieved From SEVIRI/Meteosat. *Geoscience and Remote Sensing, IEEE Transactions on, 46*, 307-315

Trombetti, M., Riaño, D., Rubio, M.A., Cheng, Y.B., & Ustin, S.L. (2008). Multi-temporal vegetation canopy water content retrieval and interpretation using artificial neural networks for the continental USA. *Remote Sensing of Environment, 112*, 203 - 215

Venturini, V., Bisht, G., Islam, S., & Jiang, L. (2004). Comparison of evaporative fractions estimated from AVHRR and MODIS sensors over South Florida. *Remote Sensing of Environment, 93*, 77-86

Venturini, V., Islam, S., & Rodriguez, L. (2008). Estimation of evaporative fraction and evapotranspiration from MODIS products using a complementary based model. *Remote Sensing of Environment, 112*, 132-141

Verbesselt, J., Somers, B., Lhermitte, S., Jonckheere, I., van Aardt, J., & Coppin, P. (2007). Monitoring herbaceous fuel moisture content with SPOT VEGETATION time-series for fire risk prediction in savanna ecosystems. *Remote Sensing of Environment, 108*, 357 - 368

Verhoef, W. (1985). Earth observation modeling based on layer scattering matrices. *Remote Sensing of Environment, 17*, 165-178

Verhoef, W., Jia, L., Qing, X., & Su, Z. (2007). Unified Optical-Thermal Four-Stream Radiative Transfer Theory for Homogeneous Vegetation Canopies. *Geoscience and Remote Sensing, IEEE Transactions on, 45*, 1808-1822

Vermote, E.F., Tanre, D., Deuze, J.L., Herman, M., & Morcette, J.J. (1997). Second Simulation of the Satellite Signal in the Solar Spectrum, 6S: an overview. *Geoscience and Remote Sensing, IEEE Transactions on, 35*, 675-686

Vicente-Serrano, S.M., Pons-Fernández, X., & Cuadrat-Prats, J.M. (2004). Mapping soil moisture in the central Ebro river valley (northeast Spain) with Landsat and NOAA satellite imagery: a comparison with meteorological data. *International Journal of Remote Sensing, 25*, 4325-4350

Vlassova, L., Perez-Cabello, F., Nieto, H., Martín, P., Riaño, D., & de la Riva, J. (2014). Assessment of Methods for Land Surface Temperature Retrieval from Landsat-5 TM Images Applicable to Multiscale Tree-Grass Ecosystem Modeling. *Remote Sensing, 6*, 4345-4368

Wang, C., Qu, J.J., Xiaoxiong, X., Xianjun, H., Yong, X., & Nianzeng, C. (2006a). A new method for retrieving band 6 of aqua MODIS. *Geoscience and Remote Sensing Letters, IEEE, 3*, 267-270

Wang, K., Li, Z., & Cribb, M. (2006b). Estimation of evaporative fraction from a combination of day and night land surface temperatures and NDVI: A new method to determine the Priestley–Taylor parameter. *Remote Sensing of Environment, 102*, 293-305

Wang, L., Qu, J.J., Hao, X., & Zhu, Q. (2008). Sensitivity studies of the moisture effects on MODIS SWIR reflectance and vegetation water indices. *International Journal of Remote Sensing, 29*, 7065-7075

Weiss, M., Baret, F., Garrigues, S., & Lacaze, R. (2007). LAI and fAPAR CYCLOPES global products derived from VEGETATION. Part 2: validation and comparison with MODIS collection 4 products. *Remote Sensing of Environment, 110*, 317-331

Wolfe, R.E., Nishihama, M., Fleig, A.J., Kuyper, J.A., Roy, D.P., Storey, J.C., & Patt, F.S. (2002). Achieving sub-pixel geolocation accuracy in support of MODIS land science. *Remote Sensing of Environment, 83*, 31-49

Yebra, M., Chuvieco, E., & Aguado, I. (2008a). Comparación entre modelos empíricos y de transferencia radiativa para estimar contenido de humedad en pastizales: Poder de generalización. *Revista de Teledetección, 29*, 73-90

Yebra, M., Chuvieco, E., & Riaño, D. (2008b). Estimation of live fuel moisture content from MODIS images for fire risk assessment. *Agricultural and Forest Meteorology, 148*, 523 - 536

Yebra, M., Dennison, P.E., Chuvieco, E., Riaño, D., Zylstra, P., Hunt Jr, E.R., Danson, F.M., Qi, Y., & Jurdao, S. (2013). A global review of remote sensing of live fuel moisture content for fire danger assessment: Moving towards operational products. *Remote Sensing of Environment, 136*, 455-468

Yilmaz, M.T., Hunt Jr, E.R., Goins, L.D., Ustin, S.L., Vanderbilt, V.C., & Jackson, T.J. (2008). Vegetation water content during SMEX04 from ground data and Landsat 5 Thematic Mapper imagery. *Remote Sensing of Environment, 112*, 350-362

Zarco-Tejada, P.J., Rueda, C.A., & Ustin, S.L. (2003). Water content estimation in vegetation with MODIS reflectance data and model inversion methods. *Remote Sensing of Environment, 85*, 109 - 124

Zhu, Z., & Woodcock, C.E. (2012). Object-based cloud and cloud shadow detection in Landsat imagery. *Remote Sensing of Environment, 118*, 83-94

# 8 List of figures

# 9 List of tables